SUBSIDENCE STUDY IN NORTHWEST HARRIS COUNTY USING GPS, LIDAR AND INSAR TECHNIQUES

A Thesis

Presented to

the Faculty of the Department of Earth and Atmospheric Sciences

University of Houston

In Partial Fulfillment

of the Requirements for the Degree

Master of Science

By

Ayca Karacay

University of Houston

May 2013

STUDY OF GROUND SUBSIDENCE IN NORTHWEST HARRIS COUNTY USING GPS, LIDAR AND INSAR TECHNIQUES

Ayca Karacay

APPROVED:

Dr. Shuhab Khan, Chairman

Dr. Guoquan Wang, Member

Dr. Hyongki Lee, Member

Dean, College of Natural Sciences and Mathematics

Acknowledgements

I am thankful to my advisor Dr. Shuhab Khan for his guidance and suggestions throughout this endeavor. I also wish to thank my committee members Dr. Guoquan Wang and Dr. Hyongki Lee of Civil Engineering Department and NCALM. Many thanks to Clifton S. Middleton, the NGS representative of HGSD, for providing important information about the GPS network and for supplying the GPS data. Many thanks to my sponsor Turkish Petroleum Corporation.

Many thanks go to my co-workers from GeoRS Team: Ismail Abir, Yahaya Abu, Xu Han, Jessica Quintanar, Zheng Huang, Kevin Schimdt, and especially my best friends Kivanc Biber and Unal Okyay for their support. Also many thanks to my former employer Dr. Arda Arcasoy for his support and encouragement for my master before I started MSc program.

Last but not least, my special thanks are to my loving family for their support, encouragement, and prayers.

STUDY OF GROUND SUBSIDENCE IN NORTHWEST HARRIS COUNTY USING GPS, LIDAR AND INSAR TECHNIQUES

An Abstract of

a Thesis

Presented to

the Faculty of the Department of Earth and Atmospheric Sciences

University of Houston

In Partial Fulfillment

of the Requirements for the Degree

Master of Science

By

Ayca Karacay

University of Houston

May 2013

ABSTRACT

Subsidence has been affecting many cities around the world, such as Nagoya (Japan), Venice (Italy), San Joaquin Valley and Long Beach (California), and Houston (Texas). This phenomenon can be caused by natural processes and/or human activities, including but not limited to carbonate dissolution, extraction of material from mines, soil compaction, and fluid withdrawal. Recent studies on Harris County, Texas suggested that surface deformation is driven by four major mechanisms: faulting, soil compaction, salt tectonics, and fluid withdrawal (groundwater withdrawal and hydrocarbon extraction). The objective of this study was to assess the land deformation rate in the northwest Harris and detect the effect of fluid withdrawal on subsidence. To achieve this goal, data from three complimentary remote sensing techniques Global Positioning System (GPS), Light Detection and Ranging (LiDAR), and Interferometric Synthetic Aperture Radar (InSAR) were used. The data of twenty (20) GPS stations acquired from Harris-Galveston Subsidence District (HGCSD) were processed using Online Positioning User Service (OPUS) of National Geodetic Survey (NGS). Two (2) of these GPS stations are Continuously Operating Reference Stations (CORS), and eighteen (18) are Port-A-Measure (PAM) sites. The zonal statistic method was applied on 2001 and 2008 Digital Elevation Models (DEMs) generated using LiDAR data. The Persistent Scatterer Interferometry (PSI) was performed using twenty five (25) ERS1/2 data. The rates of change in groundwater level and hydrocarbon production were calculated using data from 261 water wells and 658 hydrocarbon wells. Furthermore, the rates of change in groundwater level and hydrocarbon production were compared to the results of remote

sensing techniques. The results of this study revealed the rates of subsidence ranging from 0.3 to 4.5 cm/y for GPS, LiDAR, and InSAR. The level of groundwater drops with a rate of 4 m/y close to the area where subsidence is the highest. Also, the hydrocarbon withdrawals are highest (~70 million m^3/y) in areas sinking more rapidly. This study found strong correlation between fluid withdrawals and subsidence. Therefore, both groundwater and hydrocarbon withdrawal in northwest Harris are considered to be the major drivers of the subsidence deformation.

Contents

List of Figures

CHAPTER 1: INTRODUCTION

1.1 Introduction

Subsidence, the in situ downward motion of the Earth's surface, has long been a hazard. It has been caused by both geological phenomena and man-induced events; such as mining activities, compaction of sediments, earthquakes, dissolution of limestone, oxidation of organic deposits, and fluid withdrawal (Johnson, 1991). For example, subsidence in Mexico City is caused by groundwater withdrawal and aquifer system compaction; in India caused by coal mining; in Spain caused by dissolution of limestone; and in Japan caused by extraction of natural gas (Johnson, 1991). Likewise, in the United States, subsidence hazards have been reported caused by different factors such as drainage of organic soil in California, collapse cavities in Florida and New York, and mining in Ohio. However, the most common cause of subsidence in the U.S. is fluid withdrawal from the subsurface (National Research Council, 1991). Because of the human-induced subsidence, in addition to downward motion of the surface, the activation of some surface faults can be expected near these sinking regions (Morton et al., 2002). One of the U.S. cities in which these two related phenomena are encountered is Houston and surrounding vicinity (Figure 1.1). Houston and Galveston regions have coped with this subsidence problem for about 100 years. Engelkemeir et al. (2010) discussed four major mechanisms that cause subsidence for that region: faulting, soil compaction, salt tectonics, and fluid (groundwater and hydrocarbon) withdrawal. Groundwater withdrawal has been reported as the main cause of the surface deformation over the greater Houston area (Holzer & Bluntzer, 1984; Coplin & Galloway, 1999; Zilkoski et al., 2003; Engelkemeir et al., 2010). In addition to groundwater withdrawal, oil and gas extraction

has also been reported as another factor that causes subsidence in the greater Houston area (e.g. Goose Creek Oil Field) (Holzer & Bluntzer, 1984). The northwest portion of the Harris County is one of the well-known areas coping with subsiding. It is assumed that the cause of subsidence is groundwater pumping in the Northwest Harris area. However, the effects of hydrocarbon extraction on subsidence in northwest Harris were not well-documented. In this thesis, the role of the fluid withdrawal, both groundwater and oil, on subsidence is examined using Global Positioning System (GPS), Light Detection and Ranging (LiDAR), and Interferometric Synthetic Aperture Radar (InSAR) techniques.

1.2 Study Area

The Northwest Harris area is one of the census city divisions (CCDs) located in the northwest of the city of Houston, in Harris County (Figure 1.1) (U.S. Census, 2000). It covers approximately 1150 km^2 (~440 square miles) area. The Northwest Harris area is bounded by three counties: Fort Bend, Montgomery, and Waller. The elevation of the region is changing from 15 meters (50 feet) to 94 meters (310 feet) from southeast to northwest (Martin et al., 2012). The climate in the study area is humid subtropical - hot and humid in spring, summer, and autumn, and rainy in winter. The annual temperature changes from 45^o F (7.2^o C) to 93^o F (33.8^o C). Average annual precipitation in the area is about 1.2 meters (47 inches) (Coplin & Galloway, 1991). The historical tornado activity in Northwest Harris is above the average of Texas (OnboardInformatics, 2012). The well-known localities on the study area are Cypress, Tomball, Jersey Village, and Hockley.

The population of the Northwest Harris CCD is estimated 651,000 (U.S. Census, 2010). In the study area, there are three airports, one of which is the George Bush International Airport. Other transportation systems, such as railway, also have importance for the area for trading.

The study area is lying over the Gulf Coast aquifer system. There are three fault systems (Hockley, Addicks, and Long Point), and two salt domes (Hockley, and Tomball) within the study area (Figure 1.1). Moreover, eight (8) oil fields, some of which are still operational, are located in the study area.

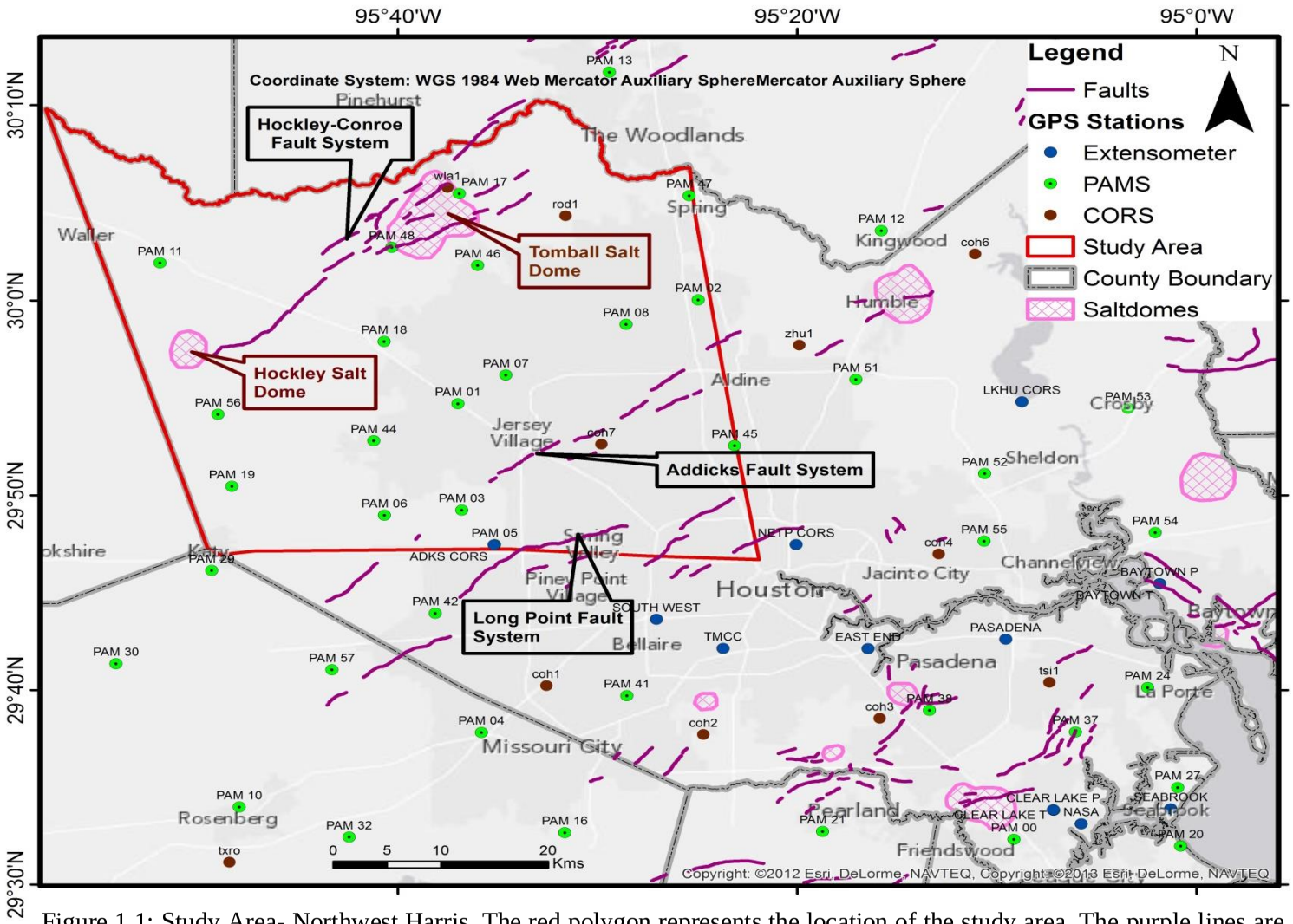

Figure 1.1: Study Area- Northwest Harris. The red polygon represents the location of the study area. The purple lines are for the surface faults and the pink polygons shows salt domes. The blue, brown, and green points show the location of extensometers, CORS, and PAM GPS Stations, respectively.

1.3 Geological Setting

Harris County, located in southeast of Texas, lies on the Gulf of Mexico coastal plain. The formation of the region started in the Late Triassic (Salvador, 1991). The area was located in the middle part of the Pangaea (Figure 1.2). In the late Triassic, the breakup of the Pangaea took place. After the breakup, the North American plate drifted apart from the African and the South American plate in clockwise motion. With the spreading, the formation of the Gulf basin and ocean initiated (Figure 1.2) (Salvador, 1991; Bird et. al., 2005; Stern & Dickinson, 2010). Concurrently, the Louann Salt and evaporites underlying Gulf Coast were deposited into the basin. Due to the continuity of the spreading, marine waters eventually permanently flooded the region, and the deposition of the salt was stopped (Salvador, 1991; Stern & Dickinson, 2010). The northwest Gulf of Mexico proceeded to be filled by different river systems during Mesozoic (Galloway, 2008).

The prograding shelf on the northwest of the Gulf of Mexico was filled by fluvial deposits formed by erosion of the Rocky Mountains (Galloway et al., 2000). The river deposits were carried by Brazos, Colorado, and Trinity River, and created the Houston "Delta" on the coastline of the Gulf of Mexico (Bernard et al., 1962). The deposits of the deltaic sediments consist of sands, clays, and some organic materials with the fining-upwards sedimentation (Galloway et al., 2000).

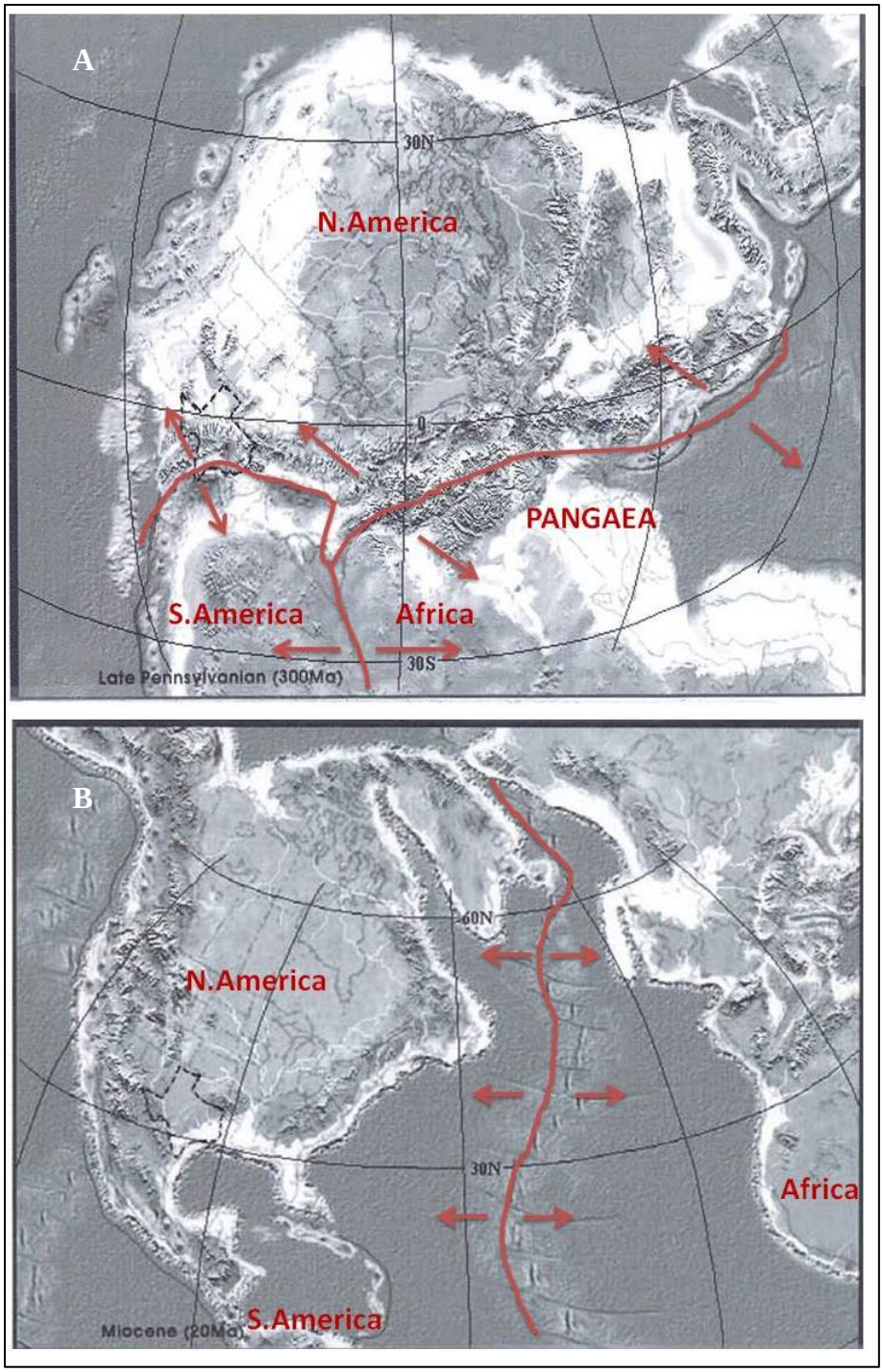

Figure 1.2: Geologic evolution of Texas. A; Paleogeographic map of North America and the location of Texas in the Late Pennsylvanian. This map also illustrates the beginning of the continental drift. B; Paleogeographic map of North America and the location of Texas in the Miocene (modified from Blakey, 2006).

There are more than 160 subsurface and surface fault systems in Harris County (Figure 1.1). Some of the fault systems are active due to natural and man-induced events. The natural factors of the fault activities are salt diapir activities, imperceptible downslope movement of sediments masses towards gulf, and distinctive compaction rates of the sediments (Verbeek & Clanton, 1981). The faults in Houston and surrounding vicinity were stated as growth faults trending southwest-northeast. Most of these faults were observed over the salt diapirs predominantly located in the southeast part of Harris County (Figure 1.3) (Kreitler, 1977; Norman, 2005; Engelkemeir & Khan, 2008).

In the Northwest Harris area, there are three fault systems: Long Point Fault System (FS), Addicks Fault System, and Hockley-Conroe Fault System (Figure 1.1). The Long Point FS, located in the southeast portion of the study area, is one of the highly active faults in Harris County (Engelkeimer & Khan, 2008). The Addicks FS is located close to Long Point FS and trends southwest-northeast. The Hockley-Conroe FS is situated in the northwest portion of study area and extends from Hockley Salt Dome to Woodlands with southwest-northeast trend (Engelkeimer & Khan, 2008; Kreitler, 1977; Saribudak, 2010).

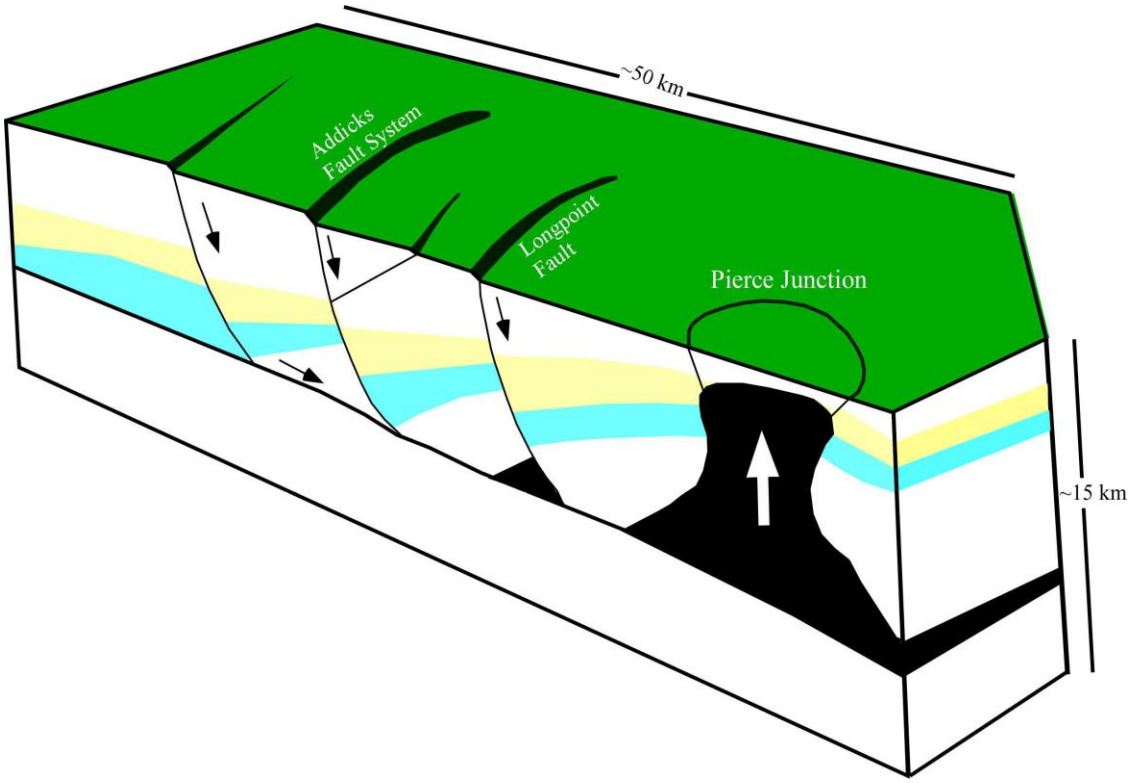

Figure 1.3: Sketch for the relation between salt domes and surface faults (Engelkemeir et al., 2010).

1.4 History and Monitoring of the Subsidence

The first noticeable subsidence that has been reported in greater Houston area occurred over Goose Creek oil field, in 1920s due to hydrocarbon production (Neighbors, 2003). Later on, along with the progress of industry, the population began to rise in Houston. Increasing demand of water induced groundwater withdrawal in higher rates. Subsequently, subsidence rate in Houston increased due to extensive groundwater withdrawal. (Coplin & Galloway, 1999). Before 1942, subsidence occurred locally where the groundwater was heavily withdrawn. However, a larger portion of Harris County had

started to be affected by subsidence after 1943 (Kreitler, 1977; Coplin & Galloway, 1999).

The Texas Legislature decided to assign the Harris-Galveston Coastal Subsidence District (HGCSD) in 1975 in order to respond to the increasing effects of subsidence and manage groundwater resources (Zilkoski et al., 2003). As the first action, HGCSD decided to monitor the Harris-Galveston Counties within three regulatory areas. The first area, from Galveston to Pasadena, began to use surface water as the main water supply in the late 1970s (Coplin & Galloway, 1999; Neighbors, 2003). The second area covering south portion of Harris and a small area in the northwestern Galveston started to supply water from alternative sources after 1990s. The third regulatory area involving the study area initiated a search of new sources for water supply in 1999 (Michel, 2006). Two different measurement methods were used to monitor subsidence between 1970s and 1990s: conventional differential leveling and extensometer (Zilkoski et al., 2003; Michel, 2006). However, GPS methods have replaced these methods as being more affordable and more convenient. GPS methods used for subsidence monitoring will be explained in detail in Chapter 2.

1.5 Scope and Purpose

Several researchers reported that the northwest portion of Harris County has been subsiding due to groundwater withdrawal (Coplin & Galloway, 1999; HGCSD, 2012). However, the effects of the oil and gas extraction have not been well described. The aim of this study is to assess the effects of the fluid withdrawal on subsidence in the study

area. To achieve this goal the following steps were taken: (**1**) GPS, LiDAR, and InSAR remote sensing techniques were used to quantify subsidence, (**2**) depth to the groundwater level data were acquired from USGS, (**3**) hydrocarbon production data were acquired from Railroad Commission of Texas, (**4**) two surface models were created from the rate of change in groundwater level and hydrocarbon extraction, and finally (**5**) the results from remote sensing techniques and surface models were compared and discussed to identify the relation between land subsidence and fluid withdrawal in northwest Harris.

1.6 Summary of Chapters

This thesis is divided into five chapters:

CHAPTER 1 gives a brief introduction about the subsidence phenomenon in the Northwest Harris area. General information about the study area and geological setting of the greater Houston area I presented in this chapter. The history of land subsidence and subsidence monitoring in the area are elucidated in this chapter. The scope and purpose of the study is also expressed in this chapter.

CHAPTER 2 provides detailed information about datasets and methods used in this study. This chapter includes five (5) sections: (1) Global Positioning System (GPS), (2) Light Detection and Ranging (LiDAR), (3) Interferometric Synthetic Aperture Radar (InSAR), (4) Groundwater, and (5) Hydrocarbon.

CHAPTER 3 presents the results of the datasets and methods mentioned in the previous chapter. Likewise, results of each datasets are presented in corresponding sections. The

GPS, LiDAR, and InSAR sections contain displacement maps while groundwater and hydrocarbon sections include surface models for the rate of change in groundwater level and the rate of hydrocarbon extraction.

CHAPTER 4 comprises the overall comparison and discussion of the results of different datasets. In addition the major causes of the subsidence in the study area along with their relative contributions on subsidence are addressed in this chapter.

CHAPTER 5 summarizes and concludes the entire study.

CHAPTER 2: DATA PROCESSING and METHODS

Data from three different techniques; GPS, LiDAR, and InSAR, were used for detecting surface deformation. The groundwater level observation and oil/gas extraction data were also processed to see their influence on the subsidence over the Northwest Harris area.

2.1 GPS

2.1.1 Introduction

Global Positioning System (GPS) is a U.S. Department of Defense satellite-based navigation system designed to provide continuous worldwide positioning and navigation capability (Sneed & Brandt, 2007). This system is used for not only getting information about positioning and navigation, but also measuring the vertical and horizontal deformation on the land surface. The principle of this system is to utilize at least three satellites to locate a point on the surface of the Earth. However, in order to increase the precision and time accuracy, a fourth satellite is needed (Figure 2.1) (Carter, 1997).

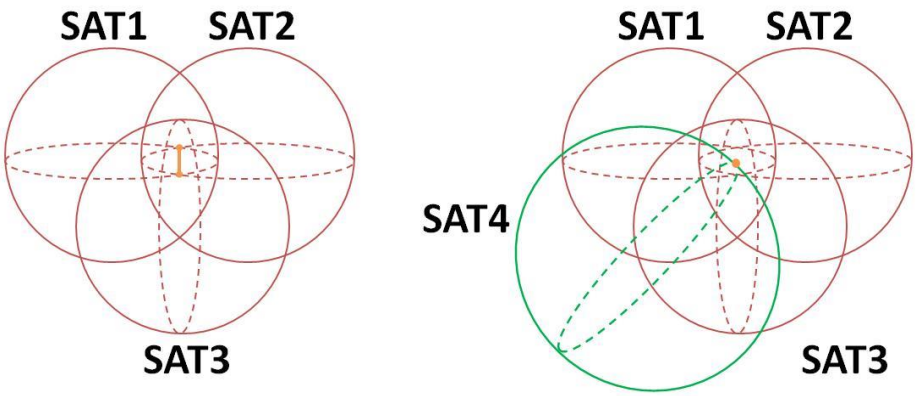

Figure 2.1: Sketch of GPS principle. The sketch on the left demonstrates the intersection of three GPS signals. Right image expresses the intersection of the GPS signals when the fourth GPS attends. The orange line on the left image and orange point on the right image show the location found by GPS signals.

2.1.2 Background of Deformation Monitoring by GPS

Monitoring the land surface deformation was controversy in the past. The scientists tried many ways to measure the rate of the land surface deformations such as fault movement, surface uplift, and subsidence. The Houston-Galveston region was one of these controversial areas to monitor the subsidence. The National Geodetic Survey (NGS), National Oceanic and Atmospheric Administration (NOAA), and Harris-Galveston Coastal Subsidence District (HGCSD) used two different methods to assess the subsidence in the past (Zilkoski et al., 2003).

The first method was re-leveling which provides a very good spatial subsidence data. For this method, they used more than 2,500 benchmarks. The principle of this method is to calculate differential leveling by subtracting level lines of subsidence between two re-leveling times. The only restriction of this method was the cost of the procedure (Zilkoski et al., 2003).

The second method is measuring subsidence using the deep borehole extensometers (Figure 2.2). This system was designed and installed by U.S. Geological Society. A borehole was placed into a drilled hole through the stable strata. The sidewalls of the hole have slip joints allowing the extensometer to move. The inner pipe was fitted to the concrete plug on the bottom of borehole. The movement of subsidence was measured by the inner pipe part. Although this method gives excellent data for subsidence, the cost of extensometer restricts its use for Houston-Galveston area (Zilkoski et al., 2003).

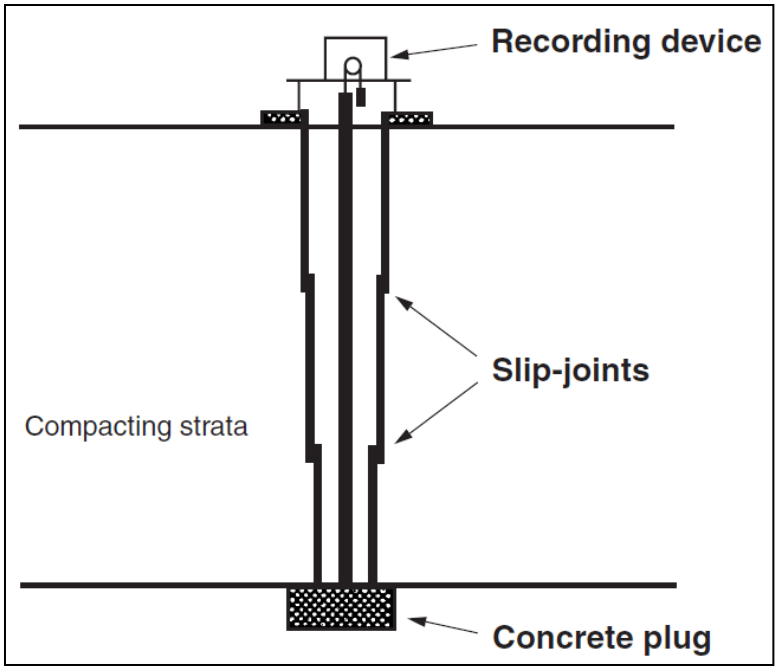

Figure 2.2: Cartoon of borehole extensometer. The slip-joints isolating the inner pipe from the compaction of the surrounding strata allow sliding of the wall of extensometer. The inner pipe is cemented on to a concrete plug places in stable sedimentary layer. Recording device is measuring the vertical displacement from the difference between the inner pipe and the slip-joints (Zilkoski, et al., 2003).

Because of the high costs of these two methods, HGSD and NGS installed the first GPS station in 1993 (Zilkoski et al., 2003). The first three GPS stations were installed on the extensometers. These stations were named as Continuous Operating Reference Stations (CORS). These stations are: Addicks (ADKS), Lake Houston (LKHU), and Northeastern (NETP). The installed GPS stations have dual-frequency GPS which are collecting 30-second interval continuous data for 24 hour.

To monitor larger area of the Houston-Galveston region, it was decided to install new GPS stations called as Port-A-Measure (PAM). The antenna of the PAM stations is

portable. The monuments of the PAM stations were planned to reduce the compaction and expansion potential of clay-rich soils. The thickness of these clay-rich layers is about 4 to 6 meters (15 to 20 ft.). While designing these monuments, occurrence of vertical movement (at most 9 cm) due to seasonal change was considered (Zilkoski, et al., 2003). The monument of a PAM site is composed of three parts two of which are placed into a 6-meter deep drilled hole (Figure 2.3). The lower part, made of sacrete-mix of concrete, provides the stability of the monument. Above the sacrete part, the 2-1/2 inch PVC (polyvinyl chloride) sleeve is set. This PVC part is stabilized using one bag of sacrete around the sleeve. The third part of the monument, on the land surface, is cemented on the PVC sleeve. This part is a heavy wall galvanized pipe 2.5 meter (8 feet) high. The GPS antenna of the PAM stations are set on the top of the this pipe (Zilkoski et al., 2003)

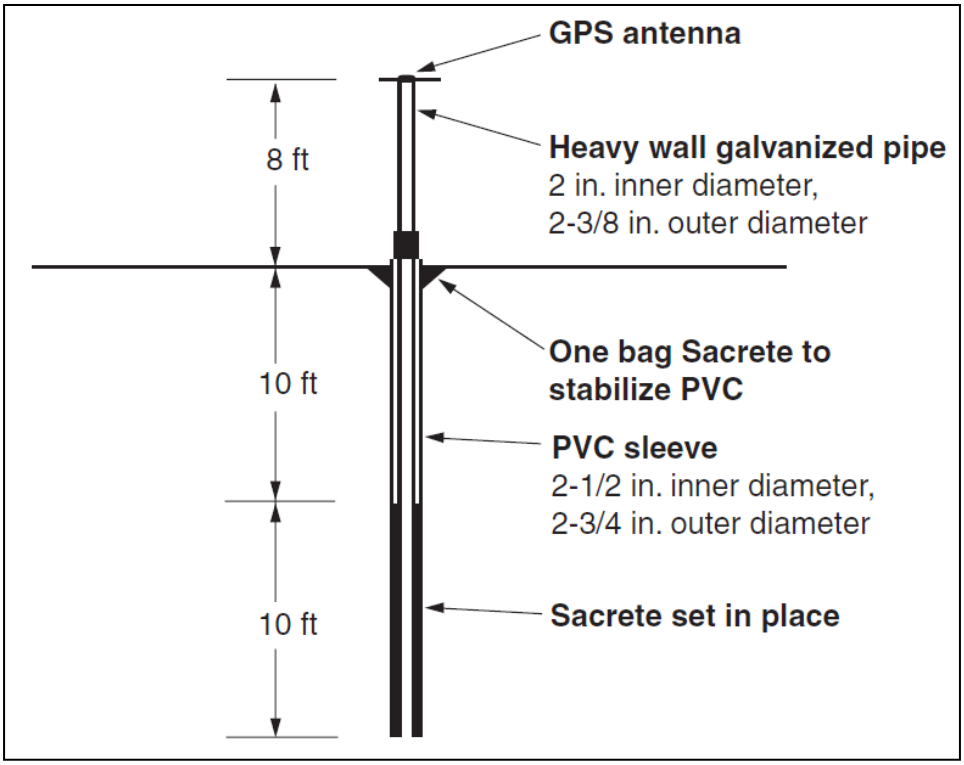

Figure 2.3: Diagram of PAM station. Sacrete is a mixture of concrete material minimizing the shrink-swell effects of clays in the upper few feet of the strata. As the borehole extensometer the inner pipe of PAM monument is isolated from its surroundings (Zilkoski, et al., 2003).

2.1.3 GPS Data Acquisition and Processing

The GPS data were acquired directly from the ftp site (ftp.subsidence.org) and representative of HGCSD. The data from 2007 through 2011 downloaded from ftp site are in Trimble format (*T00 and *T01). The data before 2007 obtained from HGCSD representative are in Receiver Independent Exchange (RINEX) format. The obtained data contain both Port-A-Measure (PAM) and Continuous Operational Reference Stations (CORS). For this research, data from 2002 through 2011 were processed for 5 CORS and 18 PAM sites. Three of these CORS, Addicks (ADKS), Lake Houston (LKHU), and

Northeastern Treatment Plant (NETP), were used as reference stations to find the displacement in each station.

Initially, the stability of the reference stations (ADKS, LKHU, and NETP) was tested using the Automatic Precise Positioning Service (APPS) (http://apps.gdgps.net) by National Aeronautics and Space Administration's (NASA) Jet Propulsion Laboratory (JPL) and online GPS data processing service provided by Geoscience Australia (AUSPOS) (http://www.ga.gov.au/earth-monitoring/geodesy/auspos-online-gps-processing-service.html). These web based services provide processing for uploaded GPS observation files in through their web sites and the reports of the results are send back to the user via e-mail. APPS uses GIPSY-OASIS software working with precise positioning technique (PPP) (Gao et al., 2006). The AUSPOS use Bernese Software System for processing GPS data. Unlike APPS, AUSPOS is processing data using double difference method (Ehigiator–Irughe et al., 2012). The data of the three CORS were uploaded in these two online services from 2002 through 2011. The results of all three stations show that the surface deformation at each GPS stations is very small (<0.1 cm) (Figure 2.4). Therefore, it was decided that ADKS, LKHU, and NETP GPS sites are stable in vertical component and can be used as reference stations for further GPS processing.

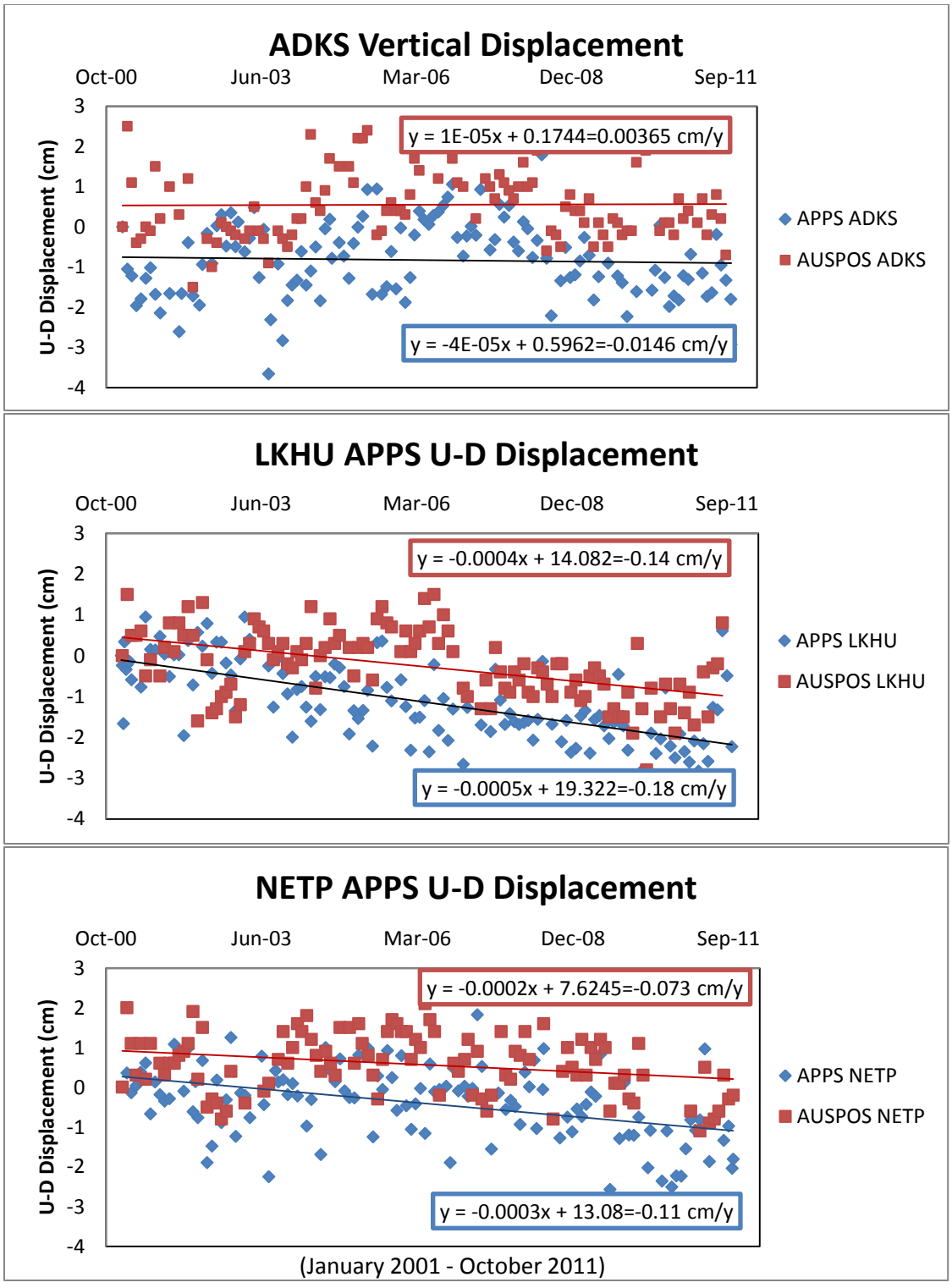

Figure 2.4: Results of APPS (blue points) and AUSPOS (red points) for ADKS, LKHU, and NETP. The results of APPS and AUSPOS are almost similar. Both results represents that ADKS, LKHU, and NETP are stable CORS, and they can be used as reference stations.

For GPS, processing GPS data in Trimble format (*T00, *T01) were converted to GPS observation file format (*Xo- 'X' stands for the year that data was recorded) and navigation file format (*Xn) using the "Convert to RINEX" tool of Trimble Navigation Limited (Figure 2.5). The observation file contains the information about the record data, antenna type, and 30-second periodic data records. These observation files were grouped according to their antenna type, the year of data, and station number. A script written in Python by Huang (2012) was modified to group the large number of GPS files. The folder of these grouped files were zipped using 7zip program in order to upload each folder to Online Positioning User Service (OPUS).

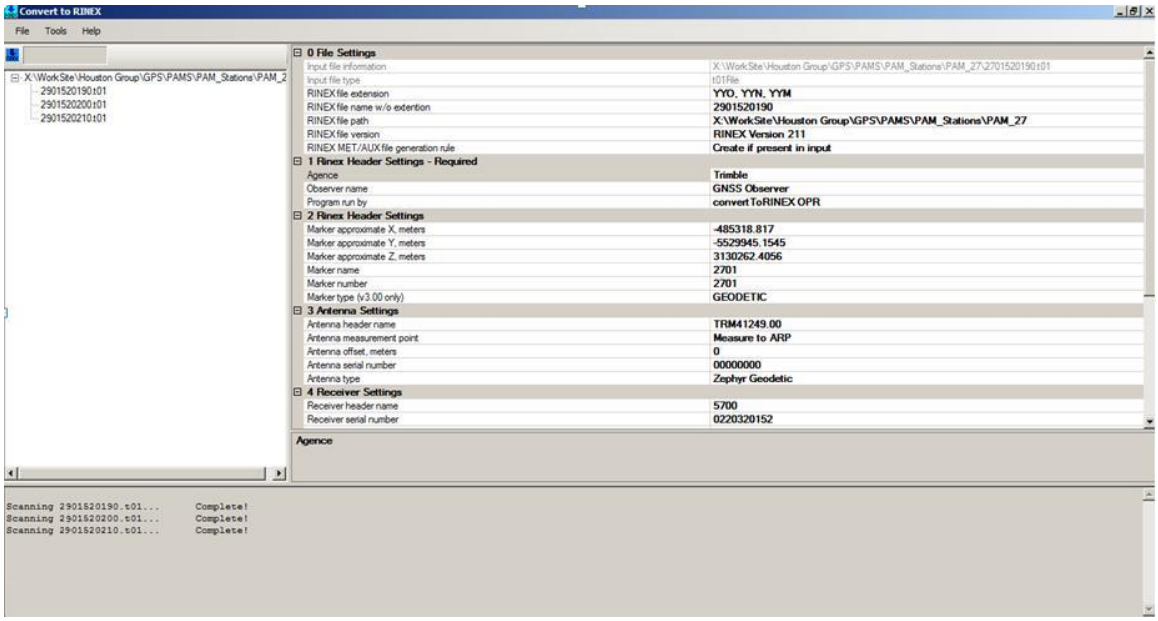

Figure 2.5: Convert to RINEX tool. This tool allow users to convert raw GPS data (T00 and T01 Trimble format) to GPS observation (*Xo-X represents the year that data collected) and navigation (*Xn) files used for GPS processing.

Zipped folders of each GPS stations were uploaded to Online Positioning User Service (OPUS) (Figure 2.6). This service is operated by National Oceanic and Atmospheric Administration (NOAA). This free online processing service provides an access to National Spatial Reference System (NSRS) coordinates with high accuracy (Wang & Soler, 2012). There are two processing options for GPS data: i) Rapid-Static for the data recorded less than 2 hours and more than 15 min. and ii) Static for the data recorded between 2 and 48 hours. For Rapid-Static processor the system is uses RSGPS (Rapid-Static GPS) rapid-static software. The OPUS processes the GPS data in Program for the Adjustment of GPS Ephemerides (PAGES) by NGS for the Static option. In this research, the Static processor was used for the daily recorded GPS data.

Uploading data to OPUS system includes 5 steps (Figure 2.6). For the first step, the created zipped folder was uploaded to the system. Then, the antenna type of the GPS was defined to OPUS in order not to allow the system to process data with a null model. The third step is the selection of three reference stations. These reference stations could be selected automatically by OPUS; however, one of the stations selected by OPUS has experienced subsidence according to Wang (in press, 2013). Therefore, ADKS, LKHU, and NETP were selected as reference stations manually in order to process the GPS data. After that, the email address is defined to system to get the reports of the solutions back. Finally, the processor is selected in terms of the duration of the data record. The antenna height box was ignored for this study assuming that the GPS were located on the land surface.

Figure 2.6: The Snap shot of Online Positioning User Service (OPUS). This figure represents the steps of uploading GPS data for processing. First GPS data loaded to online processing system. The antenna type of the GPS station is selected in the second step. Then, antenna height of the GPS is entered. The email address used for processed report is typed to system. The reference stations for processing are selected at the fifth step. Finally, the GPS data is uploaded to the system.

The solution report of the GPS data includes the information about the location of the GPS in x, y, and z axes in different coordinates and reference frames. To avoid the unnecessary information, a macro was written using Microsoft Office Excel. The solution

reports sent by OPUS were combined into a text file by a tool of Outlook software. Important information for each GPS stations was extracted from the created text file using Excel macro.

In order to calculate the surface deformation from GPS solution, the datum of the first recorded date was assumed as the base datum, in other words, starting point of the deformation. The data recorded in subsequent days were subtracted from this first datum to realize the deformation between each day. The differences of the ellipsoid height of the days were plotted into a height difference versus time graph. The rate of the deformation was calculated from the trend of the plots. Same steps were followed for northing and easting of GPS stations.

To increase the precision of GPS results, the data were selected according to the following information suggested by NGS (National Geodetic Survey, 2012b): i) >90% observations used, ii) > 50% ambiguities fixed, iii) overall RMS < 3 cm, and iv) peak to peak errors <5 cm.

2.1.4 Surface Models of GPS

The surface deformation rates of all GPS stations were plotted and evaluated using ArcGIS 10 software by Environmental Sciences Research Institute (ESRI). The surface model of the GPS results was generated using different interpolation techniques under Spatial Analysis Tool of ArcGIS software. Three interpolation methods utilized in this study are: i) Kriging, ii) Inverse Distance Weighted (IDW), and iii) Natural Neighbor.

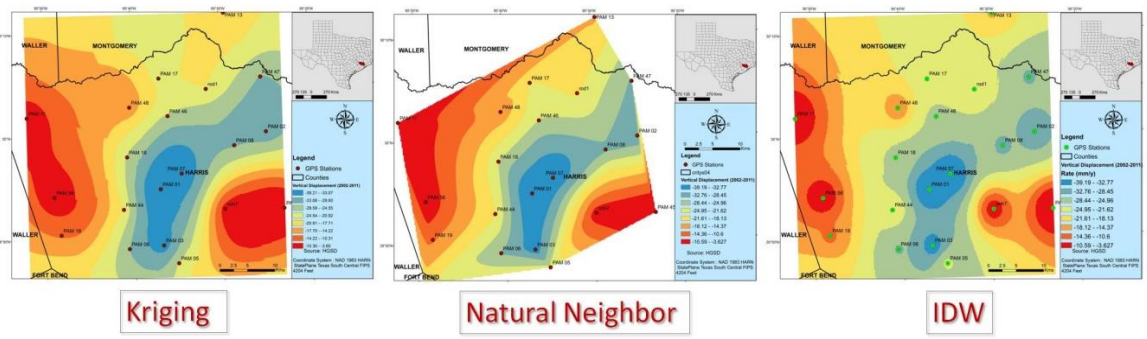

Figure 2.7: Evaluation of three interpolation techniques Kriging, Natural Neighbor, and IDW. All three interpolations demonstrate realistic values for the study area. However, the Natural Neighbor does not extend the area that IDW and Kriging do. IDW surface has bull eyes features which does not show continuity and seems unnatural. Kriging interpolated surface both represents continuity and covers wide extend of the study area.

2.2 LiDAR

2.2.1 Introduction

LiDAR (**Li**ght **D**etection **a**nd **R**anging) is an active remote sensing technique which uses light pulses to collect information about the Earth's surface (NOAA, 2008). The main purpose of this airborne remote sensing system is to find out the distance between the target and instrument by measuring the travel time (Fowler, 2001). The LiDAR data are result of: i) the time difference between the emitted and returned laser pulses, ii) the angle of the source, and iii) the location of the sensor (NOAA, 2008). These three components are provided from the laser sensor (LS), the Internal Measuring Unit (IMU) or Inertial Navigation Systems (INS), and Global Positioning Systems (GPS) (Figure 2.8).

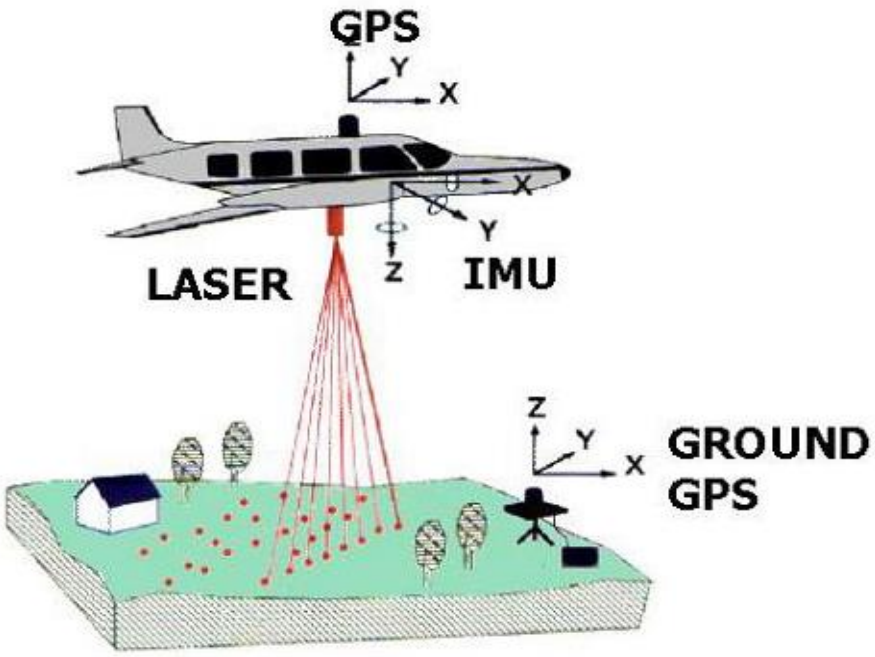

Figure 2.8: Components of Airborne LiDAR System (FEMA's Cooperating, 2003)

LiDAR data are capable of reserving multiple returns (up to 5 returns) for each pulse due to the penetrating ability of the laser beam through forest canopy and vegetation (NOAA, 2008) (Figure 2.9). This property of LiDAR is both an advantage and a disadvantage for creating a bare-earth surface with respect to the vegetation density. The bare-earth surface is a model that is created by the returns reflected from the ground directly. To differentiate this return from others reflected from buildings or vegetation, some filtering methods are applied (Sithole & Vosselman, 2004). The way of classifying returns is to use the GIS location of the buildings and aerial photos (Engelkemeir & Khan, 2008).

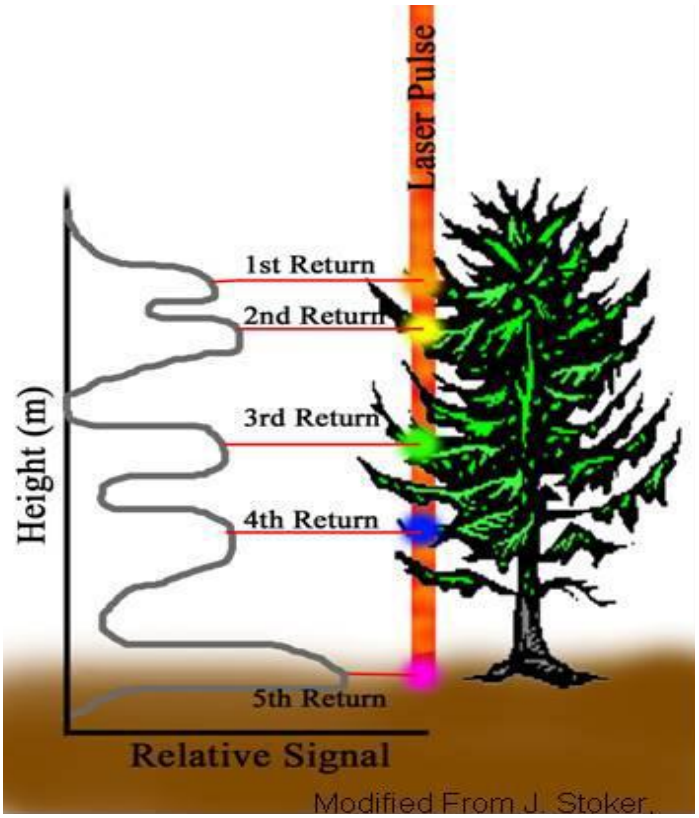

Figure 2.9: Shema of multiple returns from a single LiDAR pulse (NOAA, 2008).

Digital Elevation Models (DEMs) are generated from the bare-earth data of LiDAR. The DEM is created by using Triangulated Irregular Network (TIN) which has neither overlaps nor space while generating the grids of DEM (Engelkemeir, 2010). The LiDAR DEMs are able to use for subsidence studies (Froese & Mei, 2008).

2.2.2 LiDAR Data of Northwest Harris

In this study, two LiDAR datasets from 2001 and 2008 were used for the northwest Harris area. LiDAR 2001 data were collected by Terrapoint LLC and 2008 data were collected by Merrick & Company (Meyer, 2002; LaBarbera, 2012). The purpose of both

sets of data was to recognize the areas of high flood risk in Harris County (Kasmarek et. al., 2009). Their horizontal datum is D_North_American_1983_HARN (NAD83 HARN) with horizontal accuracy ±75 cm for 2001 data and ±70 cm for 2008 data. The vertical datum is North American Vertical Datum 1988 (NAVD88) with the accuracy ±15 cm and ±9.25cm for 2001 and 2008 data, respectively.

Two DEMs were created using 2001 and 2008 LiDAR datasets. Although the LiDAR data were filtered the created DEM has some artifacts over the elevation. The resolution of 2001 and 2008 DEMs are 3x3 meters and 1.5x1.5 meters, respectively (Meyer, 2002; Engelkemeir & Khan, 2008).

2.2.3 Digital Elevation Model (DEM) Generation

Digital Elevation Model (DEM) is a raster which contains digital geographic dataset of elevation in xyz coordinates. To create DEM, the raw LiDAR data (**L**ong **A**SCII **S**tandard -LAS) were used. At the first step, the point spacing of raw data was examined using Point File Information tool in ArcMap 10 (Figure 2.10). It was seen that the average point spacing for each tile was around 4 feet. The LAS data were converted to multipoint holding information in xyz coordinates using LAS to Multipoint tool (Figure 2.11). The average point spacing for each tile was set to 6 feet to prevent information deficiency. Also, the return value of the classified LiDAR points for creating bare-earth model, or DEM, was defined in the tool.

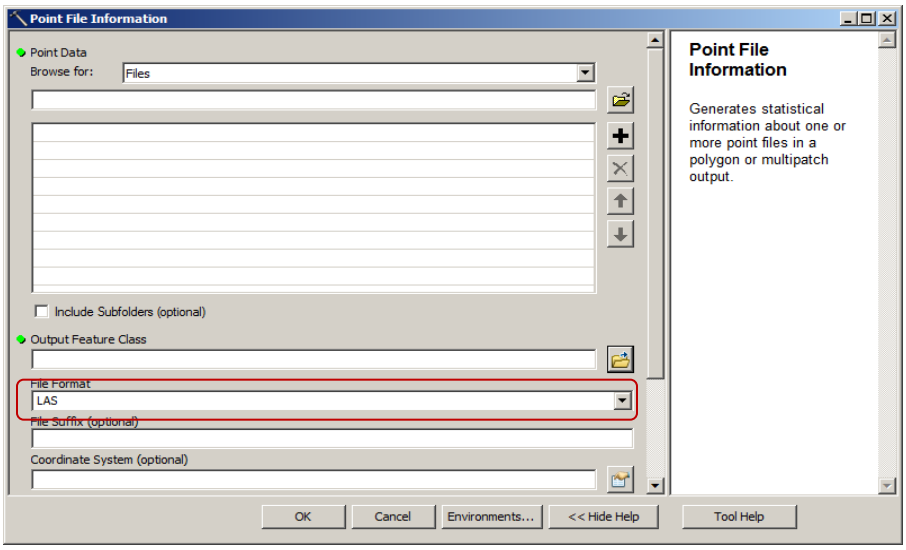

Figure 2.10: Point File Information tool. The red box on the tool is to show file format that is used to create point cloud.

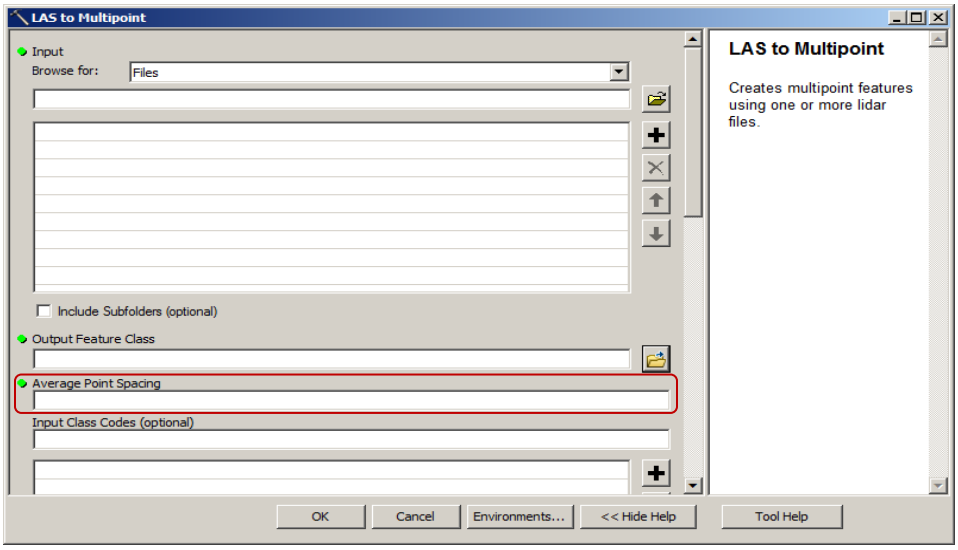

Figure 2.11: LAS to Multipoint tool. Rectangle in red shows the average point spacing where the distance between two LiDAR points is entered.

After point cloud was created, **T**riangulated **I**rregular **N**etwork (TIN) surfaces were generated from these point clouds using create TIN tool inArcMap 10 (Figure 2.12). The Height Field needed to set as z points to get a surface elevation model. In the following step, the conversion tool- TIN to Raster- was utilized to generate the DEM raster for each

tile. After completion of DEM generation for each tile, tiles were stitched into a single large raster demonstrating the regional DEM for northwest Houston using Mosaic Tool in ArcGIS 10.1.

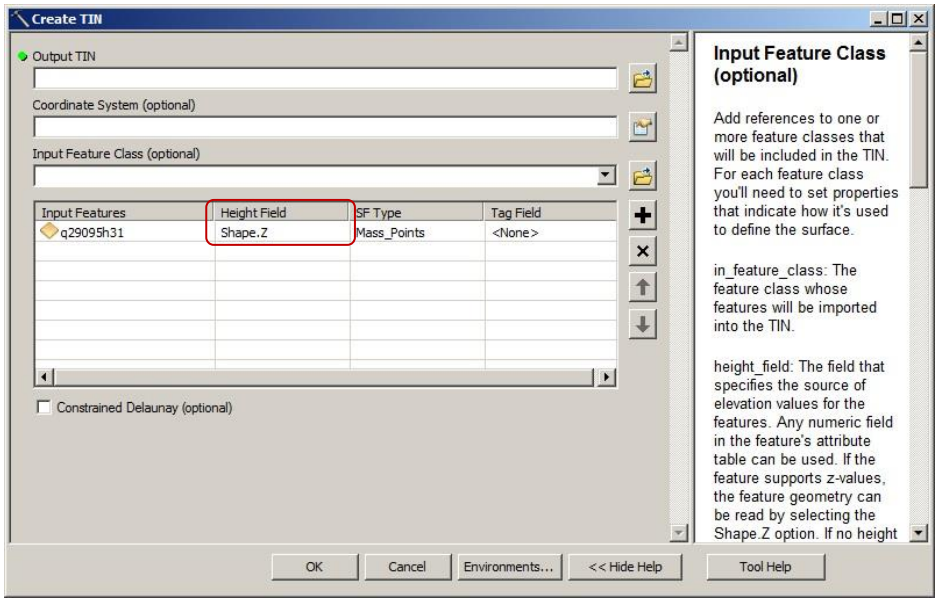

Figure 2.12: Create TIN tool. The red box points the height field part in the tool where the elevation data is mounted to create DEM.

2.2.4 Zonal Statistics Method

This technique was first applied by Engelkemeir (2008) to calculate scarp height. In this study, the change in DEM height was computed to assess the subsidence rate between 2001 and 2008. This technique was accompanied by assuming an average elevation within a defined polygon to get an acceptable elevation (Engelkemeir & Khan, 2008). Forty one (41) polygons were created for the study area. It was decided to divide the northwest Harris area into three parts: center, north, and south. Twenty of the polygons cover the center of study area where the subsidence assumed to be the highest. While creating the polygons, LiDAR DEM artifacts were avoided.

Several steps were applied for this method including some of Engelkemeir's (2008) methods for polygon computation except the custom tools for creating polygons. In this case, another method was used for creating polygons in ArcMAP 10.

Initially, in order to create polygons with equal space, the Create Fishnet tool in Data Management was used. After creating fishnet, a shape file (*Hockleyzone*) was generated (Figure 2.13). Because of the large extent of the study area, it was decided to create each polygon covering ~550 m^2 area. By using Editor Tool, each polygon was digitized with the guidance of fishnet. It was important to avoid artifacts, such as buildings and streets, and streams while creating polygons to get better results. Therefore, they are not uniform (Figure 2.14). At the same time, the number of each polygon was assigned manually in Editor Tool. The approximate values for mean, median, mode, and standard deviation (STD) were calculated using Zonal Statistics as Table tool in ArcMAP 10. The zonal statistics table was created for both 2001 and 2008 LiDAR DEMs using the same shape file. Each zonal statistics tables were plotted into an Excel sheet. By using the mean values of each polygon, difference between 2001 and 2008 was calculated. The approximate difference in this time span was computed averaging the difference of all zones.

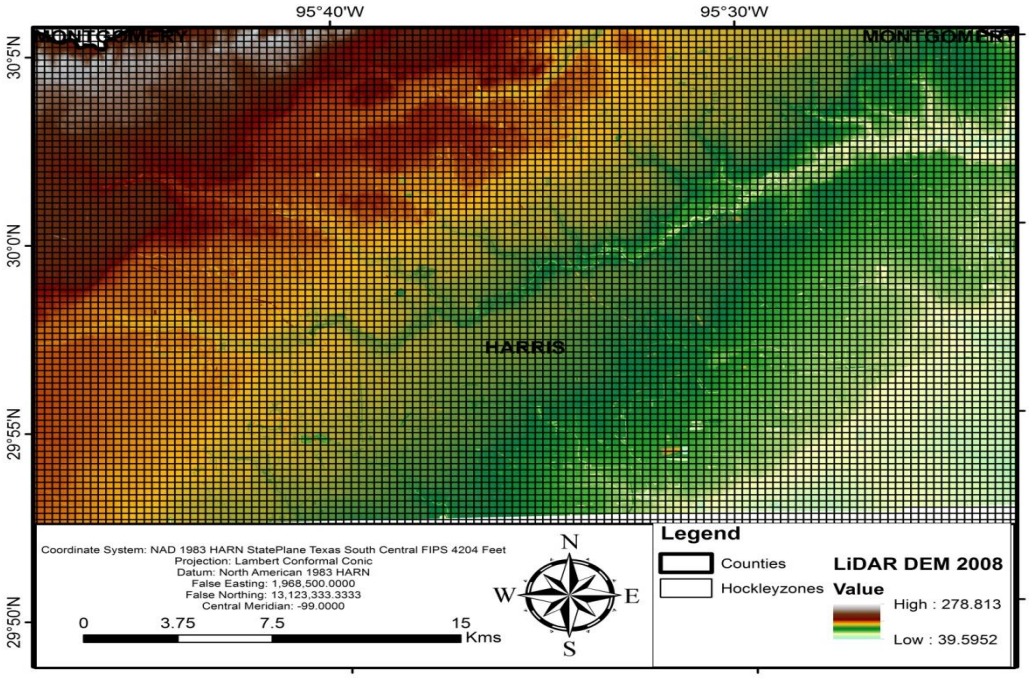

Figure 2.13: Created fishnet-*Hockleyzone*.This is an evenly spaced 550 by 550 m^2 grid for Northwest Harris County. Behind the *Hockleyzone* grids, the DEM of the Northwest Harris is displayed.

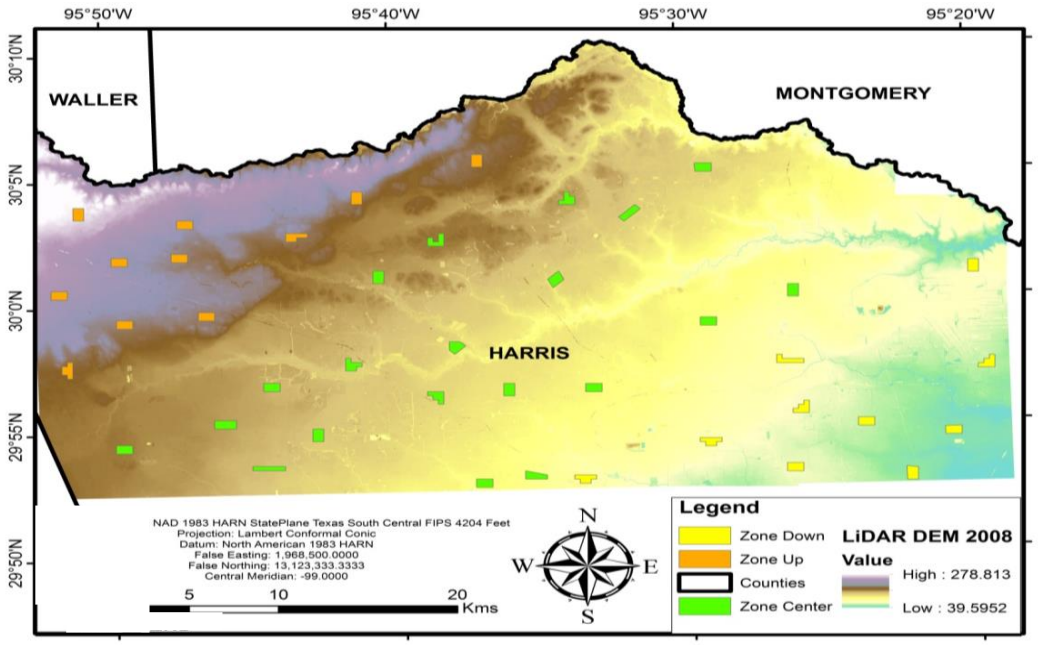

Figure 2.14: Polygons for Zonal Height Computation method. Polygons in orange are for the north part, polygons in green are for the central part, and polygons in yellow are for the south part of the study area. These polygons were divided into three parts to correlate with GPS results. The DEM of the Northwest Harris is also displayed.

2.3 InSAR

2.3.1 Introduction

Synthetic Aperture Radar (SAR) is an active remote sensing technique which uses microwave signals. This technique; therefore, can provide an image either day or night as an active system. The microwave beams can also penetrate clouds, fogs, soil, snow, and vegetation (partially) (Bamler & Hartl, 1998; Curlander & McDonough, 1991). The principle of the SAR systems is to transmit a radar pulse to target, receiving the reflected signal (Figure 2.15) (Chan & Koo, 2008). In other words, it records the amplitude and phase of the backscattered signal (Bamler & Hartl, 1998).

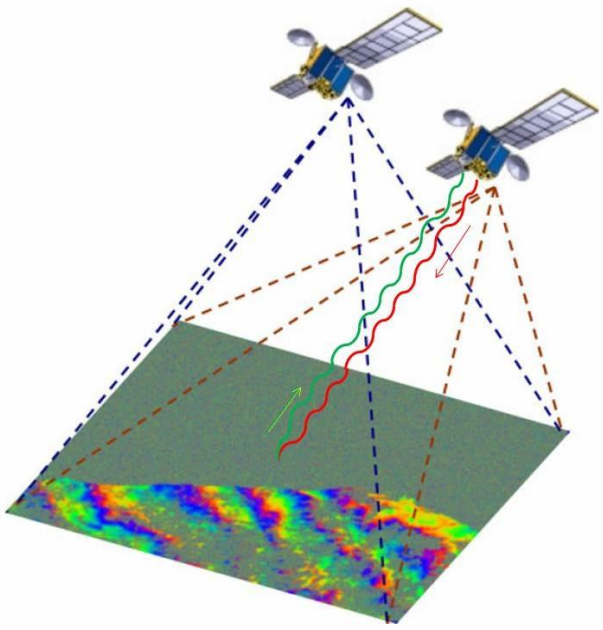

Figure 2.15: Synthetic Aperture Radar (modified from Tarikhi, 2010). It explains the principle of SAR systems. Red line demonstrates the radar pulse from instrument to target, and green line is for the signal target to recorder.

2.3.1.1 ERS

European Remote Sensing (ERS) satellites were first two satellites of European Space Agency (ESA). ERS-1 was launched in 1991. It is a Sun-synchronous satellite at 782-785 km altitude. It carried five different instruments with diverse purposes; radar altimeter (RA), along-track scanning radiometer (ATSR-1), synthetic aperture radar (SAR), i.e., active microwave instrument (AMI), wind scatterometer, and microwave radiometer (MWR). It had three different repeat cycles for mission phases; 3-day, 35-day, and 168-day. On March 2000, there was a failure of the ERS-1's computer and gyro control (ESA, 2011).

ERS-2 was launched on April, 1995 from French Guiana. It shared the same orbital plane with ERS-1. ERS-2 had two more instruments in addition to ERS-1. These two instruments are global ozone monitoring experiment (GOME), along-track scanning radiometer (ATSR). ATSR is the only passive instrument on the satellite. The repeat cycle of ERS-2 was 35 days. In February 2001, the gyroscope of the satellite was broken, and it continued to operate till September 2011 (ESA, 2012).

These two satellites have C-Band SAR system with 56.6 mm (5.3 GHz.) wavelength, and vertical-vertical (VV) polarization.

2.3.2 SAR Interferometry

SAR interferometry (InSAR) is one of the remote-sensing tools to measure the displacement and deformation on the earth surface. In the InSAR principle, two SAR images are acquired over the slightly different location, at first. The phase difference

between these SAR images is calculated. This phase difference is named as 'interferogram'. An interferogram is calculated using the equation below (Reigber et al., 2007; Raucoules et al., 2007; Osmanoglu et al., 2011).

$$\Delta\varphi = \varphi_{topo} + \varphi_{flat} + \varphi_{diff.} + \varphi_{err} + \varphi_{atm.} + \varphi_{noise}$$

where φ_{topo} stands for phase of the topography, φ_{flat} is for the flat-earth phase created by the imaging geometry, $\varphi_{diff.}$ refers to the surface deformation, φ_{err} means the error caused by inaccurate orbit and topographic information, $\varphi_{atm.}$ is for the atmospheric effects, and φ_{noise} denotes the noise of the phase.

By wrapping and unwrapping the interferogram respectively, the information about the topography can be recognized from absolute phase. The deformation over the large areas can be identified analyzing the absolute phase. This method is named as Differential SAR interferometry (DInSAR). In recent time, millimeter-scale deformation can be detected using DInSAR technique (Goldstein et al., 1993; Massonnet & Feigl, 1998; Bamler & Hartl 1998; Mouratidis et al., 2010). There are different analysis techniques for DInSAR: normal DInSAR (2-pass), dual-pair differential interferometry (3-pass or 4-pass), and persistent scatterer interferometry (n-pass).

2.3.3 Data Acquisition and Processing

Eight (8) ERS1 and seventeen (17) ERS2 sets of data from 1992 through 2002 were obtained for this study. All acquired SAR data were Level 0 type data in Committee on Earth Observing Systems (CEOS) format with its leader and data file. A CEOS format

contains the mix of binary and American Standard Code for Information Interchange (ASCII) code information.

The Level 0 CEOS data is a formatted version of raw satellite data. The raw Level 0 data were preprocessed converting to geocoded Level 1 type data in SARScape module of ENvironment for Visualizing Images (ENVI) software (Figure 2.16). To import and prepare Level 1 data, the Preliminary orbit product (PRL) was downloaded for each ERS data from the Earthnet Online server of the ESA. The PRL data contains information about Single-Lens Reflex (SLR), radar altimeter height, ERS PRARE range and doppler data for the satellite. The PRL file for each ERS SAR data was defined to ERS/JERS importing and focusing tool under SARScape module to get the Level 1 type data.

The 25 ERS Level 1 data were processed using persistent scatterer method in ENVI SARScape module.

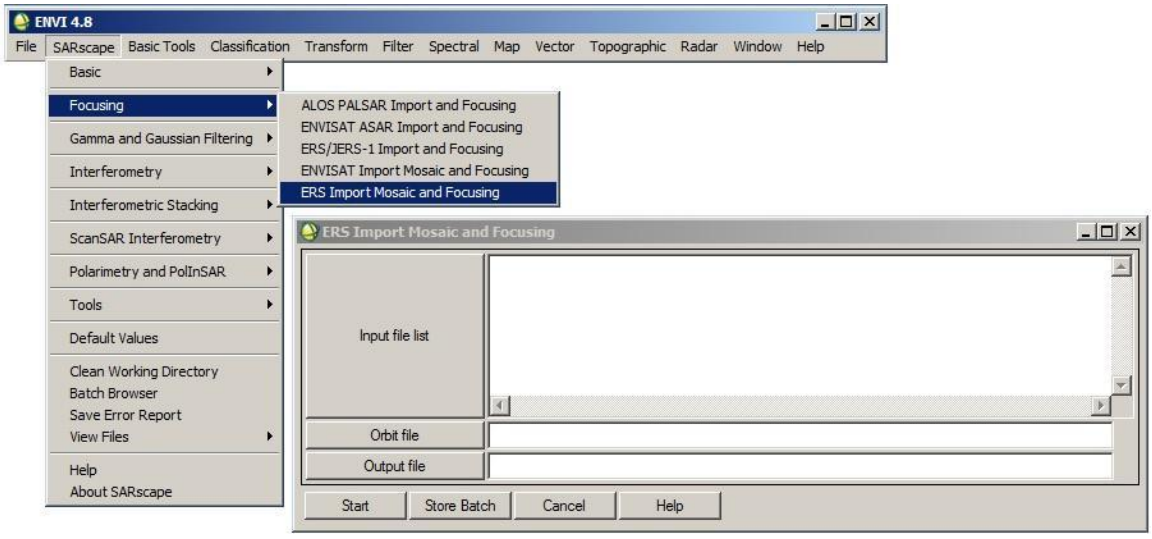

Figure 2.16: ERS import mosaic and focusing tool, and SARscape module in ENVI. This tool allows converting Level 0 ERS data to Level 1 ERS data.

2.3.3.1 Persistent Scatterer

InSAR is one of the cost-efficient techniques to detect the centimeter-scale surface deformations. It has some contradictions of generating an interferogram, however, due to anomalies caused by geometry of image, vegetation, and atmospheric effects. Persistent Scatterer, or Permanent Scatterer, InSAR (PSI) is one of the recent SAR interferometry techniques reducing these atmospheric and topographic errors (Kuehn et al., 2009). The principle of PSI is processing persistently backscattering objects which have high reflectance with iterative estimation of phase differences (Ferretti et al., 2001; Hooper et al., 2004). Therefore, it provides high ground motion results from these objects which generate pixel base products. To approach the PSI results, large numbers of images is needed to correlate them with one master image (Lauknes et al., 2005). This technique gives the best results in urban areas.

In this research, PSI method was applied on 25 ERS images from 1992 through 2002 due to reduce the anomalies of C-Band caused on Houston area. For PSI processing, these steps were followed in Persistent Scatterer (PS) tool under SARScape module of ENVI 4.8;

1. *PSI data Input*: Preprocessed 25 SAR ERS data were inputted into the Input file list part of Persistent Scatterer tool. All 25 ERS Level 1 data were in Single Look Complex (SLC). Before assigning the reference (Master) image, the directory of the output data was specified to the tool and a sub-directory was created named as "*Rootname_ps_work_dir*" into the directory folder. This sub-folder is for the iteration of the processing data. The Reference (Master) file can be selected

automatically in this tool. However, the master image was chosen manually in this research.

2. *Generating Digital Elevation Model (DEM)*: The DEM for processing PSI is a must for InSAR processing. It is used not only to correct topographic anomalies, but to specify the geographic location of the ERS data. The DEM of the research area was generated using the "Digital Elevation Model Extraction" tool of the SARScape module. The SRTM-3 version 4 was selected to extract. All of the ERS data were inputted, and the cartographic system was defined before extracting the DEM. The extracted DEM file was defined to the "Persistent Scatterer" tool.

3. *Creating Area of Interest (AOI) Vector*: The Area of Interest (AOI) vector is mandatory to process a specific area into the ERS image. This AOI vector was created using "Create New Vector" tool of ENVI program. The AOI vector was prepared as an area covering at most 4 million pixels. Since, the PS tool can process less than 4 million backscattered points. The created AOI vector was plotted to the PS tool.

4. *Parameters of PS Tool and Process*: The coherence coefficient is an important parameter for Differential InSAR processing to define the normalized complex cross correlation between the images. The higher the coherence coefficient, the

more precision of the results. The coherence threshold of the PS tool was defined as 0.75 to process more points. The tool was run after setting the all of above steps.

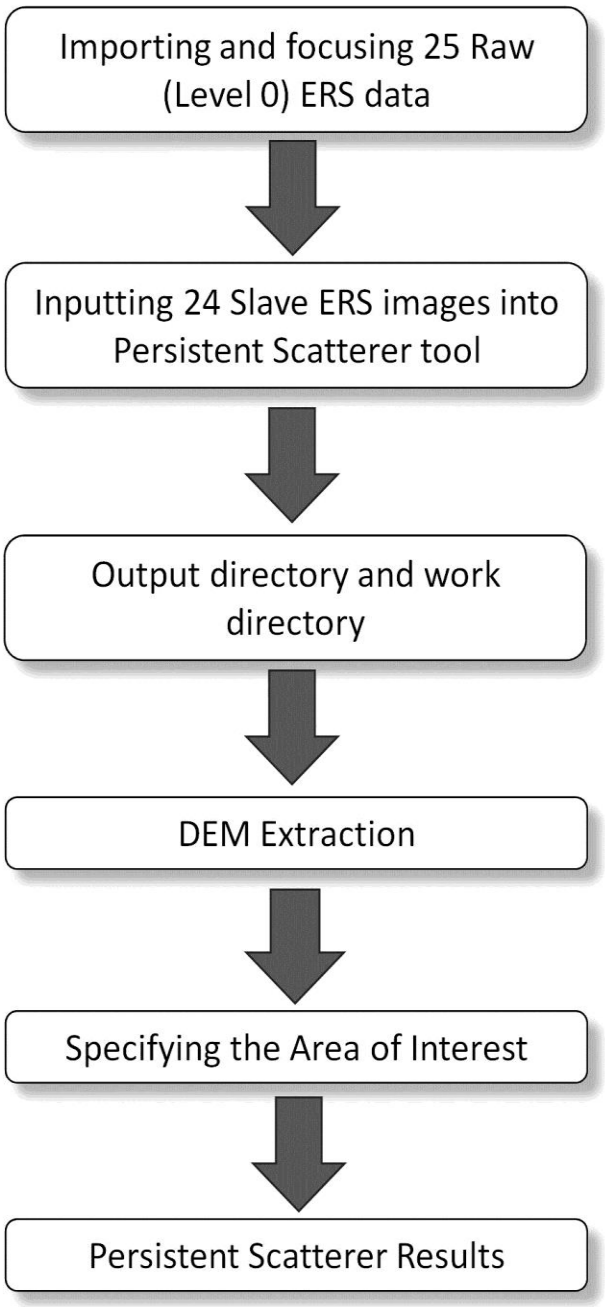

Figure 2.17: Flowchart of Persistent Scatterer InSAR processing

2.4 Groundwater

2.4.1 Introduction

The excessive usage of water from the systems is believed to cause the sinking of the land surface in the Greater Houston area, Texas (specifically in Harris County). One of the major aquifer systems of Texas that is supplying water for Harris County is Gulf Coast Aquifer (Figure 2.18) (Ashford & Hopkins, 1995). This aquifer system is composed of interbedded clays, silts, sands, and gravels (Chowdhurry, 2006). The Gulf Coast Aquifer system has four major aquifers, which are the Chicot, Evangeline, Jasper, and Catahoula Aquifers (Figure 2.19) (Ashworth & Hopkins, 1995). The Chicot is the topmost aquifer which consists of interbedded low permeable clays with sands. The Evangeline Aquifer lying below the Chicot Aquifer is formed by two important sand formations (Lefebvre, 2010). The Jasper and Evangeline Aquifers are separated by Burkeville confining layer. The deepest aquifer Jasper comprise of sandstone which brings the permeable characteristics (Ashford & Hopkins, 1995).

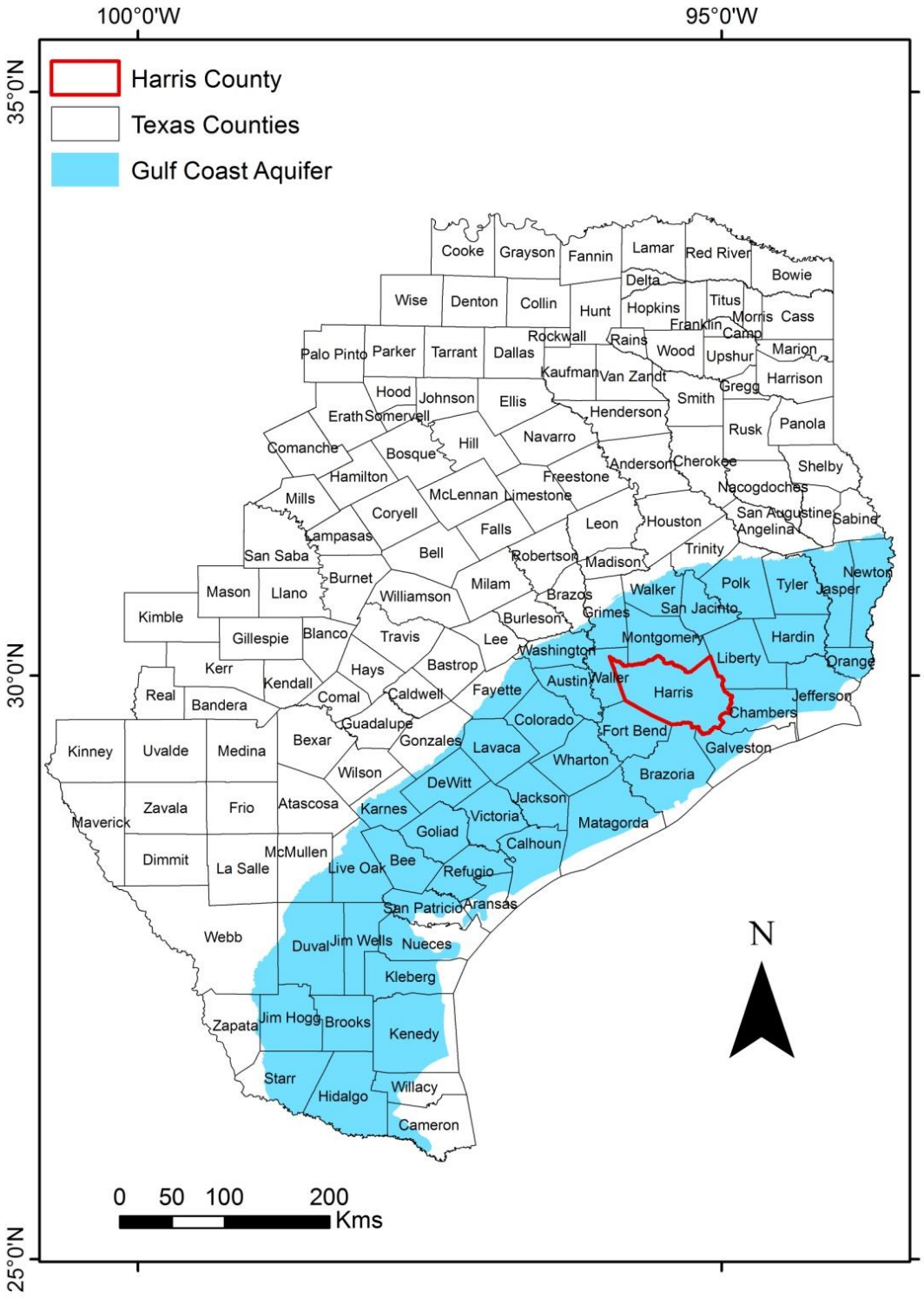

Figure 2.18: Gulf Coast Aquifer. The blue colored area represents extend of Gulf Coast Aquifer system in Texas. The red colored area demonstrates location of the Harris County.

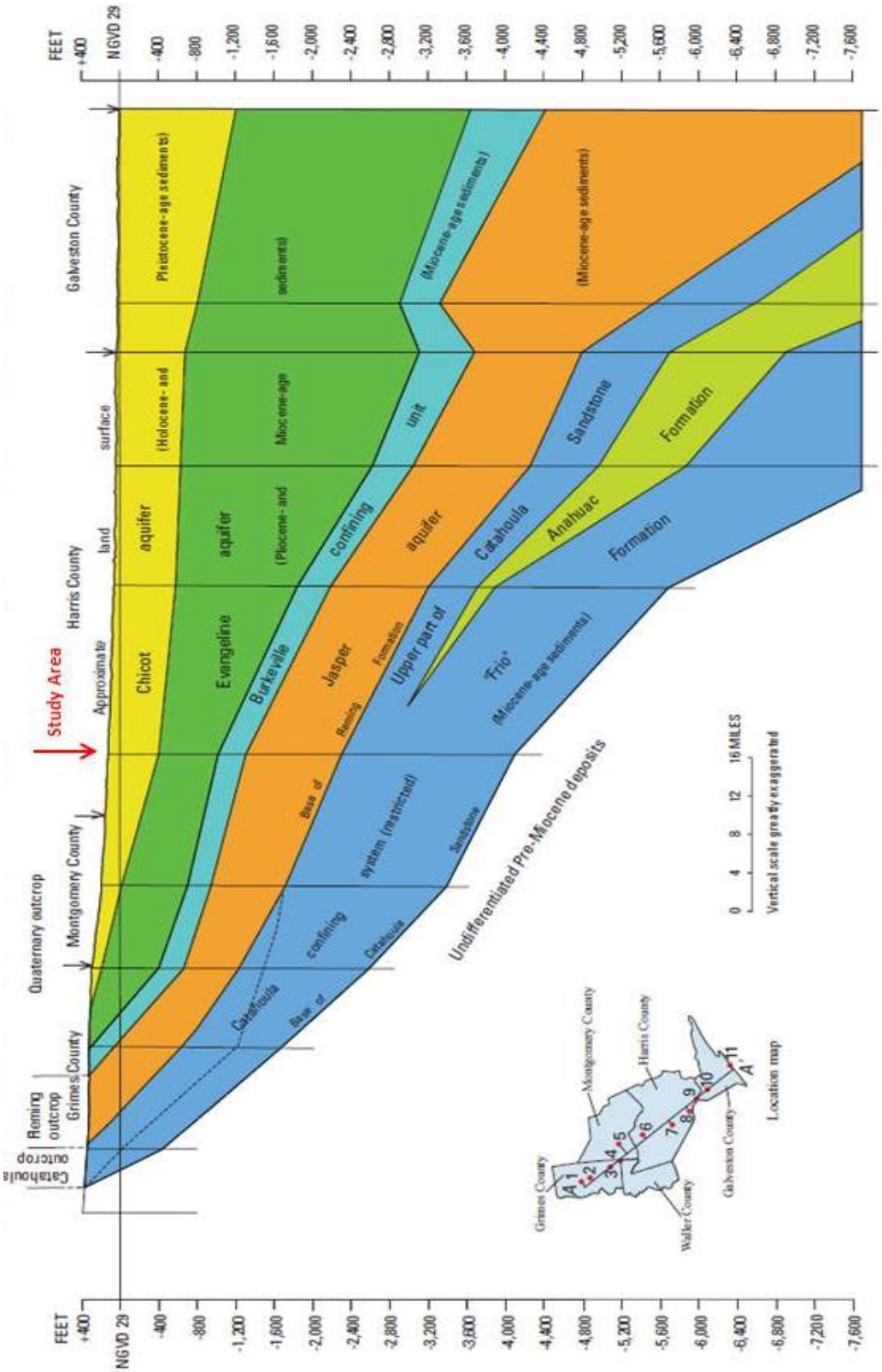

Figure 2.19: This image represents the cross section of Gulf Coast Aquifer system from the Grimmes County through the Galveston County. The red arrow points out the locality of study area (modified from Bawden et al., 2012).

The water demand for Harris County has been fulfilled from these three aquifers for many years: Chicot, Evangeline, and Jasper. The demand for water is not only for municipal purposes, but also for industrial activities and irrigations of fields. The water level of the aquifer declines as the groundwater recharge rate becomes lower than the amount of water extraction from the aquifer. When groundwater level drops below the preconsolidation stress threshold, the deposits with fine-grained sediments, e.g. silt and clay, cause permanent subsidence due to inelastic compaction (Galloway et al., 1999) (Figure 2.20). The water level drop leads compaction of the sediments. In other words, subsidence takes place by means of the compaction of the sediment layer of these aquifers.

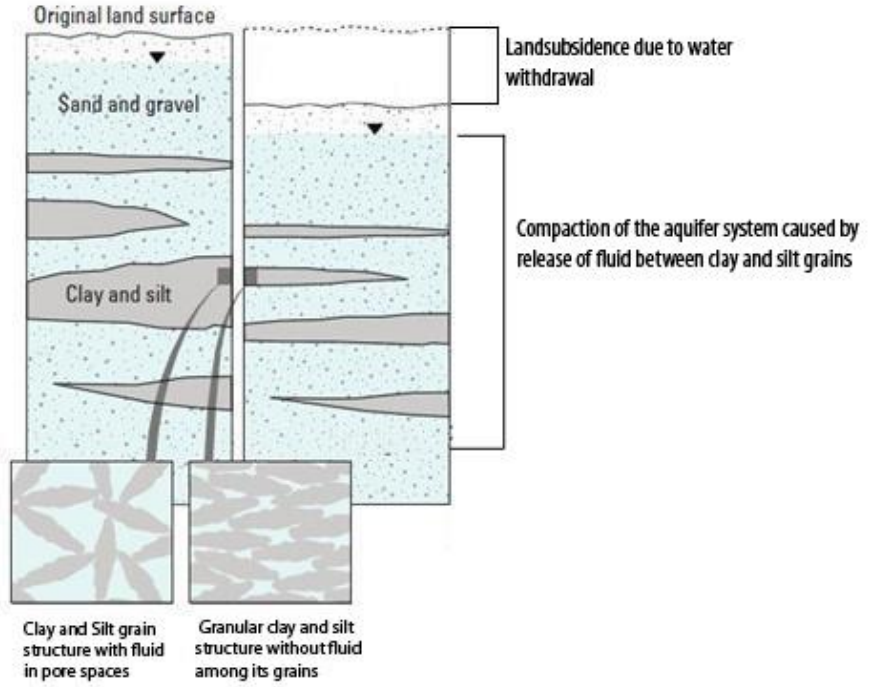

Figure 2.20: Cartoon for the mechanism of subsidence in an aquifer which includes sands and gravels with interbedded silts and clays (modified from Galloway et al., 1999). Small sketches at the bottom left corner demonstrate granular structure of the aquifer before and after the water releasing.

2.4.2 Gulf Coast Aquifer System

The Gulf Coast aquifer lies along the coastal part of the Gulf of Mexico (Ashford & Hopkins, 1995). It extends from Mexico border to Louisiana border in Texas (Figure 2.18). In Texas, more than 1.3 billion cubic meters of groundwater are withdrawn from this aquifer (Chowdhury & Turco, 2006). According to Ashford & Hopkins (1995), 90 percent of the pumped water is used for drinking water and agricultural activities.

The Gulf Coast aquifer is formed by mixed interbedded clays, silts, sands, and gravels (Sellards et al., 1932; Ashford & Hopkins, 1995). The sediments of this aquifer were deposited in the fluvial-deltaic and shallow-marine environment between Miocene and Pleistocene (Chowdhury & Turco, 2006). This aquifer system consists of five hydrological units: (i) the Chicot aquifer (at the top), (ii) the Evangeline aquifer, (iii) Burkeville confining layer, (iv) the Jasper aquifer, and (v) the Catahoula aquifer (at the bottom). These hydrological units were classified by Baker (1979) in terms of hydraulic and facies properties.

2.4.3 Aquifers of Study Area

The Northwest Houston area lies over the two important aquifers of the Gulf Coast aquifer system: the Chicot aquifer, and the Evangeline aquifer.

2.4.3.1 The Chicot aquifer

The Chicot is the uppermost aquifer of the Gulf Coast aquifer system. The thickness of the Chicot aquifer is 1200 feet (~366 meter) near the coastal part of the Gulf of Mexico

and it is thinning towards inland (Chowdhury & Mace, 2003). This aquifer contains the Beaumont, Lissie, Montgomery, Bentley, and Willis Formations, and Holocene alluvium deposits of The Brazos, Trinity, Nueces, and Rio Grande rivers (Ashford & Hopkins, 1995) . These formations and deposits include clay, silt, sand, and gravel with fining upward sequence (LDEQ, 2003). The Chicot aquifer is an unconfined aquifer, i.e., it is not confined by an impermeable substance (Figure 2.21). The property that separates the Chicot aquifer from underlying aquifer is the hydraulic conductivity difference between two aquifers. The lower part of the Chicot aquifer has high hydraulic conductivity due to massive sand component know as Alta Loma Sand (Jorgensen, 1975; Chowdhury & Turco, 2006).

2.4.3.2 The Evangeline aquifer

The Evangeline aquifer is the one of the most important fresh groundwater source for Houston area. It is overlain by the Chicot aquifer and underlain by the Burkeville confining unit (Figure 2.19). The Evangeline aquifer is dipping and thickening (50 to 1900 ft, ~15.2 to ~580 m) towards the Gulf of Mexico. This aquifer is formed by the Miocene and Pliocene aged The Fleming, and Goliad Formations (Baker, 1979). These formations consist of sand interbedded with clay, marl, and caliche (Figure 2.21) (Hosman, 1996; Chowdhury & Turco, 2006).

The clay layer which is at the upper most part of the Goliad Formations separates the Chicot and the Evangeline Aquifers. This clay-rich layer provides confined aquifer characteristic to the Evangeline aquifer (Turcan et al., 1966). However, the groundwater

flows between the Chicot Aquifer and the Evangeline Aquifer, because this clay-rich layer is not thick enough to work as confining unit (Kasmarek et al., 2010). According to Kasmarek et al. (2010), the hydraulic head change in the Evangeline aquifer can influence the water level in the Chicot aquifer due to hydraulic contact.

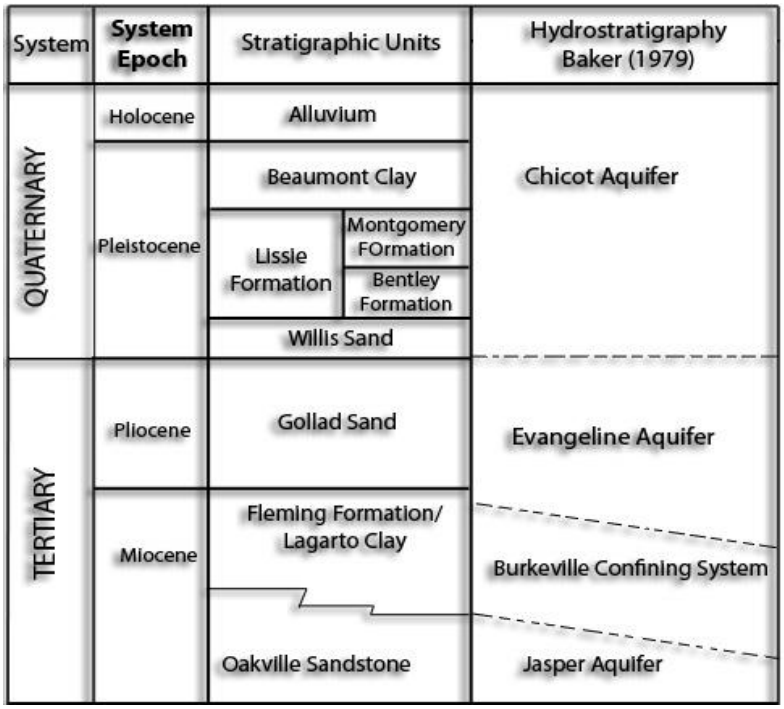

Figure 2.21: Hydrostratigraphic units and its stratigraphy (modified from Baker, 1979).

2.4.4 Data Processing

The historical groundwater observation data were acquired from U.S. Geological Survey (USGS). The following steps were taken to:

i) identify locations of the observation wells in the study area, the information about the well locations was gathered from USGS website (http://groundwaterwatch.usgs.gov/countymaps/TX_201.html), ii) the groundwater level

data of these observation wells based on the National Geodetic Vertical Datum of 1929 (NGVD 29) datum were searched in USGS, iii) the groundwater data were classified in terms of the aquifer systems, and iv) the rate of change in groundwater level was calculated from the trend equation of the graphs of observation well data for long and short term time period.

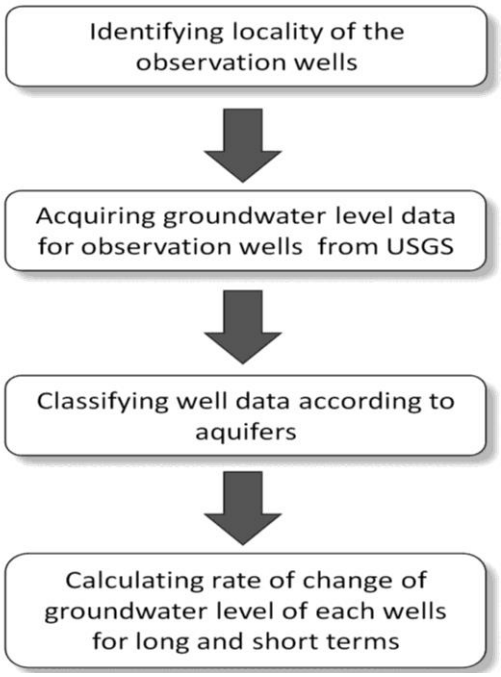

Figure 2.22: Flowchart of data processing of groundwater observation wells.

2.4.5 Groundwater Surface Modeling

The rates of groundwater level change for each well were listed in terms of the well number, latitude and longitude of the well, and its aquifer. The data sheet was imported into ArcGIS 10 software, and the observation wells were plotted using its coordinates. The datum of the observation wells was selected as North American Datum of 1927 (NAD27). After plotting observation wells of each groundwater aquifer, three different

interpolation techniques (Kriging, IDW, and Natural Neighbor) were applied to create a surface model for groundwater level change using the rate of change parameters.

2.5 Hydrocarbon

2.5.1 Introduction

Texas is the one of the prominent oil producing states in the U.S. The hydrocarbon reserves of the Texas region cover 22 percent of oil and 23 percent of natural gas reserves in the U.S. (Kim & Ruppel, 2005). The state is also first in U.S. oil and gas production, which has been important for its economy since 1900s (Worldmark Encyclopedia of the States, 2004). The first oil field, Humble, was discovered in 1905, while the salt domes on the same region was being explored (Olien, 2012). In 1908, the Goose Creek oil field was found out in the same way as the Humble oil field discovery. In 1930s, oil productive fields located in the northwest of Harris, Tomball and Hockley, were discovered. While the exploration of new oil fields was being continued, Pratt & Johnson (1926) recognized a subsidence over Goose Creek area caused by oil extraction. The local subsidence over the Goose Creek revealed that this phenomenon could be seen over the other productive oilfields.

The Northwest Harris area has eight (8) productive oil fields, some of which began to produce in early 1900's. The oil and gas generated beds range between Upper Cretaceous and Miocene-aged rocks in Gulf Coast of Texas; the Wilcox, the Yegua, and the Frio Formations (Hackley & Ewing, 2010).

2.5.2 Geology and Stratigraphy of Study Area

The Northwest Houston area lies on Gulf Coast Plain (GCP). The formation of the GCP started with the breakup of the Pangaea in the Late Triassic (Salvador, 1991; Hackley, 2012). During the continental drift, the marine deposits were taking place in the Texas basin. In the Jurassic and Cretaceous, the limestone shelves that were formed during the Paleozoic were buried under the deltaic, fluvial, and shallow-marine environment deposits (Ward, 2006).

The Southeast coast of the Texas began to form with the deposition of the Wilcox Formation during the Paleocene (Dutton & Loucks, 2010). The stratigraphy of the Gulf Coast Plain is expressed in Figure 2.23.

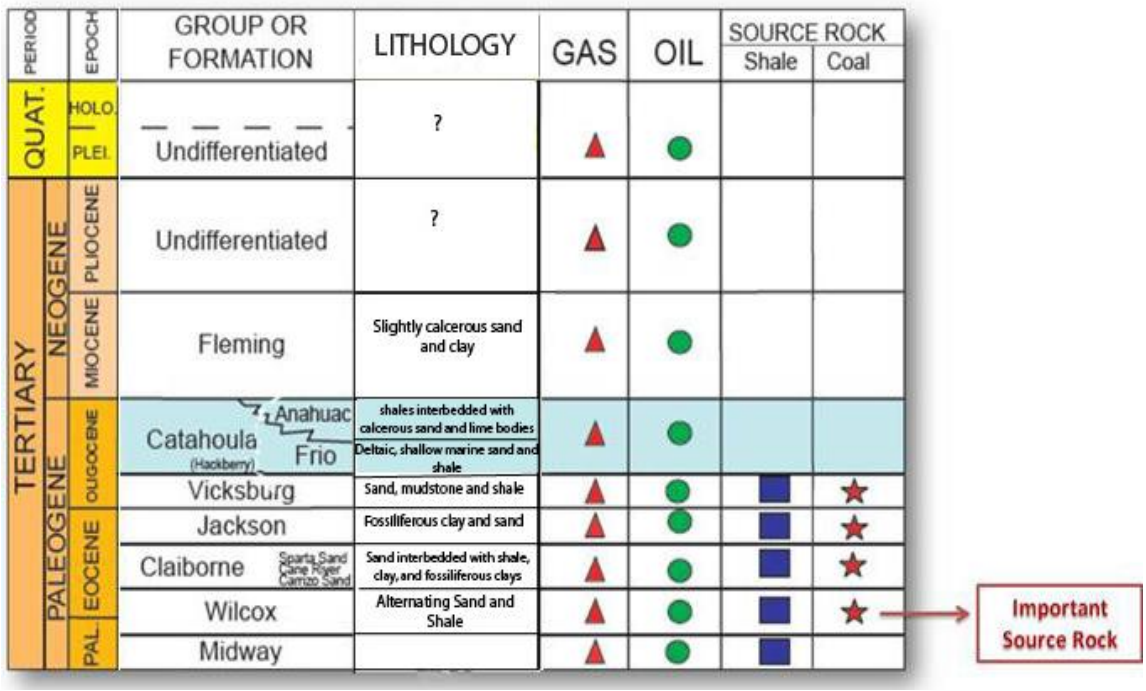

Figure 2.23: Generalized stratigraphic section of the northern Gulf of Mexico Coastal Plain showing potential hydrocarbon source rock intervals (modified from Hackley and Ewing, 2010).

2.5.3 Oil fields in Northwest Harris

The oil fields located in the Northwest Harris area are Cypress, Hockley, Tomball, Rotherwood, Fairbanks, Satsuma, Bammel, and Milton (Hamman, 1987; Canada, 1962; Cockerham, 1957; Harvey & Burkhead, 1939; Brace, 1962; Martyn & Beery, 1961).

Table 2.1: Oil Fields in Northwest Houston and the reservoir rocks producing oil and gas (Hamman, 1987; Canada, 1962; Cockerham, 1957; Harvey & Burkhead, 1939; Brace, 1962; Martyn & Beery, 1962).

Oil Field	Reservoir Rock Formation	Oil	Gas
Cypress	Yegua and Cockfield deposits	√	√
Hockley	Yegua and Cockfield deposits	√	
Tomball	Cockfield, Yegua and Wilcox,	√	√
Rotherwood	Upper Yegua Sand	√	
Fairbanks	Yegua Sand	√	√
Satsuma	Yegua Sand	√	
Bammel	Bammel sand, Yanko sand, D-Y sand, Fairbanks sand, and Lower Yegua sand	√	√
Milton	D-Y sand, Fairbanks sand, and Yegua sand	√	√

In this study, oil and gas production data for eight (8) oil fields that are located within the study area were acquired. The production data include the monthly extraction in terms of volume for four (4) different fluids: oil, casing head gas, gas well (GW-gas), and

condensate. All data are presented in tables (Table 2.2) for each oil field. The units of oil and gas were given as barrel (BBL) for oil and condensates, and mil (thousand) cubic feet (MCF) for gw gas and casing head. At first, these values were converted to cubic meters (m^3).

$$\mathbf{1}\ BBL = \mathbf{0.1589873}\ m^3$$

$$\mathbf{1}\ MCF = \mathbf{1000}\ ft^3 = \mathbf{28.3168}\ m^3$$

The total hydrocarbon production was calculated in m^3 and the annual production rate was computed in volume for the oil fields. A data sheet was generated in terms of oil fields and annual production rates (m^3/y). The annual production rate for each oil field was imported to ArcGIS 10 software to create surface modeling of hydrocarbon extraction volume change in the study area.

Table 2.2: Hydrocarbon production data (m^3) for oil fields in Northwest Harris County

Field Name	Oil (m3)	Casinghead (m3)	GW Gas (m3)	Condensate (m3)
CYPRESS (COCKFIELD A)	0	0	298068	0
CYPRESS (COCKFIELD B)	0	0	10812830.88	217.671
CYPRESS (Y-1)	0	0	39102301.92	1925.172
CYPRESS (Y-11)	1124.766	311.52	5114110.56	602.451
CYPRESS (Y-2)	629.322	731703.8	41087279.04	2435.721
CYPRESS (Y-3)	3573.366	1478559	8702226.24	409.584
CYPRESS (Y-4)	2477.061	1796139	2198283.36	252.81
CYPRESS (Y-6)	26279.202	8968604	11050294.08	1262.937
CYPRESS (Y-7)	590.367	0	13751795.52	427.551
CYPRESS (Y-9)	67388.652	6623765	0	0
CYPRESS (YEGUA 6340)	0	0	6854799.36	435.66
CYPRESS (YEGUA 6900)	0	0	3257621.28	308.301
CYPRESS (YEGUA BASAL)	0	0	2613737.76	84.906
CYPRESS, DEEP (12,500 WX. SD.)	0	0	5499489.12	607.062

Table 2.2: Continued

Field Name	Oil (m3)	Casinghead (m3)	GW Gas (m3)	Condensate (m3)
CYPRESS, DEEP (LOWER WILCOX)	0	0	17612406.24	235.797
CYPRESS, DEEP (UPPER WILCOX)	0	0	39627383.04	3418.182
CYPRESS, DEEP (WILCOX)	0	0	1274088905	60852.64
DECKERS PARIRIE, S. (SEG A 1300)	0	0	0	0
DECKERS PRAIRIE (BAYER 5400)	0	0	323244.48	8.904
DECKERS PRAIRIE (PITTS)	0	0	1507218.72	142.782
DECKERS PRAIRIE, S. (2150)	0	0	3463989.12	0.159
DECKERS PRAIRIE, S. (SEG A 1400)	0	0	0	0
DECKERS PRAIRIE, S. (SEG A 1700)	0	0	0	0
DECKERS PRAIRIE, S. (SEG A 1800)	0	0	1005558.24	0
DECKERS PRAIRIE, S. (SEG A)	0	0	0	0
DECKERS PRAIRIE, S. (SEG.A 1600)	0	0	0	0
DELHI, NORTH	41116.764	298492.8	0	0
DELHI, NORTH (6300)	0	0	31261541.76	1961.265
DELHI, NORTH (6700 KATY)	0	0	3716065.44	291.924
DURKEE (FAIRBANKS SAND)	161135.37	47622204	0	0
DURKEE (GOODYKOONTZ 7400)	0	0	0	0
FAIRBANKS (COCKFIELD 6500)	0	0	5304137.76	144.531
FAIRBANKS, N. (GOODYKOONTZ 1ST)	12264.147	6286389	0	0
HOOKS (SHALLOW)	0	0	11089517.28	0
HOUSTON, N. (GOODYKOONTZ - 2ND)	17626.581	2431215	0	0
HOUSTON, N. (GOODYKOONTZ 7200)	18064.308	1767706	0	0
HOUSTON, NORTH (FAIRBANKS 6800)	0	0	12953228.16	0.795
HUFFSMITH (5700)	0	0	81476.64	0
HUFFSMITH (PETRICH SAND)	0	0	0	0
HUFFSMITH (SID MOORE)	0	0	266292.96	111.141
HUFFSMITH, SW. (KOBS)	0	0	0	0
HUMBLE	318571.446	18013729	737877.6	0
HUMBLE LIGHT (RIVERSIDE)	998.52	124608	0	0
HUMBLE, SE. (EY-3)	0	0	0	0
KATY (COMBINED)	0	0	0	0
KATY (FIRST WILCOX)	0	0	18309559.68	473.661
KATY (II-A L)	0	0	0	0
KATY (WILCOX CONS.)	0	0	3694938.72	131.334
MILTON (YEGUA 6550)	0	0	0	0
MILTON (YEGUA COCKFIELD)	0	28.32	0	0
MILTON, E. (WILCOX 9800)	0	0	66216068.16	13082.84

Table 2.2: Continued

Field Name	Oil (m3)	Casinghead (m3)	GW Gas (m3)	Condensate (m3)
MILTON, N. (13000)	2069.067	2740781	1769521250	143572.2
MILTON, N. (9800 WILCOX)	0	0	1052243052	29497.52
MILTON, W. (10500)	0	0	10233403.68	577.17
SATSUMA	0	0	0	0
SATSUMA (6800)	3478.761	66665.28	0	0
SATSUMA (6850)	282.861	934.56	0	0
SATSUMA (6900 LOOK)	0	0	16142.4	0
SATSUMA (7100 SAND)	10929.183	490049.3	0	0
SATSUMA (7200)	3935.886	211323.8	0	0
SATSUMA (7500 MOORE, UPPER)	1202.199	504577.4	0	0
SATSUMA, N. E. (7100)	68.847	481.44	0	0
TOMBALL	19522.179	4994997	1429876.8	0
TOMBALL (950)	0	0	0	0
TOMBALL (COCKFIELD 5400)	0	0	12487449.12	0
TOMBALL (COCKFIELD MILO)	0	0	753340.32	0
TOMBALL (COCKFIELD UPPER 1-5300)	0	0	37652119.68	219.738
TOMBALL (COCKFIELD UPPER 5500)	0	0	31834002.24	142.782
TOMBALL (COCKFIELD UPPER 5500SW)	0	0	3159435.84	0
TOMBALL (COCKFIELD)	0	0	21983626.56	707.709
TOMBALL (COCKFIELD,UP 1-5300,SE)	0	0	20524863.36	365.064
TOMBALL (HIRSCH, NW.)	484.95	162443.5	0	0
TOMBALL (JACKSON 4400)	0	0	1087686.24	4.452
TOMBALL (JACKSON 4400,SE)	0	0	0	0
TOMBALL (KOBS)	18754.845	3335105	12733776.48	0
TOMBALL (LEWIS 5930)	67038.852	18763869	0	0
TOMBALL (LEWIS 5930, EAST)	0	0	2841458.88	10.812
TOMBALL (MARTENS, NW.)	13492.422	6465768	3016080	115.593
TOMBALL (MICHEL)	1431.636	343804.8	32132155.2	8219.028
TOMBALL (MIOCENE 1450)	0	0	3435810.72	2.226
TOMBALL (MIOCENE 1650)	0	0	0	0
TOMBALL (MIOCENE 1750)	0	0	7571748.48	0
TOMBALL (MIOCENE 1850)	0	0	5544517.92	0
TOMBALL (MIOCENE 2040)	0	0	2602154.88	0
TOMBALL (MIOCENE 2400)	0	0	14623909.92	51.198
TOMBALL (MIOCENE 2700 FB-A)	0	0	1215267.84	0
TOMBALL (MIOCENE 2700)	0	0	11299.68	0

Table 2.2: Continued

Field Name	Oil (m3)	Casinghead (m3)	GW Gas (m3)	Condensate (m3)
TOMBALL (MIOCENE 30)	0	0	4248	0
TOMBALL (MIOCENE 3150)	0	0	8941898.4	0
TOMBALL (MIOCENE 3320)	0	0	4841813.76	0
TOMBALL (MIOCENE 3400)	0	0	2374773.6	0
TOMBALL (MIOCENE 3500)	0	0	681067.68	0
TOMBALL (MIOCENE 7A,C)	0	0	508117.44	0
TOMBALL (MIOCENE 9)	0	0	874946.4	22.419
TOMBALL (PETRICH)	5335.404	2343565	0	0
TOMBALL (PETRICH, NW.)	0.318	56.64	0	0
TOMBALL (SCHULTZ CENTRAL)	18183.399	6285766	0	0
TOMBALL (SCHULTZ LO. N.E.)	28977.432	2440023	0	0
TOMBALL (SCHULTZ N.W.)	0	0	0	0
TOMBALL (SCHULTZ SE.)	273067.077	81133656	2089109.76	31.005
TOMBALL (SID MOORE)	0	0	92578.08	0
TOMBALL (STRAY 5300)	0	0	5804382.24	0
TOMBALL (STRAY 6700)	0	0	4594353.6	0
TOMBALL (THEIS, NE.)	0	0	0	0
TOMBALL (VICKSBURG 3940)	0	0	484272	0
TOMBALL (VICKSBURG 4050)	0	0	20142883.2	0
TOMBALL (WILCOX 8400)	0	0	72148994.88	1914.042
TOMBALL (WILCOX 8860, 2ND)	0	0	11056071.36	0.159
TOMBALL, SE. (10650)	0	0	15406023.36	1832.634
TOMBALL, SE. (11700)	0	0	165638582.4	15063.98
TOMBALL, SE. (12,250)	0	0	39417446.88	3705.018
TOMBALL, W. (ADAMS)	29533.455	4388127	0	0
TOMBALL, W. (TRESELER -A- SD)	6317.547	1123964	0	0
TOMBALL, W. (TRESELER)	19385.598	6338837	0	0
TOMBALL, WEST (HOCKLEY)	0	0	2333426.4	0

2.5.4 Hydrocarbon Extraction Modeling

The annual rate of total oil and gas extraction were plotted in ArcGIS 10. To realize the extraction volumes of each oil field, the surface models were generated using three different interpolation techniques. These three algorithm techniques under Spatial

Analysis tools are: i) Kriging, ii) Inverse Distance Weighted (IDW), and iii) Natural Neighbor.

CHAPTER 3: RESULTS

The results of GPS, LiDAR, InSAR, changes in groundwater levels, and the rate hydrocarbon extraction are given below.

3.1 GPS

GPS data from eighteen (18) PAM and two (2) CORS sites in the Northwest Harris County were processed and evaluated to elucidate the rate of vertical and horizontal movement of the land surface with reference to LKHU, ADKS, and NETP GPS stations (Table 3.1). The surface models generated from the rate of vertical displacement for two different time period, 2002-2011 and 2008-2011, are displayed in Figure 3.1 and Figure 3.2, respectively. The purpose of selecting two different periods is to assess the vertical displacement change with time. The first period is selected between year 2002 and 2011 to not to lose control points over the study area. Since, some of the GPS stations (after PAM 28) were installed after 2007. Both Figure 3.1 and Figure 3.2 illustrate that the subsidence rate of the Northwest Harris is the highest (39 mm/y) in the center of study area. Figure 3.3 demonstrates the horizontal motion of the GPS stations between 2002 and 2011. The arrows on the map present the magnitude of the velocity and the direction of relative movement of GPS stations with respect to reference stations. Most of the arrows point to the center part of the study area where subsidence rate is higher. Figure 3.4 shows the error values of GPS stations in Northwest Harris area.

Table 3.1: GPS Stations in the study area with the displacement rates in North, East, and vertical directions.

GPS Station	Station Type	Velocity vertical (mm/y)	Period	Velocity vertical (2008-2011) (mm/y)	Velocity in North (mm/y)	Velocity in East (mm/y)	Error (mm/y)
PAM 01	**PAM**	-24.8	2002-2011	-18.40	2.19	0.5	13
PAM 02	**PAM**	-31.87	2002-2011	-21.90	1.7	-0.57	18
PAM 03	**PAM**	-35.58	2002-2011	-13.10	1.9	-1.1	15
PAM 05	**PAM**	-24.12	2002-2011	-9.80	1.1	0	17
PAM 06	**PAM**	-28.72	2002-2011	-17.50	1.3	-1.2	17
PAM 07	**PAM**	-39.23	2002-2011	-22.90	2.5	0.98	19
PAM 08	**PAM**	-29.14	2002-2011	-18.60	3.2	-1.6	21
PAM 11	**PAM**	-6.48	2002-2011	-10.10	-1	2	10
PAM 13	**PAM**	-17.56	2002-2011	-19.50	0.21	0.87	22
PAM 17	**PAM**	-21.68	2002-2011	-17.40	0.15	-0.58	15
PAM 18	**PAM**	-24.96	2002-2011	-18.60	1.3	0.07	9
PAM 19	**PAM**	-13.76	2002-2011	-9.60	-0.2	0.8	13
PAM 29	**PAM**	-20.98	2007-2011	-20.90	1.8	-2.6	13
PAM 44	**PAM**	-21.14	2007-2011	-14.80	7	-1.3	12
PAM 45	**PAM**	-3.49	2007-2011	-4.80	2.3	-0.95	10
PAM 46	**PAM**	-25.12	2007-2011	-22.60	2.6	-0.7	10
PAM 47	**PAM**	-28.87	2007-2011	-26.80	2.5	-0.3	9
PAM 48	**PAM**	-15.39	2007-2011	-13.10	-1.8	1.56	11
PAM 56	**PAM**	-6.68	2007-2011	-4.80	2.5	1.06	9
coh7	**CORS**	-8.06	2002-2011	-1.90	2.4	-0.04	11
rod1	**CORS**	-21.16	2007-2011	-19.20	4.8	0.38	8

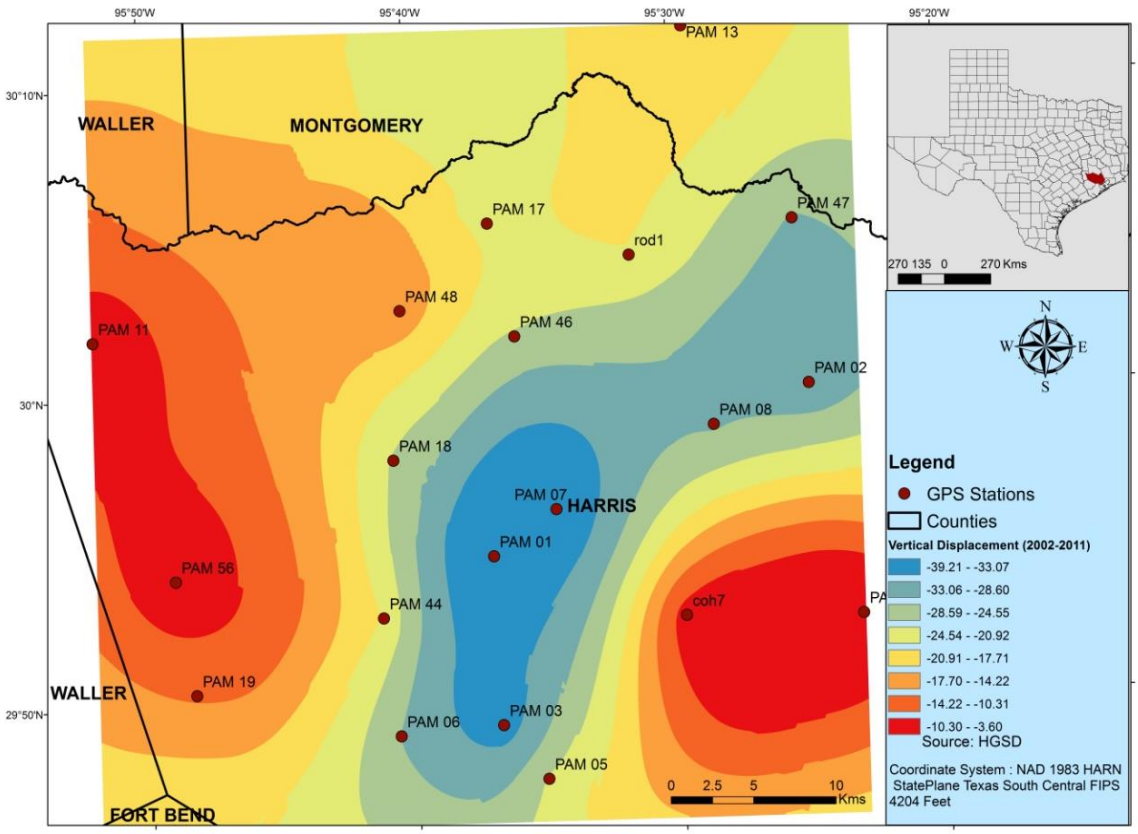

Figure 3.1: Kriging Interpolated surface of GPS results displaying surface deformation rates in Northwest Harris County between years 2002 and 2011.The red points on the surface map are GPS (CORS and PAM) stations over study area. As it is seen, the central region of the Northwest Harris is rapidly subsiding relative to northwest and southeast parts.

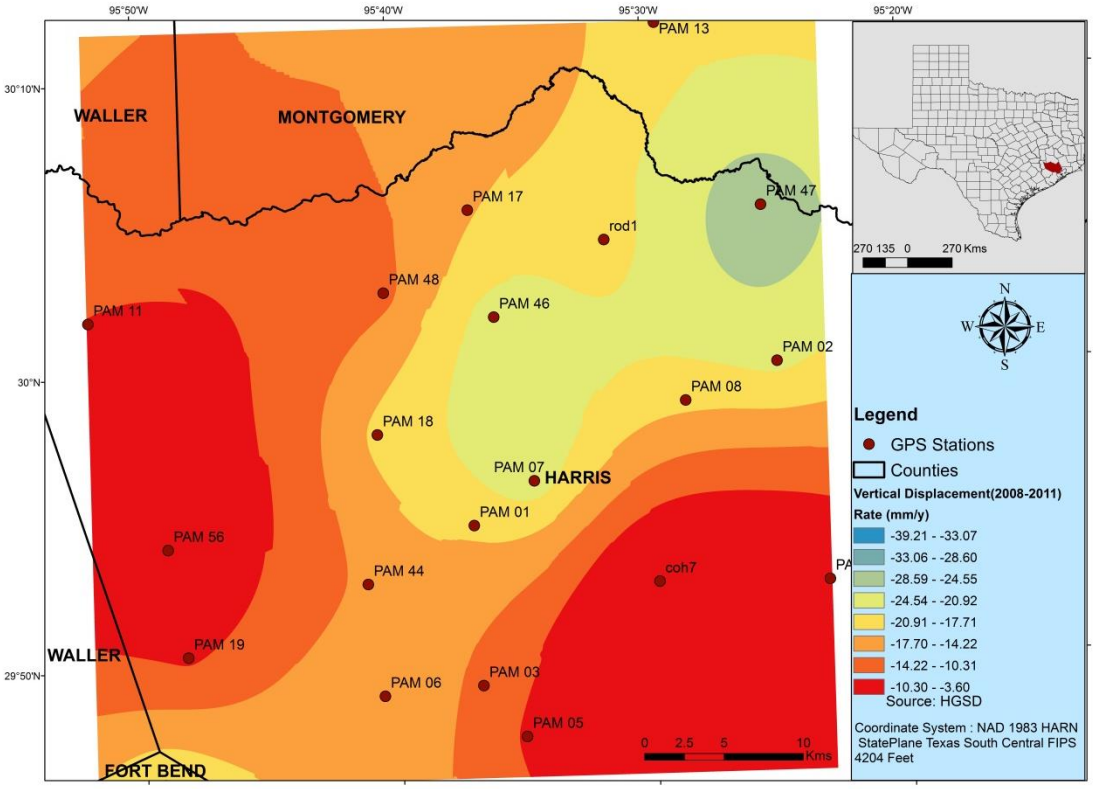

Figure 3.2: Kriging Interpolated surface of GPS results displaying surface deformation rates in Northwest Harris County between years 2008 and 2011. As in Figure 3.1, the central part of the study area is subsiding more. However, it is seen that the subsidence migrating towards northeast of the study area.

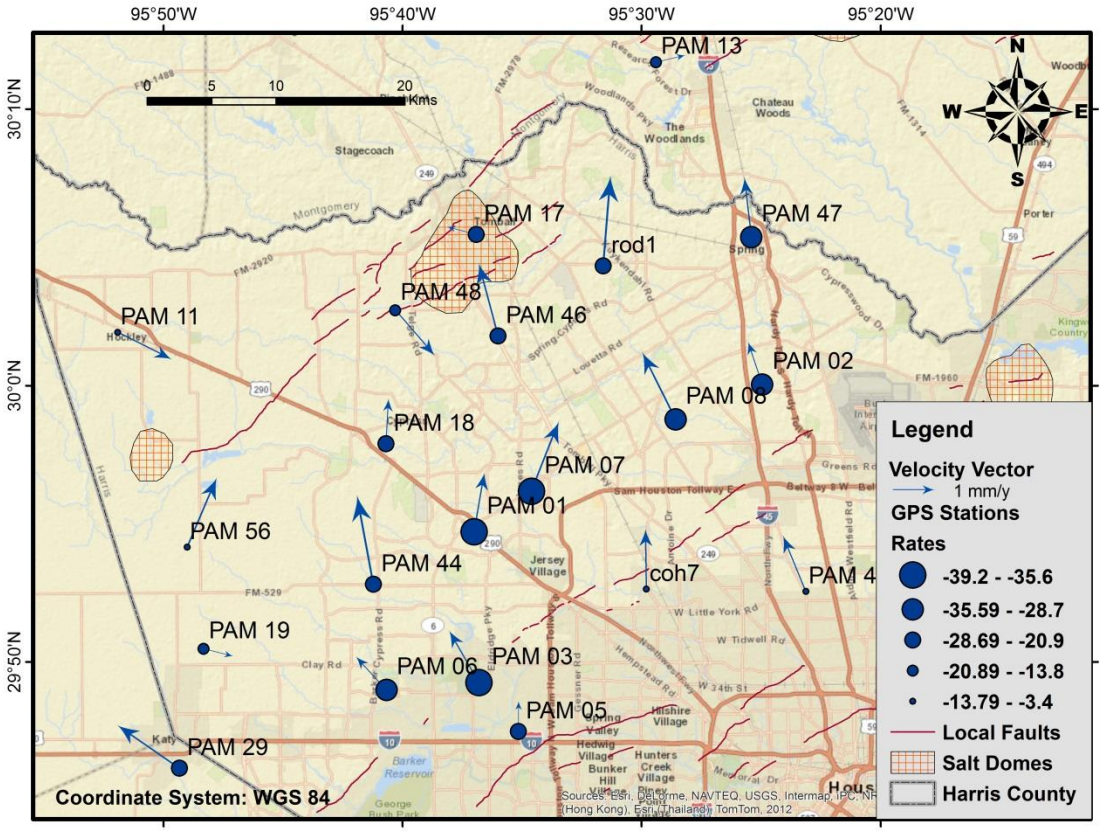

Figure 3.3: GPS displacement map in horizontal direction (north and east). The blue arrows are velocity vectors to show the direction and magnitude of the movement of each GPS Stations. These displacements are relative displacements to ADKS, LKHU, and NETP. Most of the vectors point the northern directions where the subsidence is high.

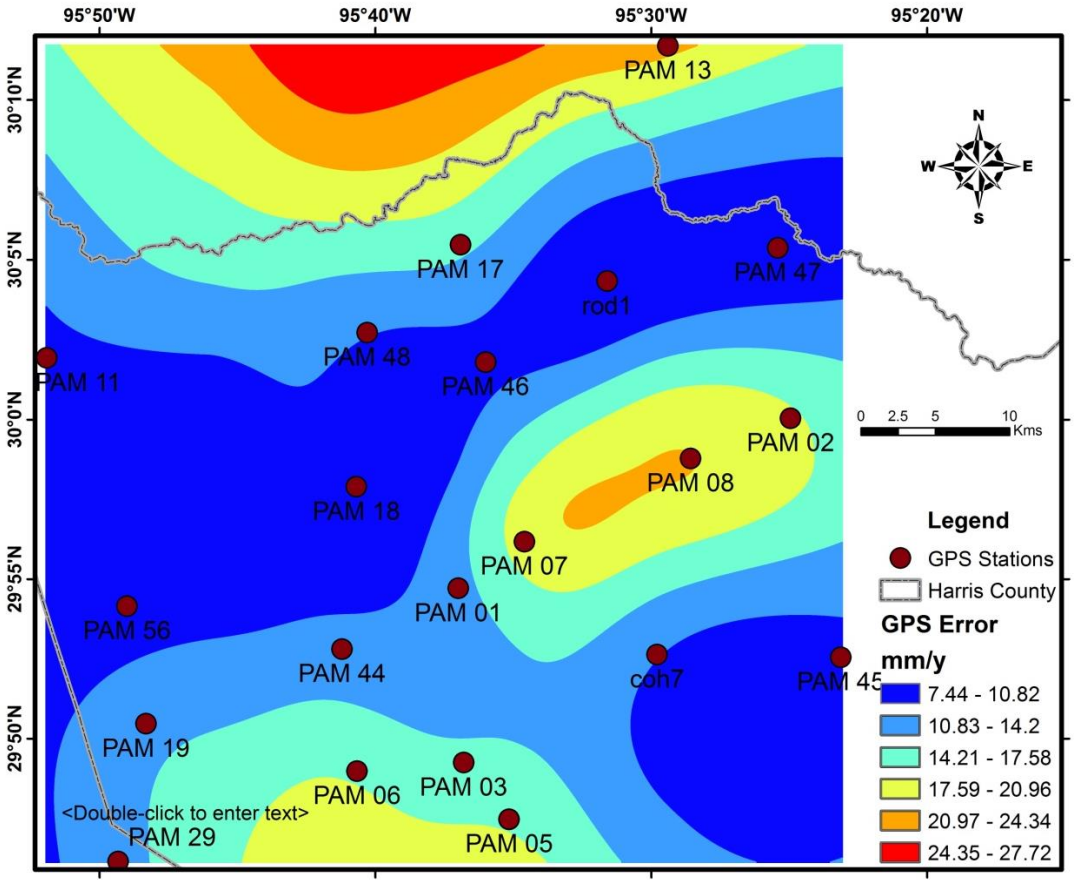

Figure 3.4: Error map of the GPS results. This map shows error values of the GPS stations in Northwest Harris area. Blue colors show low error values, and red colors indicate high error values. The red points on the map represent the location of the GPS stations in the study area.

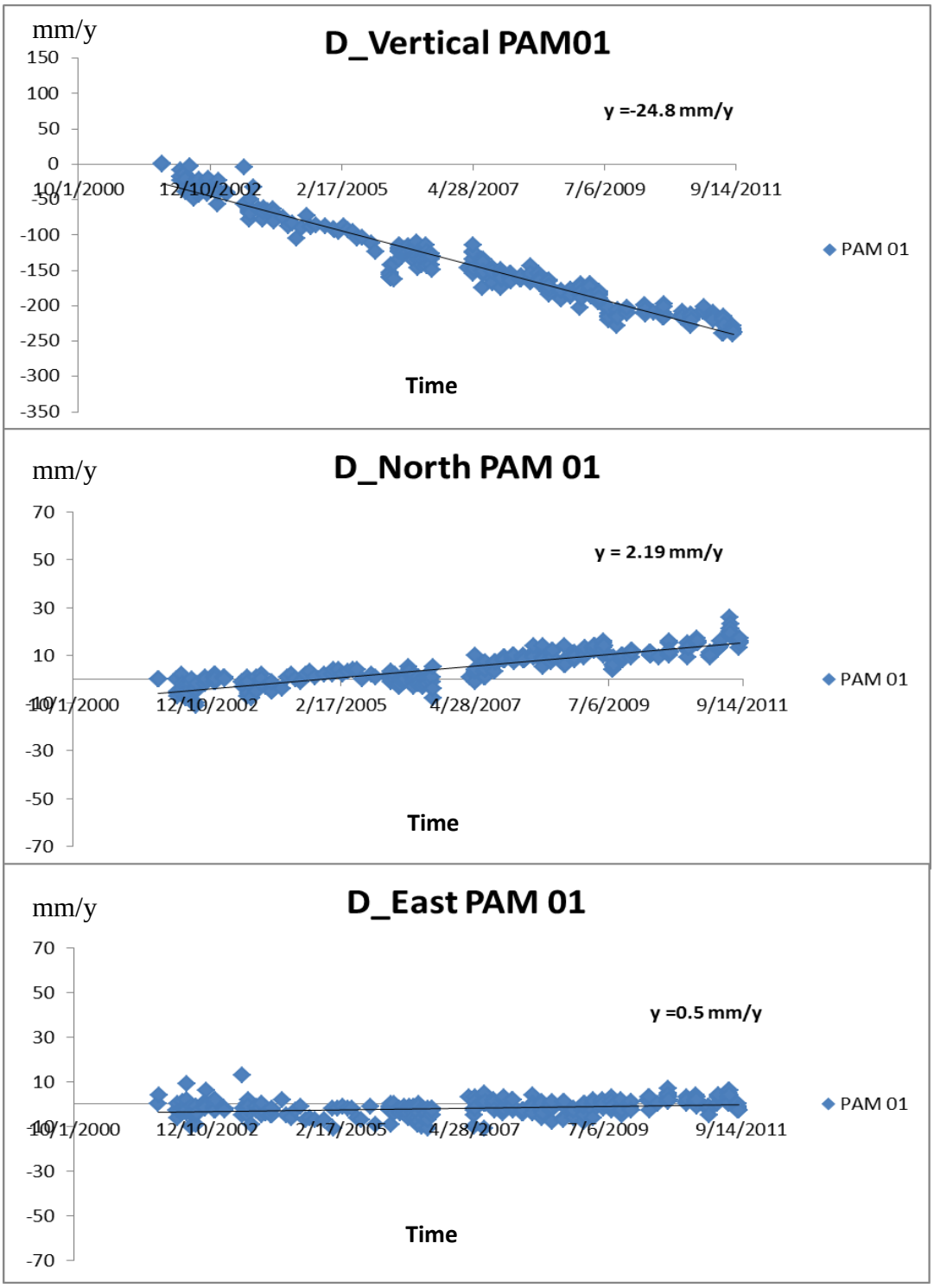

Figure 3.5: Graphs of the PAM 01 results in north, east, and vertical direction. Blue points are daily data for PAM 01, and the black line over these points presents the trend of changing in results. Error of the result for this station is ±13 mm/y.

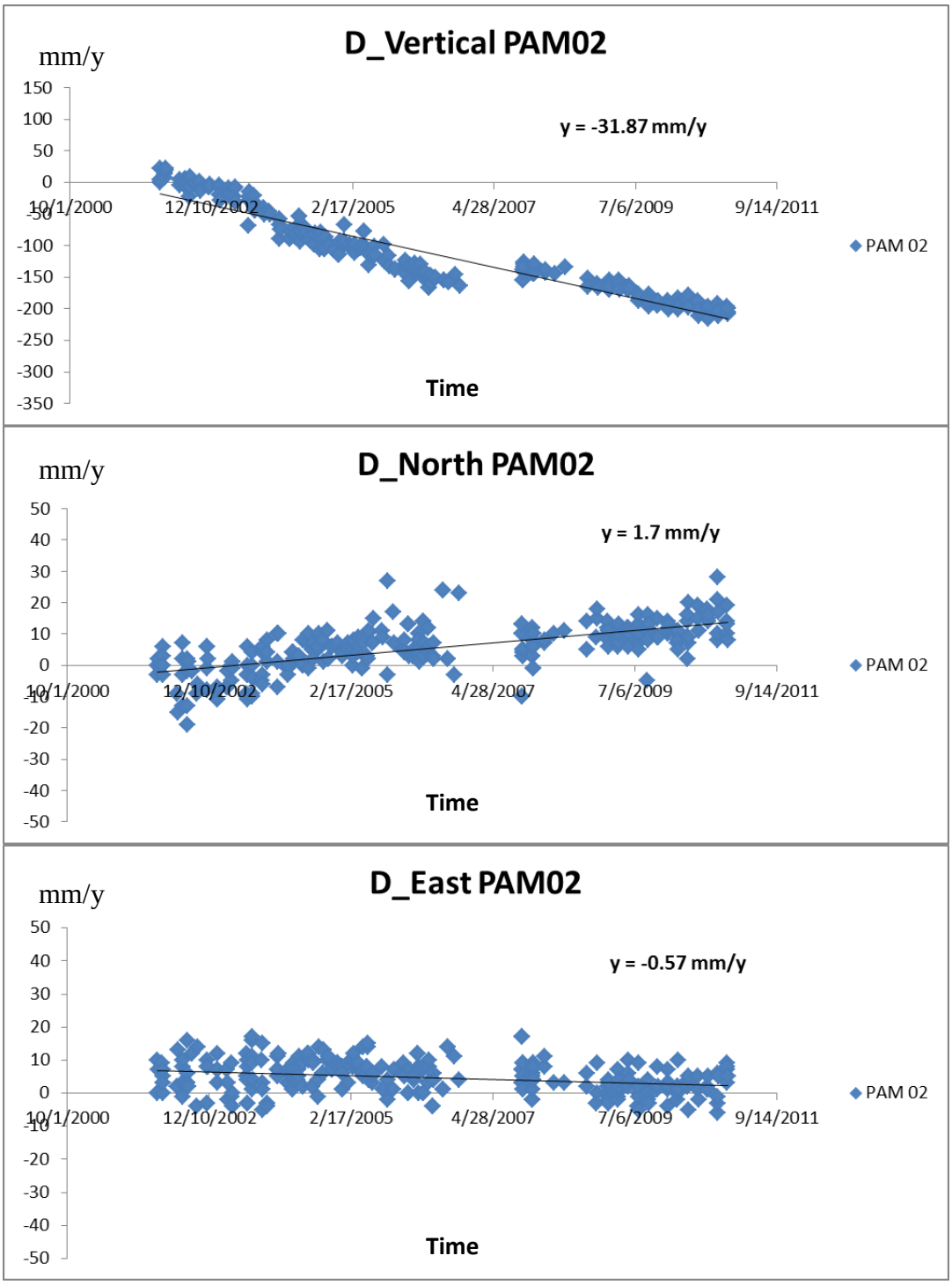

Figure 3.6: Graphs of the PAM 02 results in north, east, and vertical direction. Blue points are daily data for PAM 02, and the black line over these points presents the trend of changing in results. Error of the result for this station is ±18 mm/y.

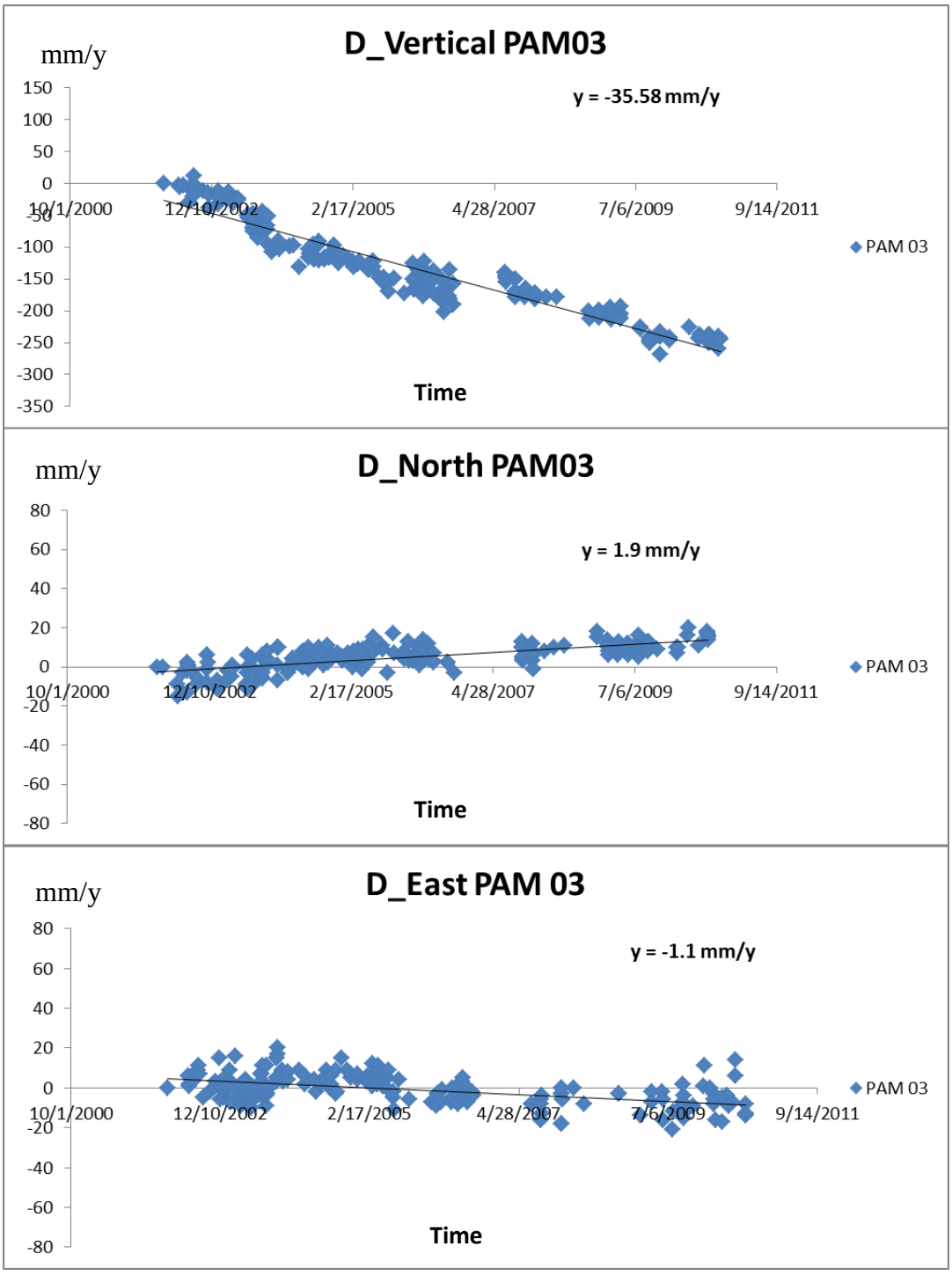

Figure 3.7: Graphs of the PAM 03 results in north, east, and vertical direction. Blue points are daily data for PAM 03, and the black line over these points presents the trend of changing in results. Error of the result for this station is ±15 mm/y.

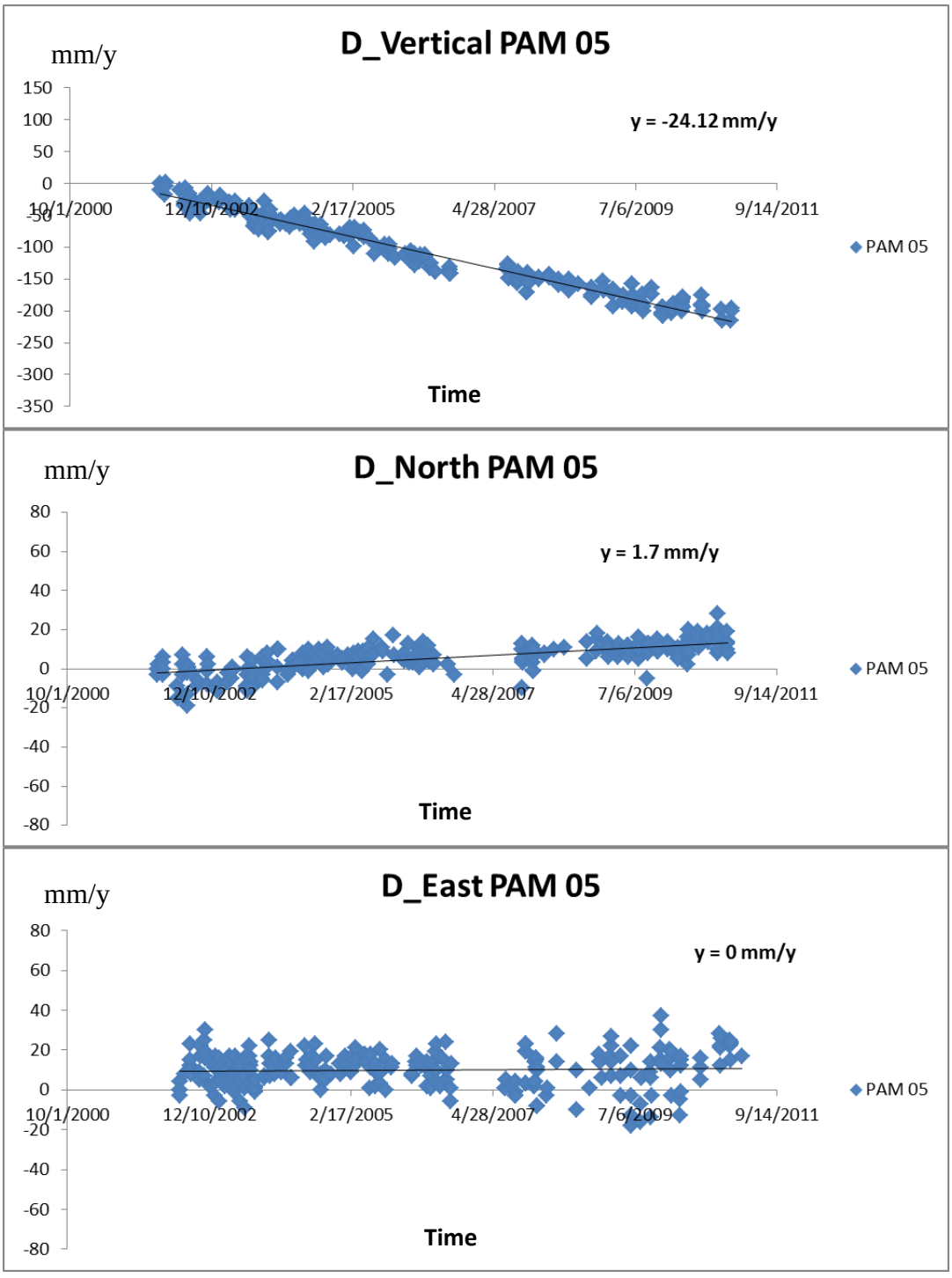

Figure 3.8: Graphs of the PAM 05 results in north, east, and vertical direction. Blue points are daily data for PAM 05, and the black line over these points presents the trend of changing in results. Error of the result for this station is ±17 mm/y.

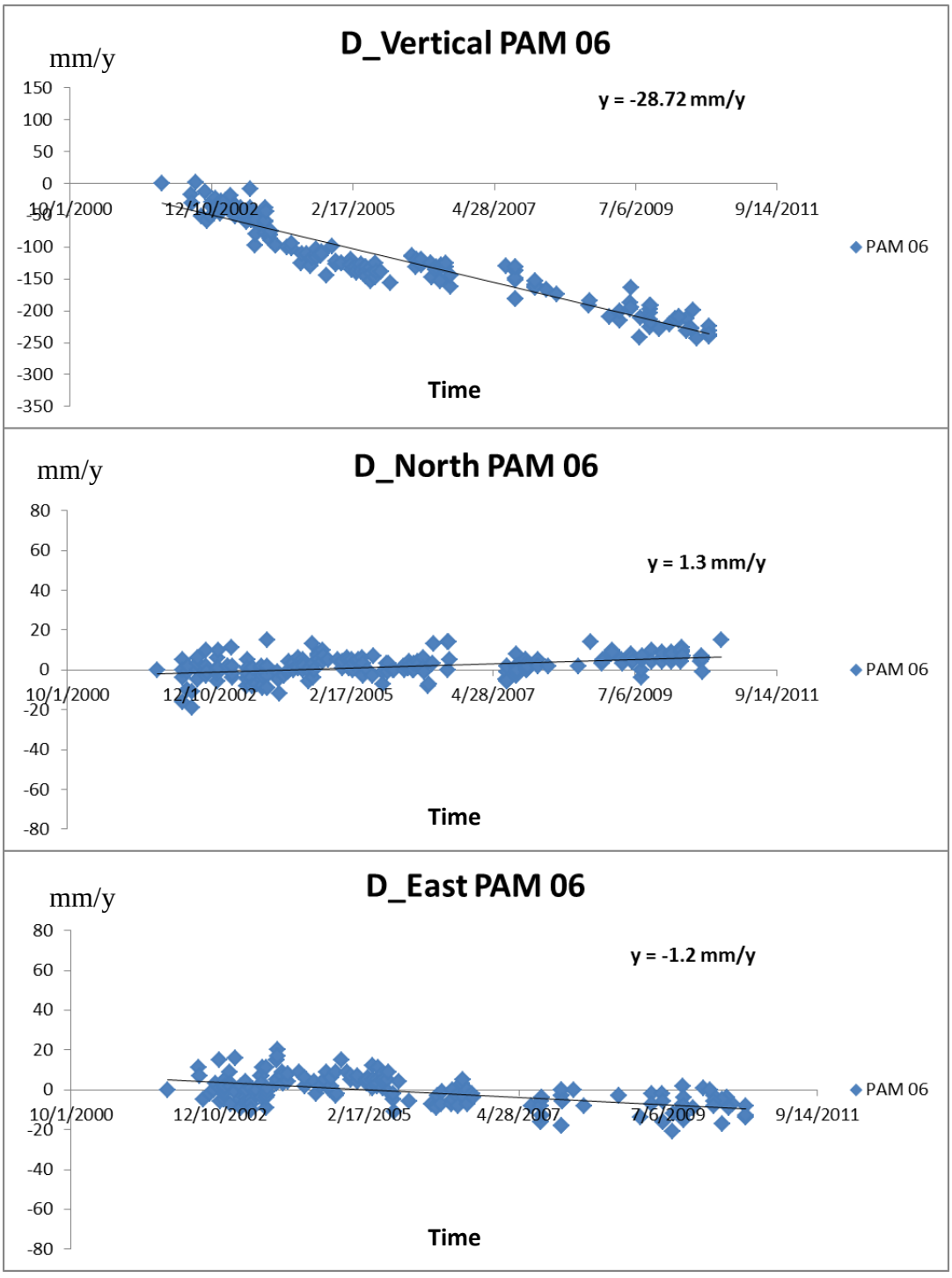

Figure 3.9: Graphs of the PAM 06 results in north, east, and vertical direction. Blue points are daily data for PAM 06, and the black line over these points presents the trend of changing in results. Error of the result for this station is ±17 mm/y.

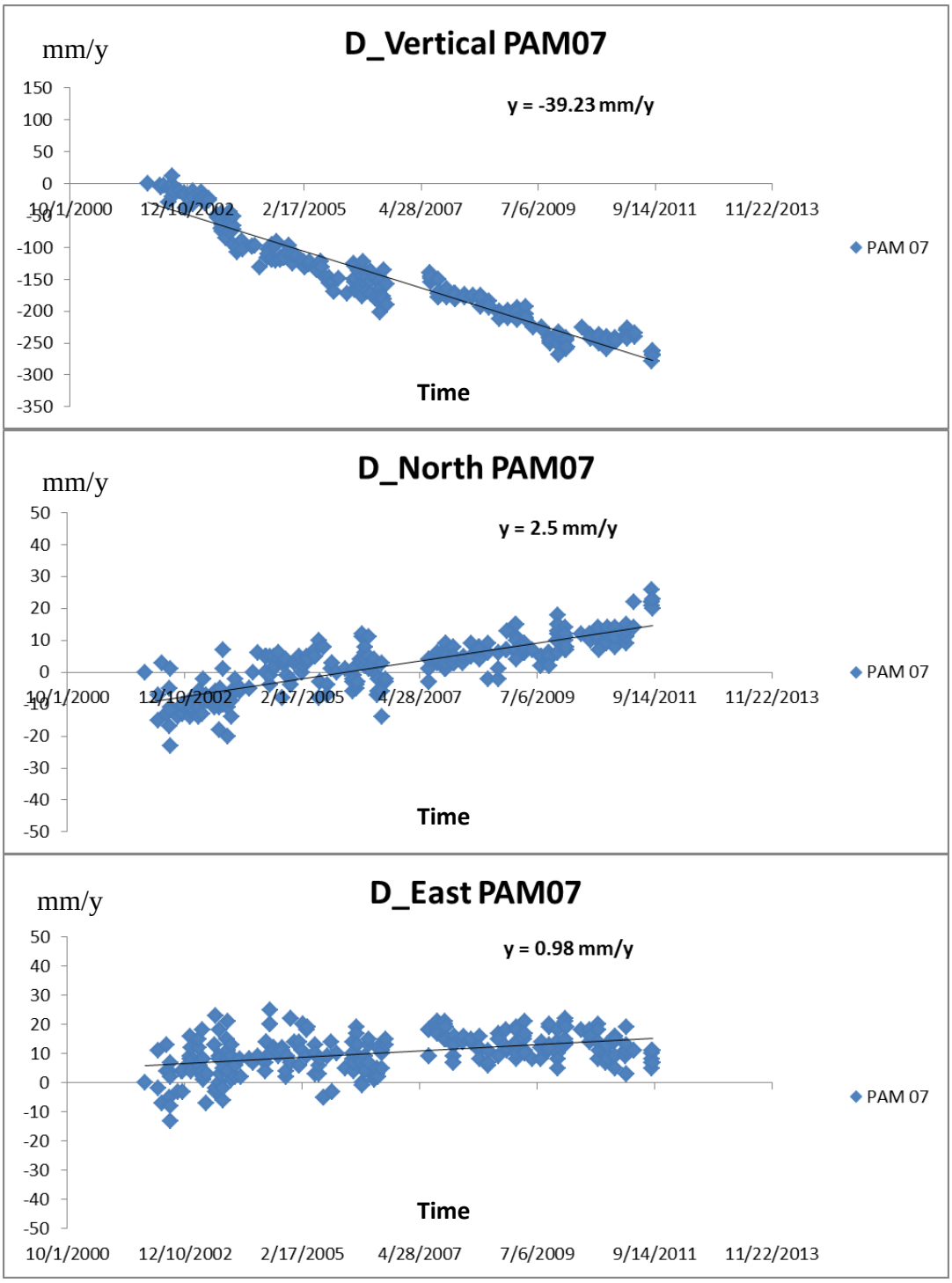

Figure 3.10: Graphs of the PAM 07 results in north, east, and vertical direction. Blue points are daily data for PAM 07, and the black line over these points presents the trend of changing in results. Error of the result for this station is ±19 mm/y.

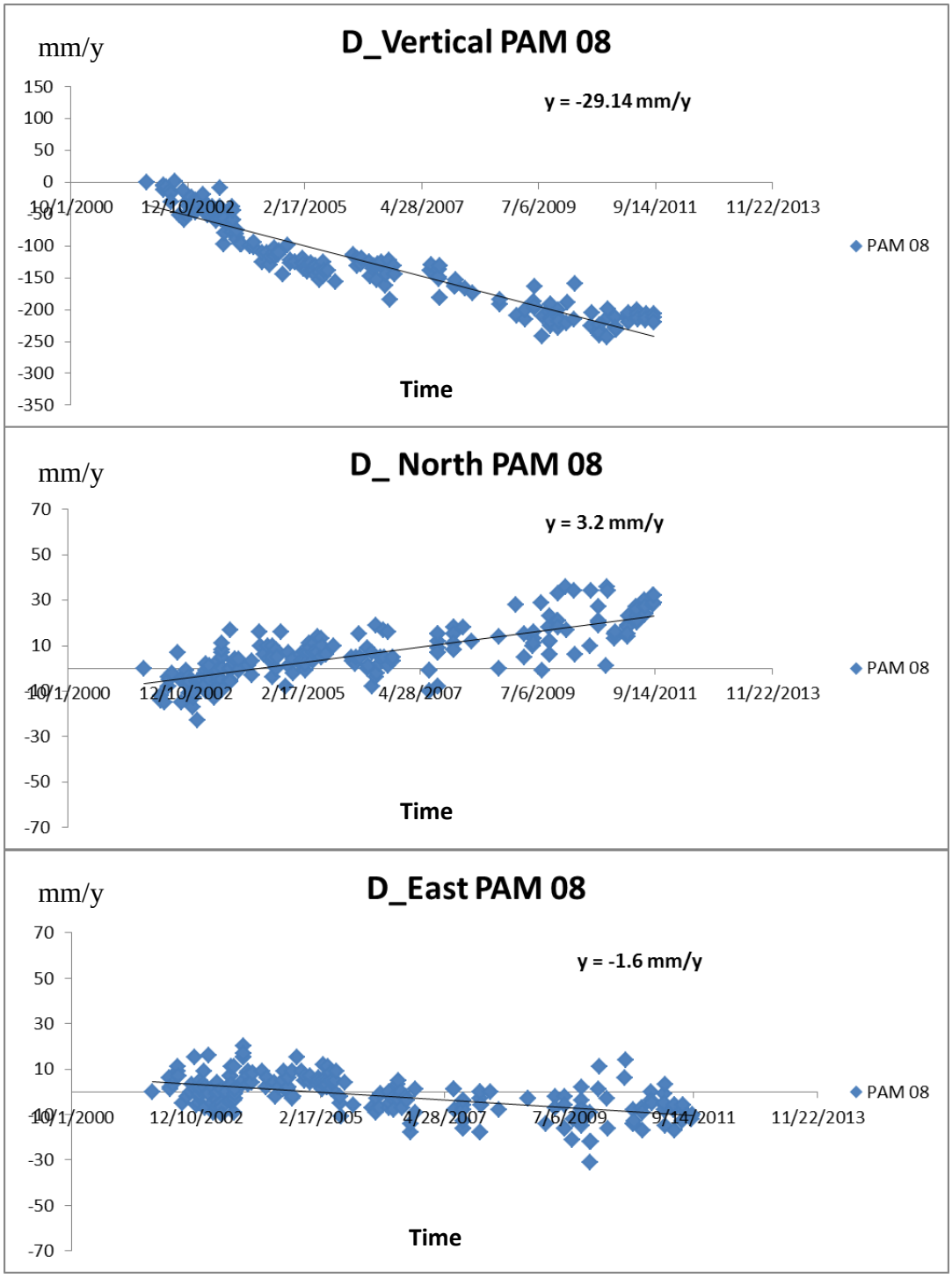

Figure 3.11: Graphs of the PAM 08 results in north, east, and vertical direction. Blue points are daily data for PAM 08, and the black line over these points presents the trend of changing in results. Error of the result for this station is ±21 mm/y.

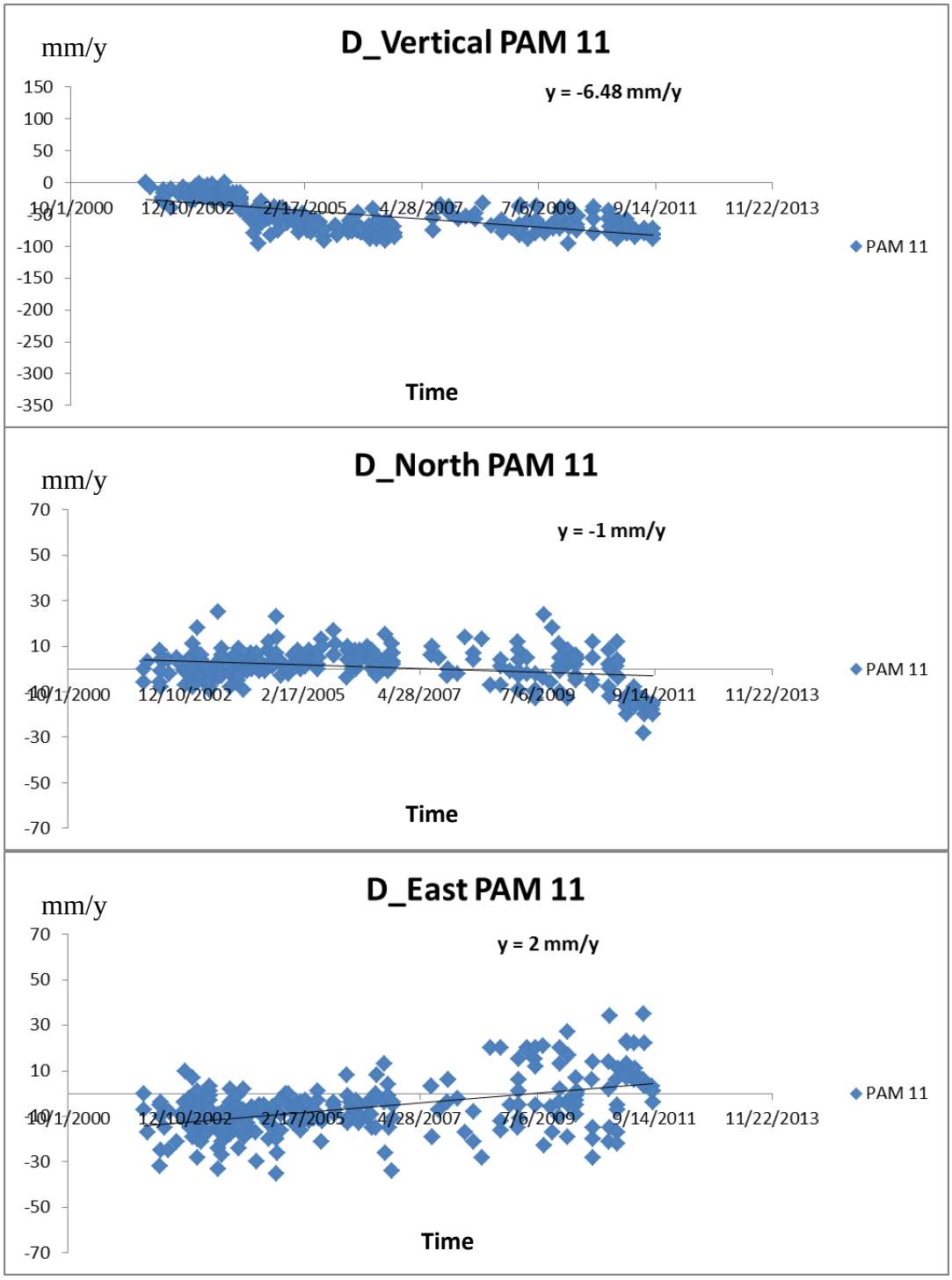

Figure 3.12: Graphs of the PAM 11 results in north, east, and vertical direction. Blue points are daily data for PAM 11, and the black line over these points presents the trend of changing in results. Error of the result for this station is ±10 mm/y.

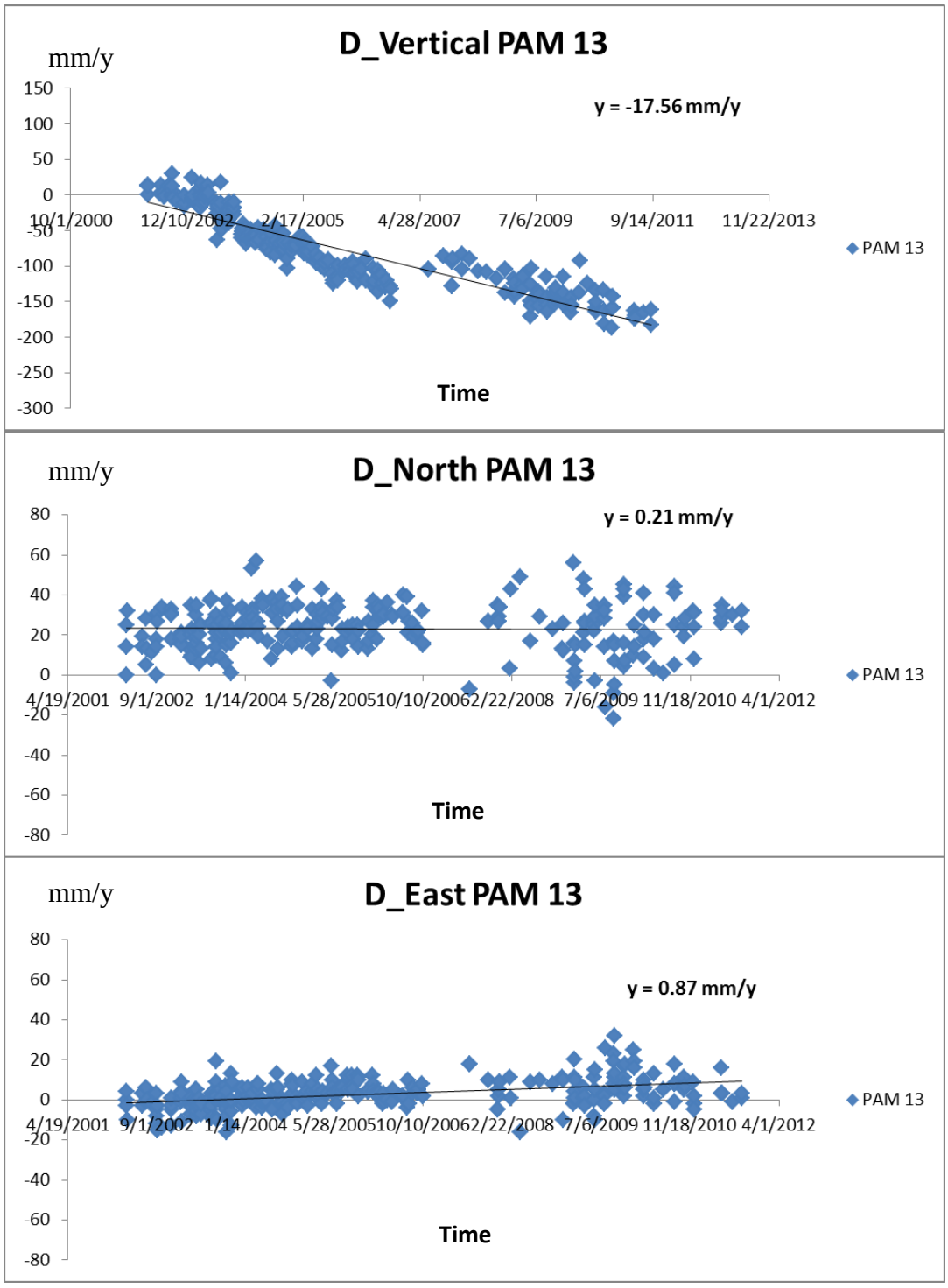

Figure 3.13: Graphs of the PAM 13 results in north, east, and vertical direction. Blue points are daily data for PAM 13, and the black line over these points presents the trend of changing in results. Error of the result for this station is ±22 mm/y.

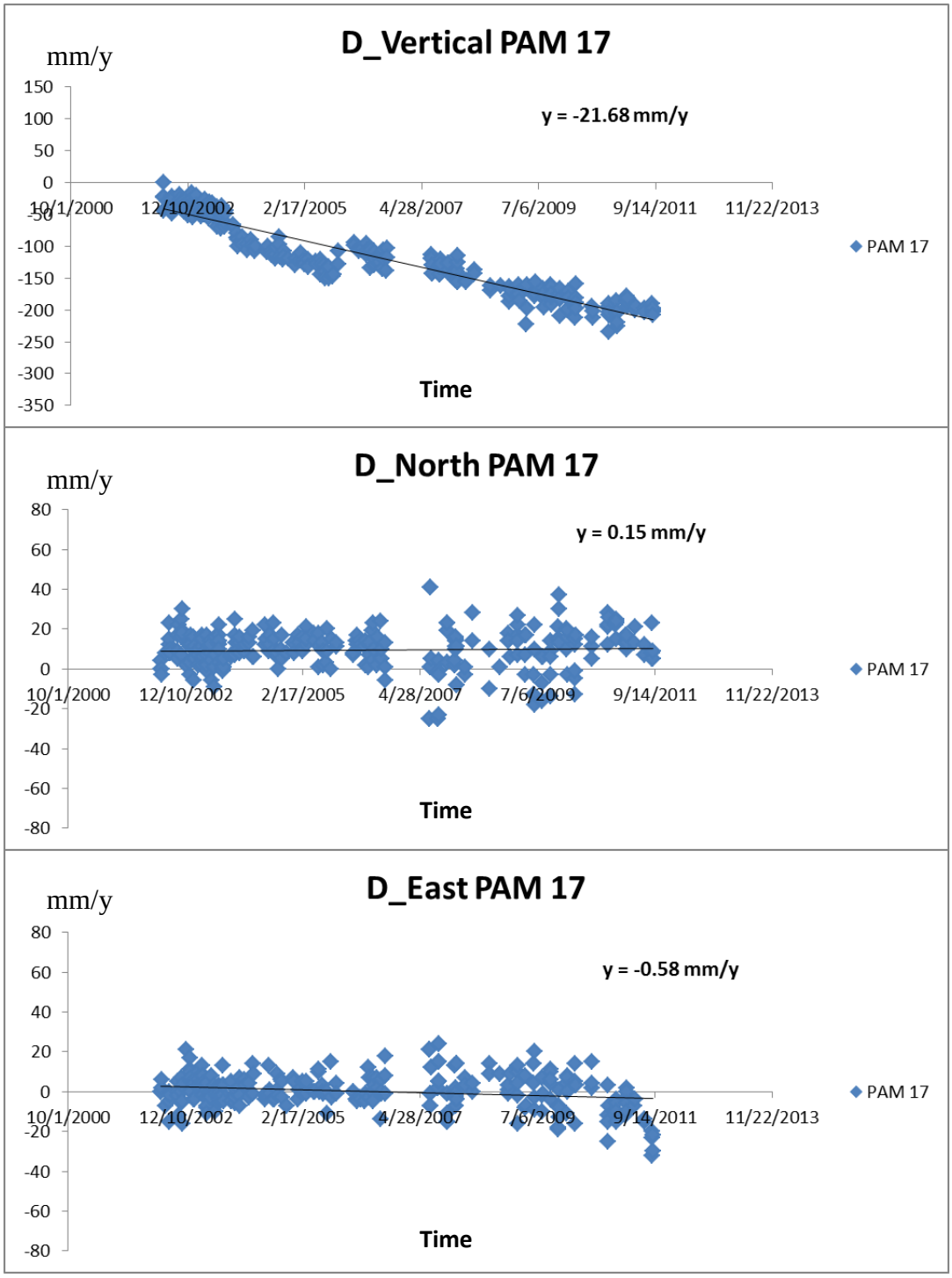

Figure 3.14: Graphs of the PAM 17 results in north, east, and vertical direction. Blue points are daily data for PAM 17, and the black line over these points presents the trend of changing in results. Error of the result for this station is ±15 mm/y.

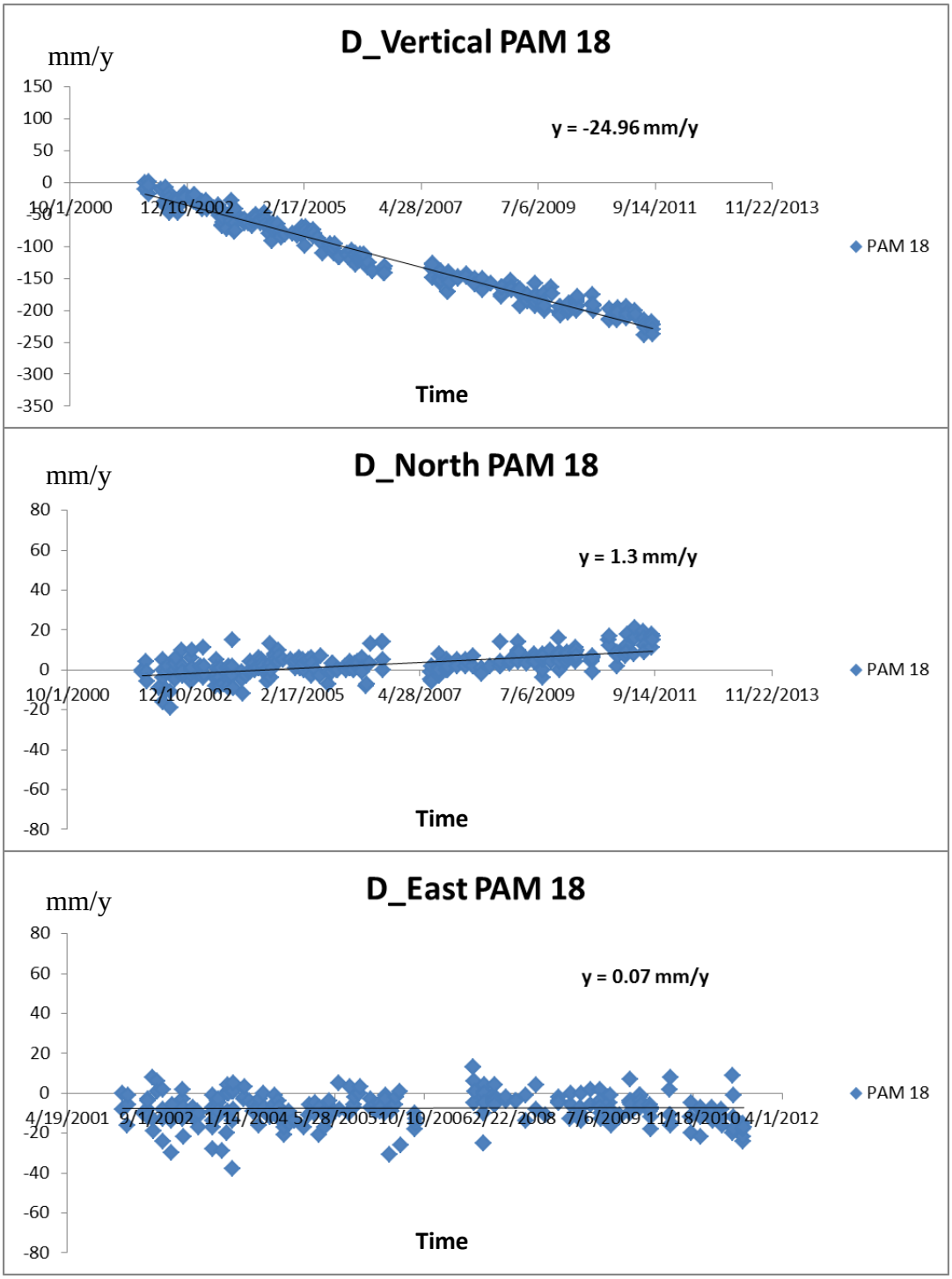

Figure 3.15: Graphs of the PAM 18 results in north, east, and vertical direction. Blue points are daily data for PAM 18, and the black line over these points presents the trend of changing in results. Error of the result for this station is ±9 mm/y.

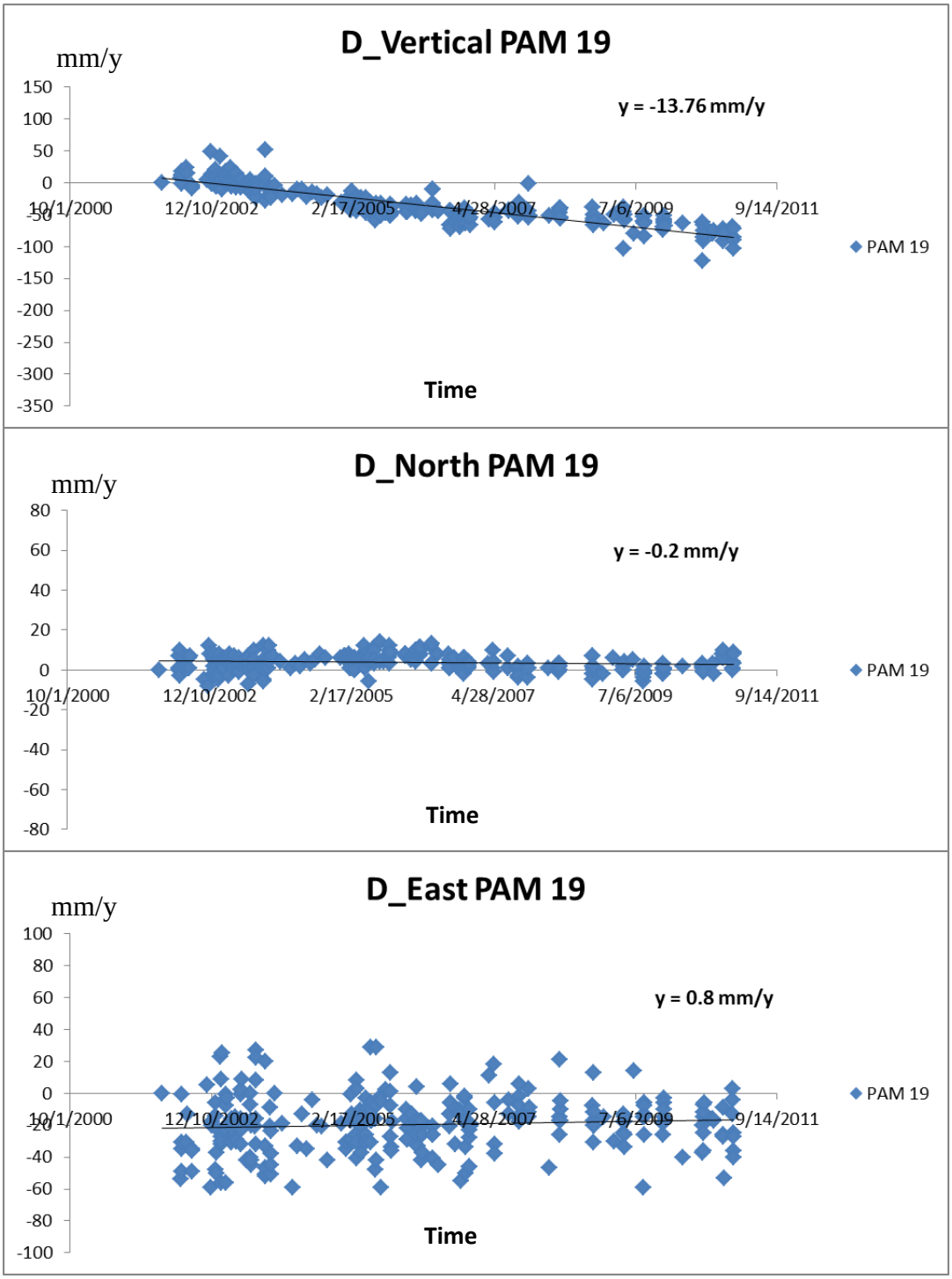

Figure 3.16: Graphs of the PAM 19 results in north, east, and vertical direction. Blue points are daily data for PAM 19, and the black line over these points presents the trend of changing in results. Error of the result for this station is ±13 mm/y.

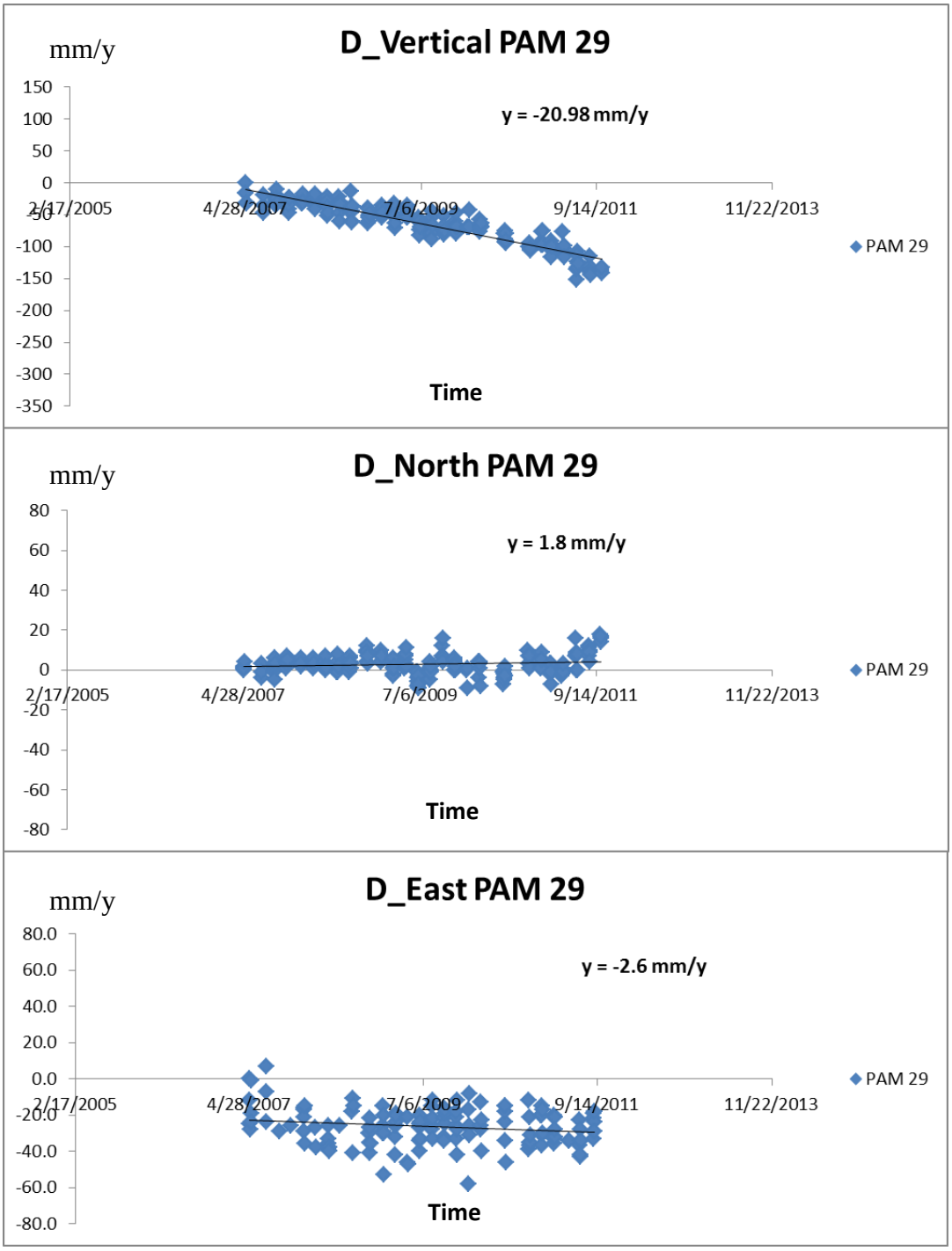

Figure 3.17: Graphs of the PAM 29 results in north, east, and vertical direction. Blue points are daily data for PAM 29, and the black line over these points presents the trend of changing in results. Error of the result for this station is ±13 mm/y.

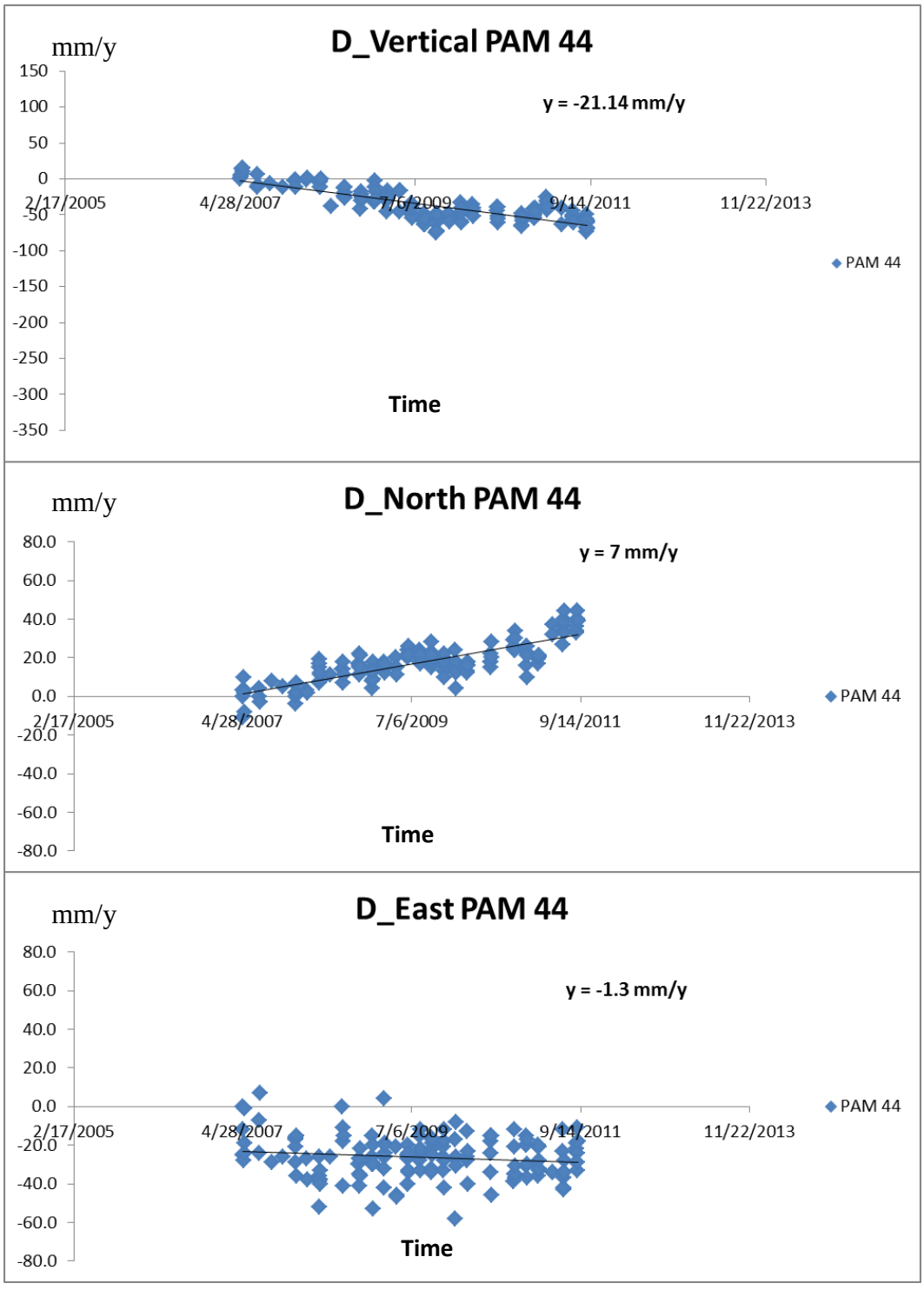

Figure 3.18: Graphs of the PAM 44 results in north, east, and vertical direction. Blue points are daily data for PAM 44, and the black line over these points presents the trend of changing in results. Error of the result for this station is ±12 mm/y.

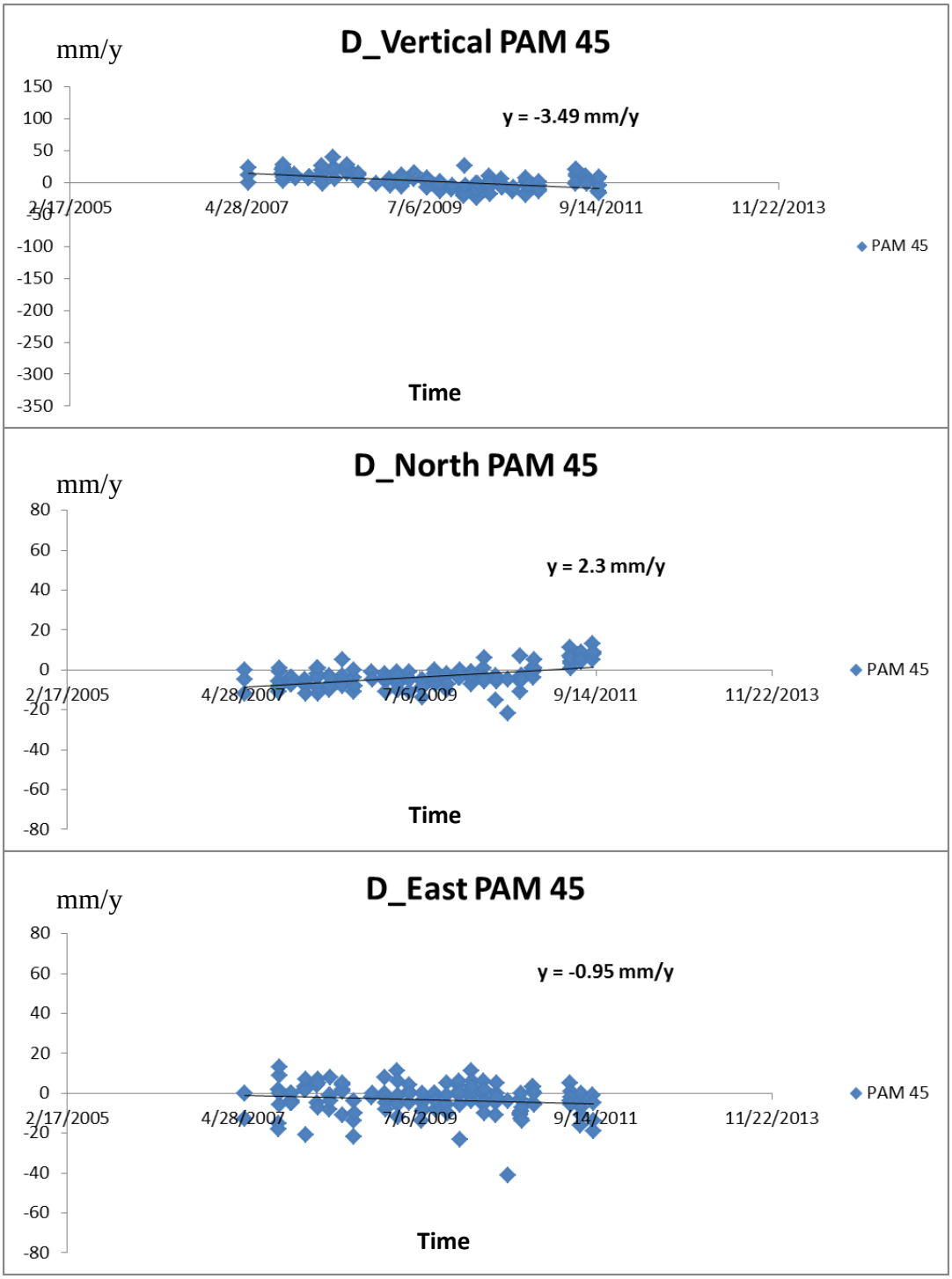

Figure 3.19: Graphs of the PAM 45 results in north, east, and vertical direction. Blue points are daily data for PAM 45, and the black line over these points presents the trend of changing in results. Error of the result for this station is ±10 mm/y.

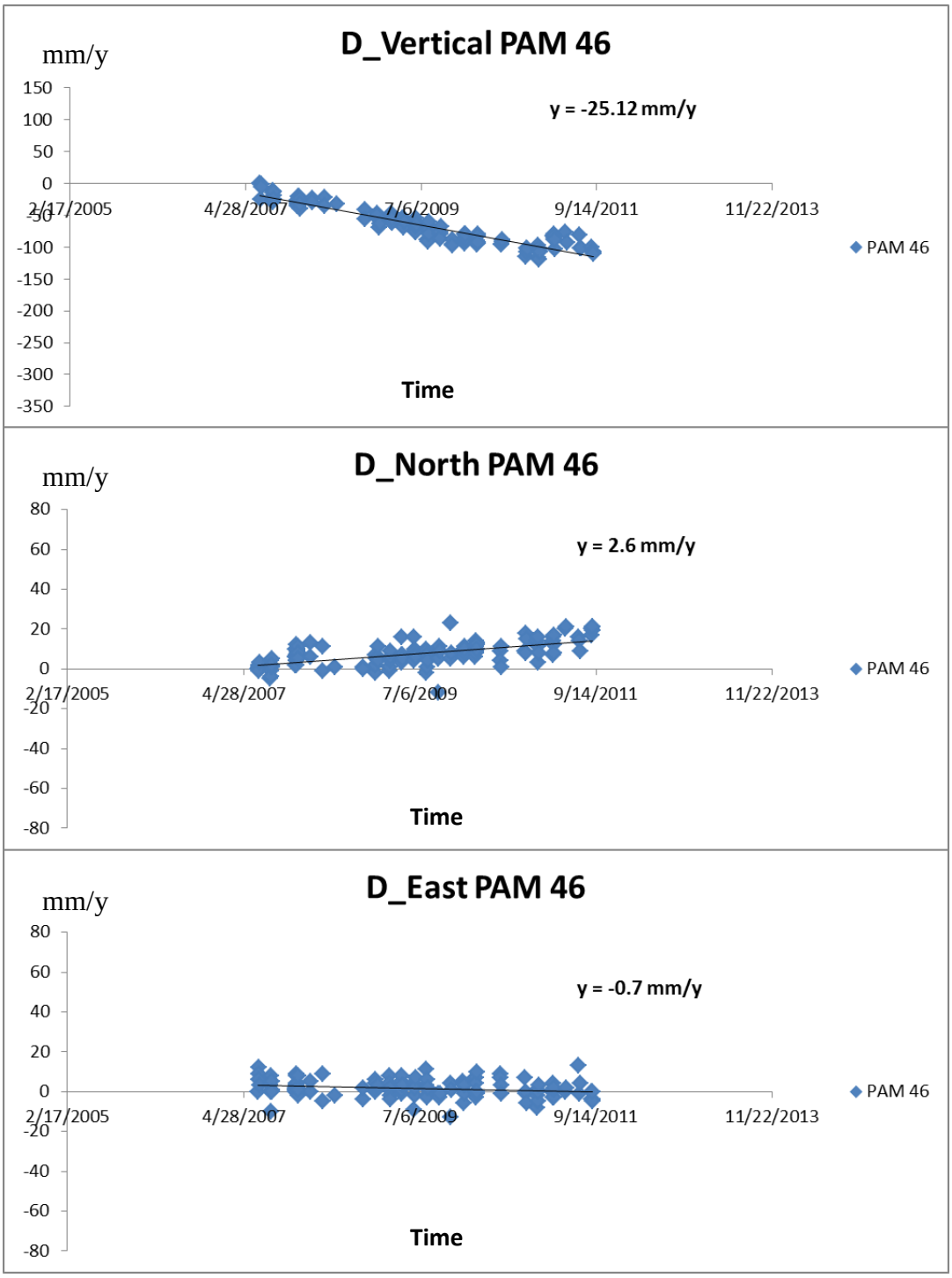

Figure 3.20: Graphs of the PAM 46 results in north, east, and vertical direction. Blue points are daily data for PAM 46, and the black line over these points presents the trend of changing in results. Error of the result for this station is ±10 mm/y.

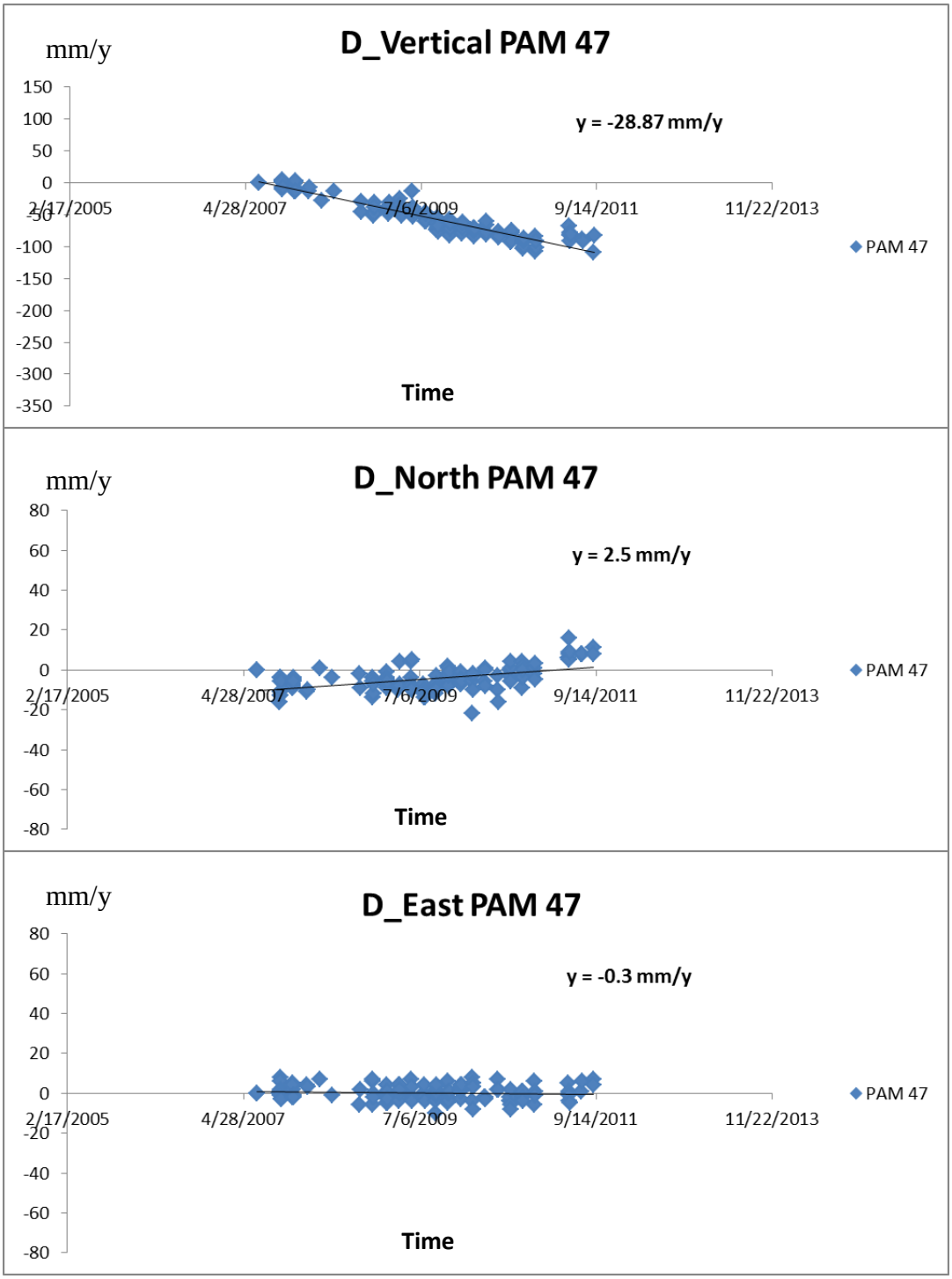

Figure 3.21: Graphs of the PAM 47 results in north, east, and vertical direction. Blue points are daily data for PAM 47, and the black line over these points presents the trend of changing in results. Error of the result for this station is ±9 mm/y.

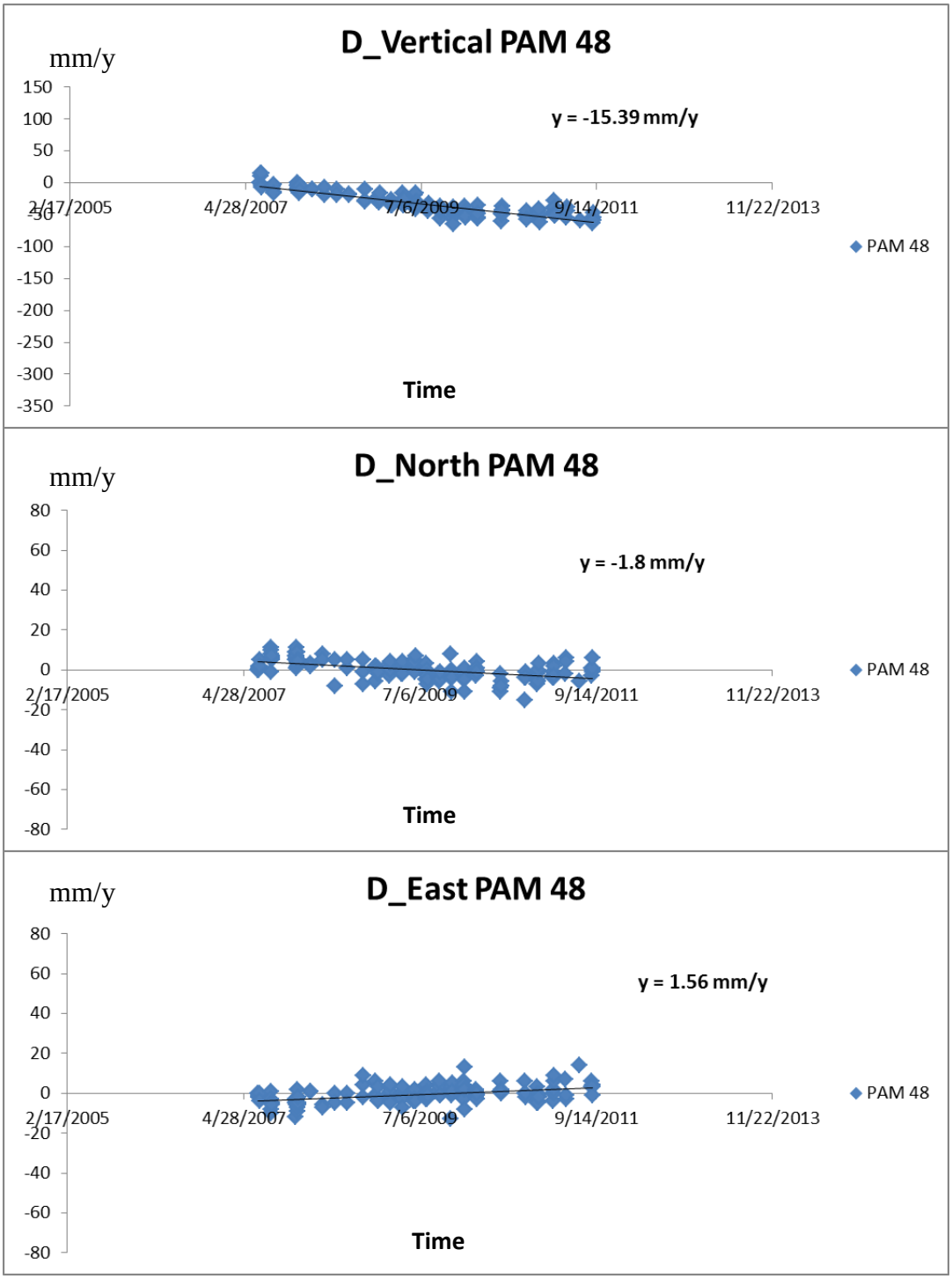

Figure 3.22: Graphs of the PAM 48 results in north, east, and vertical direction. Blue points are daily data for PAM 48, and the black line over these points presents the trend of changing in results. Error of the result for this station is ±11 mm/y.

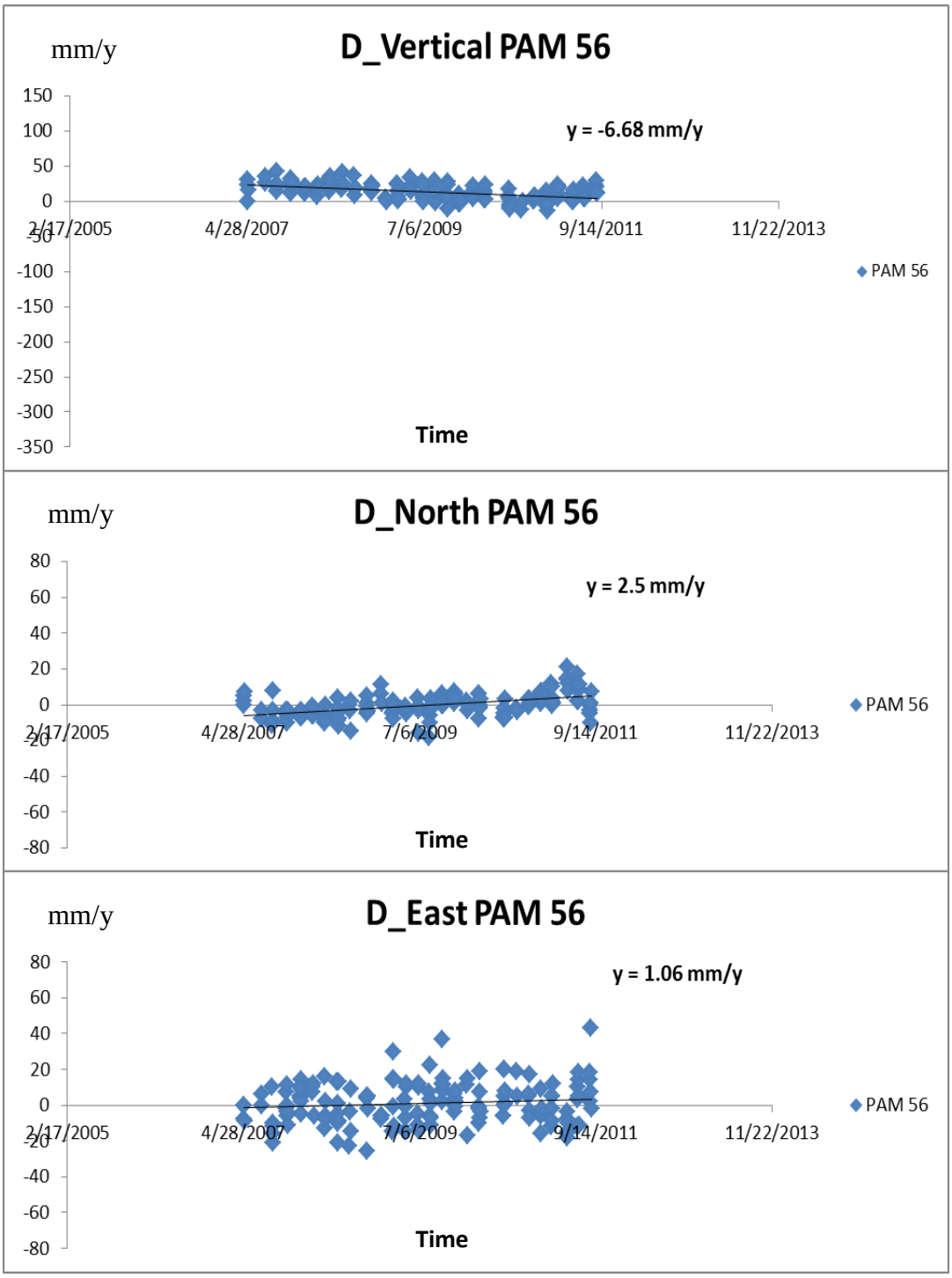

Figure 3.23: Graphs of the PAM 56 results in north, east, and vertical direction. Blue points are daily data for PAM 56, and the black line over these points presents the trend of changing in results. Error of the result for this station is ±9 mm/y.

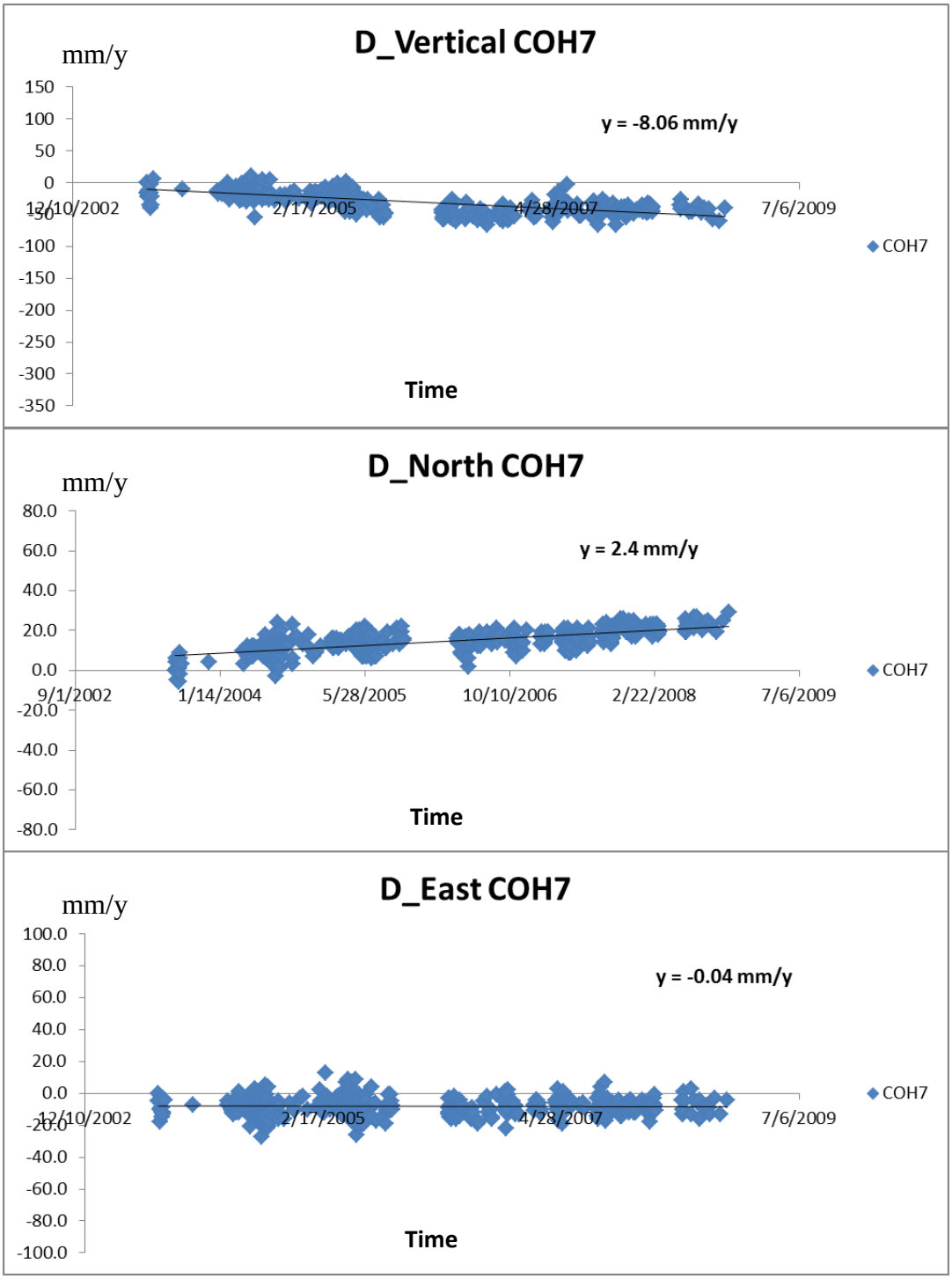

Figure 3.24: Graphs of the COH7 (CORS) results in north, east, and vertical direction. Blue points are daily data for COH7, and the black line over these points presents the trend of changing in results. Error of the result for this station is ±11 mm/y.

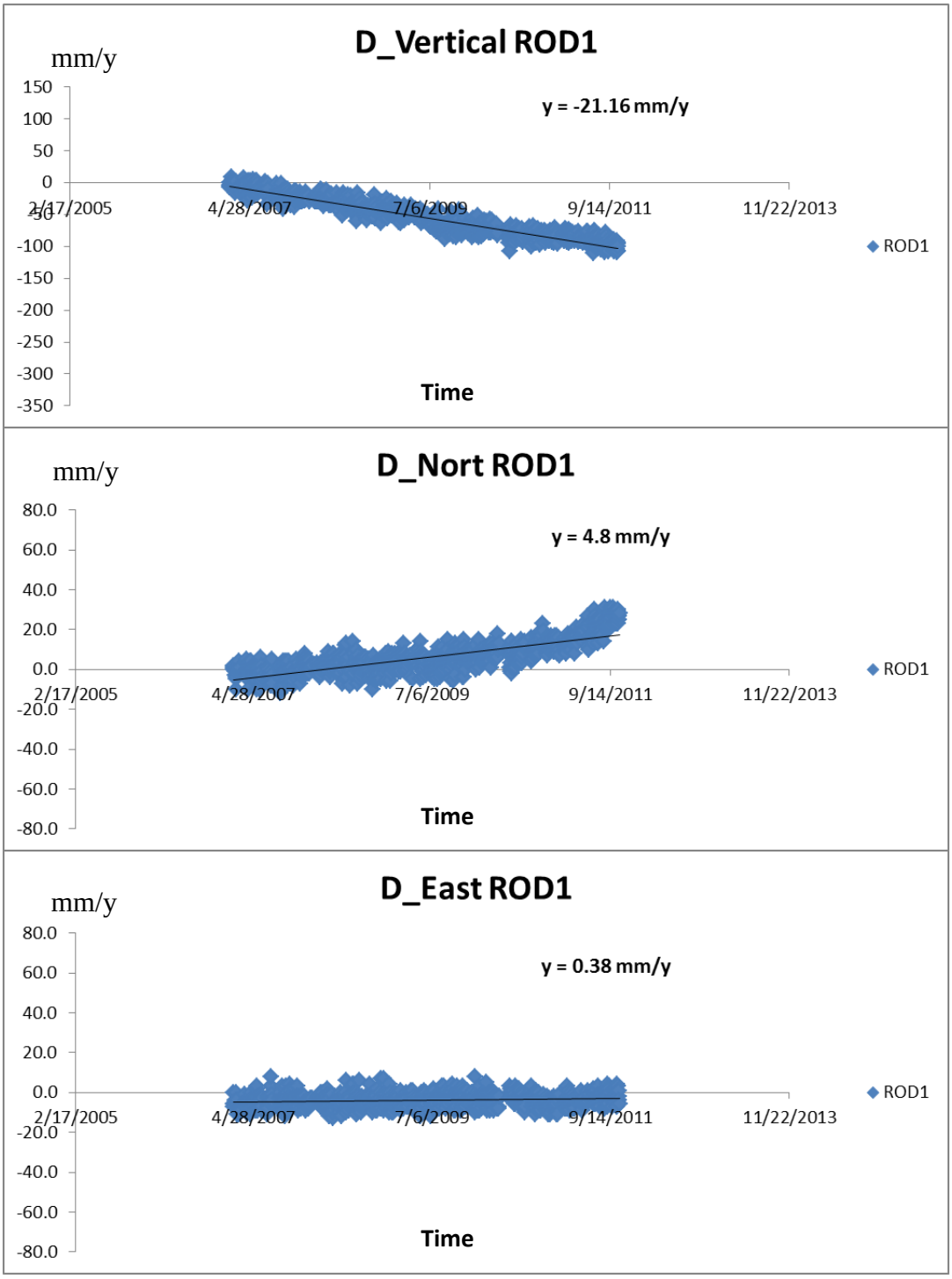

Figure 3.25: Graphs of the ROD1 (CORS) results in north, east, and vertical direction. Blue points are daily data for ROD1, and the black line over these points presents the trend of changing in results. Error of the result for this station is ±8 mm/y.

3.2 LiDAR

3.2.1 Zonal Statistics

Zonal statistics or 'polygonal based height computation' was used to calculate the height difference for three different parts of the Northwest Harris area: north, center, and south (Figure 3.26), and the Hockley Fault. Two different DEMs generated from 2001 and 2008 LiDAR data were used.

Figure 3.26 and Figure 3.28 present the statistics calculated for the Northwest Harris area and throw of the Hockley Fault. The colored polygons in Figure 3.26 represent the different section of the investigated area.

Table 3.2 and 3.3 show the results of zonal statistics of the Hockley Fault and Northwest Harris area for 2001 and 2008 LiDAR DEMs. The mean values of each table were plotted as bar graphs.

Figure 3.25 and Figure 3.27 show the difference of the mean values of the zones between 2001 and 2008 LiDAR DEMs at Hockley Fault and Northwest Harris area. The average value of these polygons gives the mean of rate of change on each region. The rate of change in the north, center and up section of study area, and the Hockley Fault are -4.5 cm/y, -2.1 cm/y, -3.5 cm/y, and -2.1 cm/y, respectively. The minus sign expresses the subsidence on the investigated area.

Table 3.2 Zonal Statistics of 2001 and 2008 LiDAR DEM of the Northwest Harris County

2001					
ID	MIN(m)	MAX(m)	RANGE(m)	MEAN(m)	STD(m)
CNT1	118.00	124.51	6.51	119.71	1.42
CNT2	127.00	130.00	3.00	128.52	0.80
CNT3	125.50	139.00	13.50	136.69	2.67
CNT4	150.00	158.00	8.00	155.17	2.36
CNT5	137.50	143.00	5.50	139.96	1.57
CNT6	143.00	148.00	5.00	146.12	1.56
CNT7	130.00	137.00	7.00	134.48	1.99
CNT8	105.50	108.50	3.00	107.12	0.78
CNT9	137.00	140.00	3.00	138.74	0.71
CNT10	153.00	157.00	4.00	155.26	1.11
CNT11	110.00	114.50	4.50	112.34	1.32
CNT12	137.50	147.00	9.50	142.57	2.49
CNT13	163.00	166.00	3.00	165.02	1.19
CNT14	110.50	116.00	5.50	113.44	1.43
CNT15	165.50	168.00	2.50	166.45	0.67
CNT16	134.00	138.50	4.50	135.91	0.99
CNT17	114.00	123.00	9.00	118.77	1.67
CNT18	142.00	144.00	2.00	143.28	0.76
CNT19	149.50	152.00	2.50	151.09	0.81
CNT20	153.00	158.00	5.00	155.44	1.25
STH1	78.01	81.00	2.99	79.43	0.72
STH2	77.01	82.51	5.49	79.11	1.23
STH3	85.49	89.00	3.51	86.73	0.91
STH4	69.51	72.49	2.99	70.98	0.70
STH5	83.02	89.49	6.47	87.36	1.38
STH6	96.00	99.50	3.50	98.21	0.75
STH7	100.00	107.00	7.00	104.37	1.89
STH8	95.00	102.00	7.00	98.48	1.68
STH9	65.51	69.00	3.49	67.64	0.72
STH10	77.00	92.00	15.00	88.40	2.89
NTH1	192.99	198.00	5.01	196.61	1.30
NTH2	199.98	213.00	13.02	206.84	4.03
NTH3	187.47	196.00	8.53	191.52	2.48
NTH4	175.00	180.99	5.99	177.86	1.50
NTH5	206.50	214.00	7.50	211.04	1.85
NTH6	252.00	264.00	12.00	257.56	3.13
NTH7	183.50	198.50	15.00	190.92	4.54
NTH8	181.50	207.50	26.00	193.54	8.27
NTH9	215.50	223.00	7.50	219.00	2.02
NTH10	189.00	192.50	3.50	190.79	0.95
NTH11	179.00	187.00	8.00	182.95	2.41

2008				
MIN (m)	MAX(m)	RANGE(m)	MEAN(m)	STD(m)
115.11	123.31	8.20	118.50	1.11
119.11	131.62	12.51	127.74	1.19
118.79	140.34	21.56	136.36	1.78
146.04	159.83	13.80	155.18	2.40
135.49	151.16	15.68	139.67	1.51
141.39	155.56	14.17	145.73	1.68
127.15	137.22	10.07	133.59	1.75
102.25	110.71	8.46	106.31	0.84
132.18	140.75	8.57	138.05	0.93
151.50	158.90	7.40	155.30	1.27
107.41	116.20	8.78	112.19	1.36
133.72	148.60	14.87	142.06	2.40
161.77	168.53	6.76	165.29	1.21
107.30	121.98	14.68	112.47	1.63
164.08	168.87	4.78	165.92	0.63
131.02	139.00	7.98	135.54	0.99
106.28	126.09	19.80	118.31	1.61
139.67	149.50	9.84	142.89	0.89
147.75	153.58	5.83	150.12	0.85
150.34	162.17	11.83	154.72	1.14
69.03	91.56	22.53	79.51	1.42
72.20	89.40	17.20	78.47	1.39
76.73	89.53	12.80	85.87	1.48
63.82	74.40	10.58	70.52	0.86
77.76	92.23	14.46	87.14	1.28
92.64	104.92	12.27	97.59	0.93
96.89	109.46	12.57	103.36	2.05
83.15	103.73	20.58	97.98	1.72
61.54	70.89	9.34	67.34	0.70
79.98	93.16	13.19	87.88	2.41
189.08	200.43	11.36	196.45	1.69
199.31	216.36	17.06	206.49	4.08
186.06	197.60	11.54	191.46	2.44
173.31	182.83	9.52	177.90	1.53
205.32	216.00	10.67	210.82	1.71
249.76	264.98	15.22	257.88	2.89
180.97	200.61	19.64	190.59	4.67
177.67	214.81	37.14	194.15	8.84
213.18	223.10	9.92	218.10	1.76
186.21	193.80	7.59	190.68	1.02
174.52	188.53	14.01	182.37	2.43

Each color represents polygons in different area
CNT: Center
STH: South
NTH: North
STD: Standard Deviation

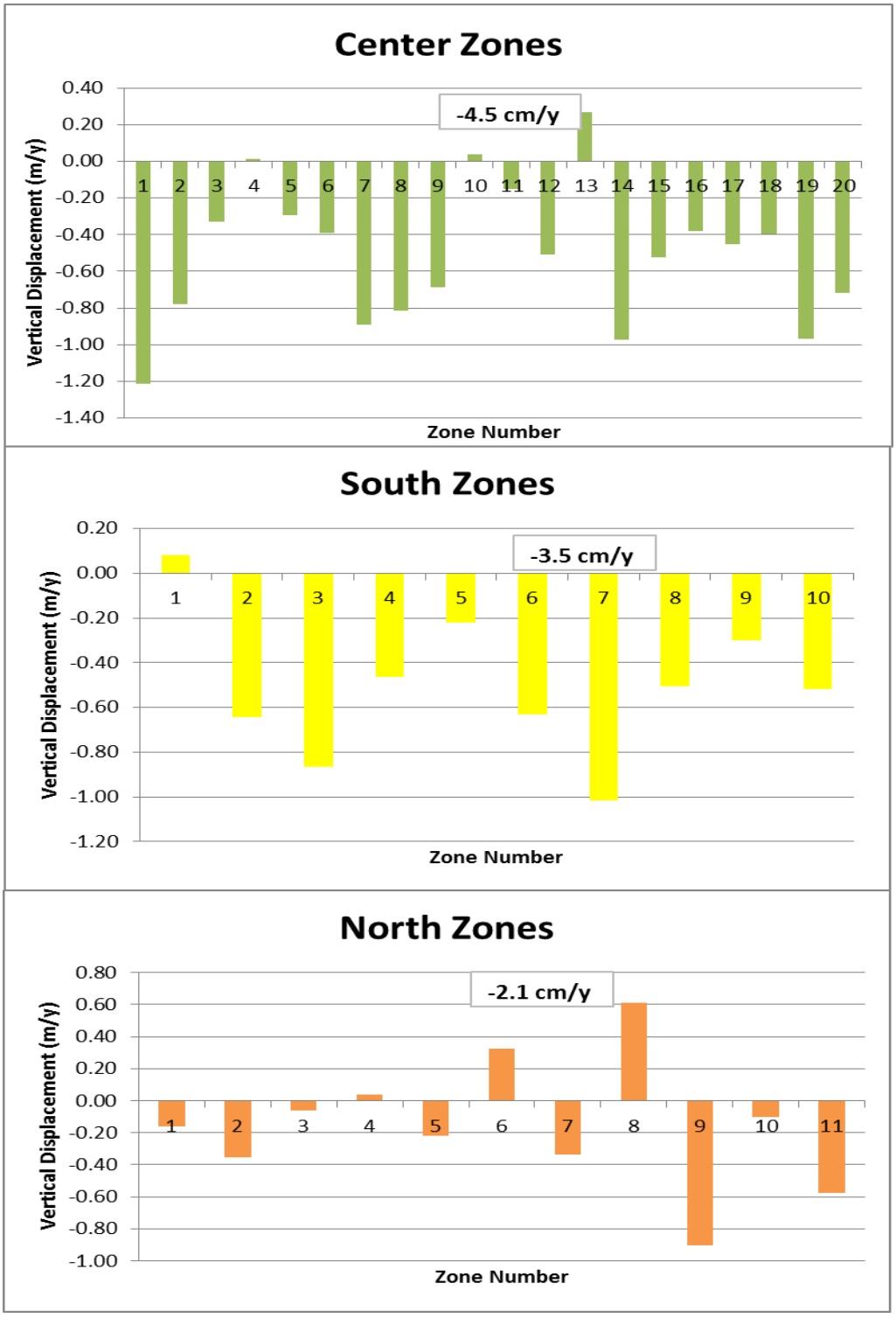

Figure 3.26: Graphs of difference of mean elevation values between 2001 and 2008 LiDAR DEMs for zones of different parts of the Northwest Harris.

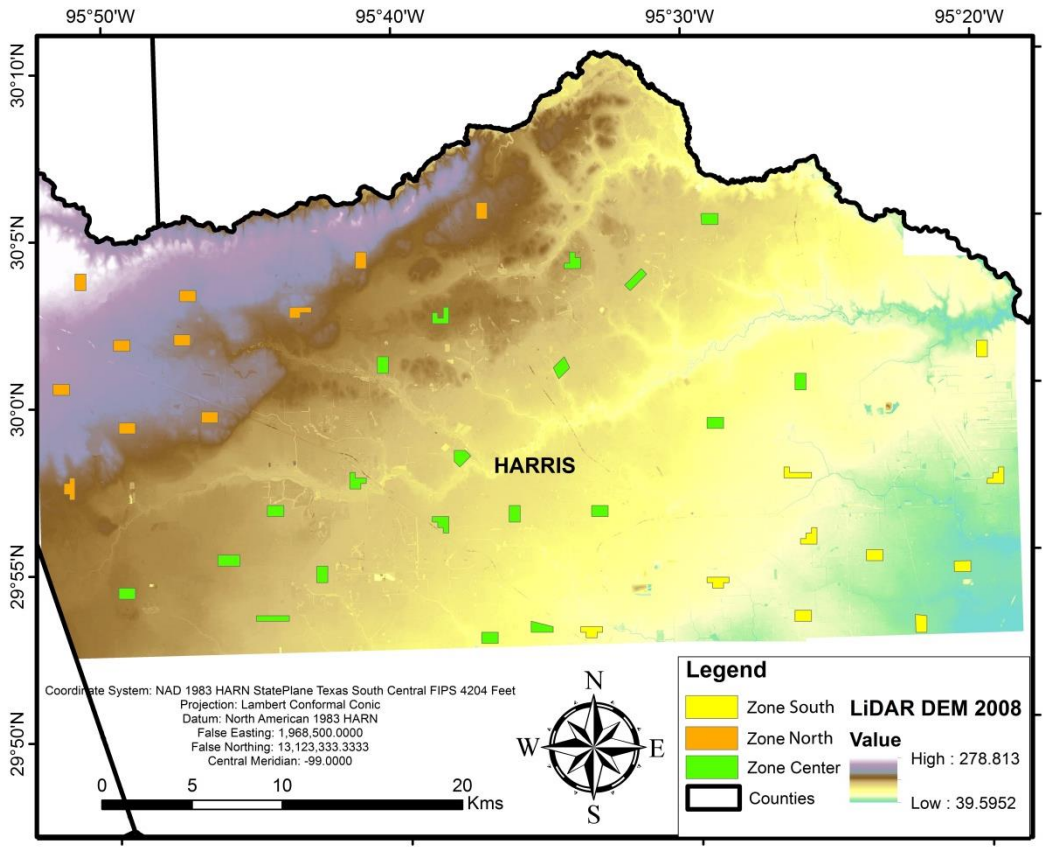

Figure 3.27: Polygons for Zonal Height Computation method. Polygons in orange are for the north part, polygons in green are for the central part, and polygons in yellow are for the south part of the study area. The DEM of the Northwest Harris is also displayed.

Table 3.3 Zonal Statistics of 2001 and 2008 LiDAR DEM for Hockley Fault

2001					
ID	MIN(m)	MAX(m)	Range(m)	MEAN(m)	STD(m)
HUT1	165	168	3	166.40	0.69
HUT2	165	169	4	167.08	0.93
HUT3	166	173	7	168.89	1.41
HUT4	168	175	7	171.76	1.68
HUT5	171	177	6	174.76	1.39
HUT6	172	174	2	172.85	0.77
HUT7	169	176	7	173.32	1.59
HUT8	174	183	9	178.50	2.01
HUT9	176	184	8	180.06	2.13
HUT10	176	182	6	179.22	1.51
HUT11	177	186	9	181.79	2.28
HUT12	172	185	13	177.56	2.83
HUT13	171	176	5	173.11	1.01
HUT14	172	177	5	174.37	1.43
HUT15	172	178	6	175.15	1.60
HUT16	172	179	7	175.01	1.85
HUT17	171	175	4	172.93	0.90
HUT18	172	175	3	173.96	0.76
HUT19	175	180	5	177.33	1.31
HUT20	174	179	5	176.83	1.44
HUT21	175	182	7	178.39	1.75
HUT22	176	182	6	178.62	1.52
HUT23	176	183	7	180.11	1.63
HUT24	175	180	5	177.38	1.27
HUT25	176	182	6	179.55	1.77
HUT26	177	185	8	181.32	1.78
HUT27	179	184	5	181.90	1.30
HUT28	179	185	6	181.86	1.47
HUT29	179	186	7	181.64	1.44
HUT30	180	188	8	183.50	1.82
HUT31	183	192	9	188.07	2.74
HUT32	182	192	10	185.77	3.14
HUT33	182	187	5	185.48	0.88
HUT34	181	188	7	185.55	1.67
HUT35	181	188	7	185.27	1.63
HUT36	182	187	5	185.41	1.07
HUT37	184	188	4	186.15	0.99
HUT38	183	188	5	186.27	1.25
HUT39	182	189	7	185.89	1.53
HUT40	181	188	7	185.64	2.10
HUT41	184	189	5	186.75	1.00
HUT42	185	189	4	187.24	0.98
HUT43	185	188	3	186.98	0.81
HUT44	184	188	4	186.36	1.14
HUT45	178	187	9	182.71	2.07

2008					
ID	MIN(m)	MAX(m)	Range(m)	MEAN(m)	STD(m)
HUT1	163.82	167.13	3.31	165.37	0.64
HUT2	164.23	168.81	4.58	166.51	1.00
HUT3	165.18	172.42	7.24	168.51	1.35
HUT4	167.91	175.14	7.23	171.61	1.53
HUT5	171.18	177.09	5.91	174.96	1.33
HUT6	171.04	174.65	3.61	172.54	0.80
HUT7	168.71	176.25	7.55	173.10	1.41
HUT8	173.35	182.82	9.47	178.02	1.96
HUT9	175.57	183.97	8.40	179.82	2.10
HUT10	175.58	182.05	6.46	178.69	1.48
HUT11	176.73	186.09	9.36	181.49	2.16
HUT12	171.86	185.33	13.47	177.53	2.76
HUT13	170.68	175.34	4.66	172.68	0.93
HUT14	171.55	177.81	6.26	174.12	1.40
HUT15	171.52	177.74	6.23	174.62	1.48
HUT16	171.44	178.66	7.22	174.80	1.74
HUT17	170.19	175.54	5.35	172.70	1.06
HUT18	171.90	175.73	3.84	173.69	0.80
HUT19	174.23	180.32	6.09	177.08	1.25
HUT20	173.14	179.78	6.64	176.50	1.41
HUT21	175.73	186.11	10.39	179.79	2.37
HUT22	177.36	186.74	9.38	182.47	2.63
HUT23	176.36	183.88	7.52	179.92	1.50
HUT24	174.74	181.29	6.56	177.65	1.36
HUT25	176.15	183.39	7.24	179.86	1.87
HUT26	177.02	185.80	8.78	181.46	1.70
HUT27	179.10	185.08	5.97	181.94	1.33
HUT28	177.75	186.19	8.44	182.71	1.45
HUT29	177.98	186.76	8.78	181.70	1.55
HUT30	179.89	190.54	10.66	183.70	2.01
HUT31	182.06	192.27	10.21	187.57	2.66
HUT32	180.81	192.18	11.37	185.62	3.30
HUT33	181.70	187.66	5.96	185.13	0.76
HUT34	180.27	188.57	8.30	185.22	1.64
HUT35	179.94	188.97	9.02	185.11	1.50
HUT36	181.94	188.12	6.18	185.31	1.05
HUT37	183.34	189.18	5.84	185.88	1.07
HUT38	182.97	189.63	6.65	186.01	1.31
HUT39	181.59	189.07	7.49	185.47	1.54
HUT40	180.58	188.53	7.95	185.33	2.04
HUT41	182.16	188.26	6.10	186.22	0.99
HUT42	184.57	188.71	4.13	186.71	0.96
HUT43	183.78	188.06	4.28	186.37	0.86
HUT44	183.36	188.17	4.81	186.01	1.01
HUT45	177.78	187.14	9.36	182.53	1.99

HDT1	156	159	3	157.6	0.7
HDT2	157	159	2	158	0.7
HDT3	157	160	3	158.6	0.7
HDT4	157	159	2	157.7	0.6
HDT5	158	161	3	159.5	0.8
HDT6	159	163	4	161.2	0.8
HDT7	160	163	3	161.6	0.8
HDT8	160	163	3	161.5	0.7
HDT9	160	165	5	162.5	1
HDT10	162	165	3	163.6	0.9
HDT11	162	165	3	163.9	0.8
HDT12	164	166	2	164.8	0.5
HDT13	163	165	2	164.3	0.6
HDT14	162	165	3	163.3	0.6
HDT15	162	165	3	163.3	0.6
HDT16	163	165	2	163.7	0.5
HDT17	162	166	4	164.3	0.8
HDT18	162	165	3	163.4	0.7

HDT1	163.8	167.1	3.3084	165.4	0.6
HDT2	164.2	168.8	4.5824	166.5	1
HDT3	165.2	172.4	7.2397	168.5	1.3
HDT4	167.9	175.1	7.2294	171.6	1.5
HDT5	171.2	177.1	5.9092	175	1.3
HDT6	171	174.7	3.6095	172.5	0.8
HDT7	168.7	176.3	7.5462	173.1	1.4
HDT8	173.4	182.8	9.4719	178	2
HDT9	175.6	184	8.395	179.8	2.1
HDT10	175.6	182	6.4648	178.7	1.5
HDT11	176.7	186.1	9.3602	181.5	2.2
HDT12	171.9	185.3	13.472	177.5	2.8
HDT13	170.7	175.3	4.6554	172.7	0.9
HDT14	171.6	177.8	6.2569	174.1	1.4
HDT15	171.5	177.7	6.2274	174.6	1.5
HDT16	171.4	178.7	7.2205	174.8	1.7
HDT17	170.2	175.5	5.3454	172.7	1.1
HDT18	171.9	175.7	3.8377	173.7	0.8

Table 3.3 : Continued

2001					
ID	MIN(m)	MAX(m)	Range(m)	MEAN(m)	STD(m)
HDT19	162	165	3	163.3	0.9
HDT20	160	165	5	163.4	1.2
HDT21	162	165	3	163.2	0.9
HDT22	162	165	3	163.5	1
HDT23	163	167	4	165.2	0.9
HDT24	160	167	7	164.5	2.1
HDT25	160	167	7	163.3	1.6
HDT26	160	167	7	164.2	1.4
HDT27	163	167	4	165.1	0.9
HDT28	164	169	5	166.4	1.3
HDT29	164	170	6	166.6	1.3
HDT30	166	172	6	168.7	1.3
HDT31	169	174	5	171.6	1.1
HDT32	168	177	9	172.6	2.1
HDT33	170	176	6	173.5	1.2
HDT34	171	176	5	173.4	1.3
HDT35	167	176	9	172.8	2.3
HDT36	172	177	5	174.6	1.1
HDT37	172	177	5	175.3	1.2
HDT38	172	177	5	175.2	1.2
HDT39	172	177	5	175.1	1
HDT40	172	177	5	174.9	1.1
HDT41	173	177	4	175	1
HDT42	173	178	5	174.9	1.3
HDT43	172	176	4	173.8	1
HDT44	172	175	3	172.9	0.9
HDT45	171	173	2	171.5	0.7

2008					
ID	MIN(m)	MAX(m)	Range(m)	MEAN(m)	STD(m)
HDT19	174.2	180.3	6.0923	177.1	1.3
HDT20	173.1	179.8	6.6376	176.5	1.4
HDT21	175.7	186.1	10.387	179.8	2.4
HDT22	177.4	186.7	9.3844	182.5	2.6
HDT23	176.4	183.9	7.5169	179.9	1.5
HDT24	174.7	181.3	6.5551	177.6	1.4
HDT25	176.1	183.4	7.2449	179.9	1.9
HDT26	177	185.8	8.7815	181.5	1.7
HDT27	179.1	185.1	5.9725	181.9	1.3
HDT28	177.8	186.2	8.4396	182.7	1.4
HDT29	178	186.8	8.7792	181.7	1.6
HDT30	179.9	190.5	10.657	183.7	2
HDT31	182.1	192.3	10.208	187.6	2.7
HDT32	180.8	192.2	11.366	185.6	3.3
HDT33	181.7	187.7	5.9608	185.1	0.8
HDT34	180.3	188.6	8.3035	185.2	1.6
HDT35	179.9	189	9.0246	185.1	1.5
HDT36	181.9	188.1	6.1817	185.3	1.1
HDT37	183.3	189.2	5.8414	185.9	1.1
HDT38	183	189.6	6.6539	186	1.3
HDT39	181.6	189.1	7.486	185.5	1.5
HDT40	180.6	188.5	7.9487	185.3	2
HDT41	182.2	188.3	6.0986	186.2	1
HDT42	184.6	188.7	4.1349	186.7	1
HDT43	183.8	188.1	4.2814	186.4	0.9
HDT44	183.4	188.2	4.8126	186	1
HDT45	177.8	187.1	9.3563	182.5	2

HUT: Hockley Up Thrown
HDT: Hockley Down Thrown
SDT: Standard Deviation

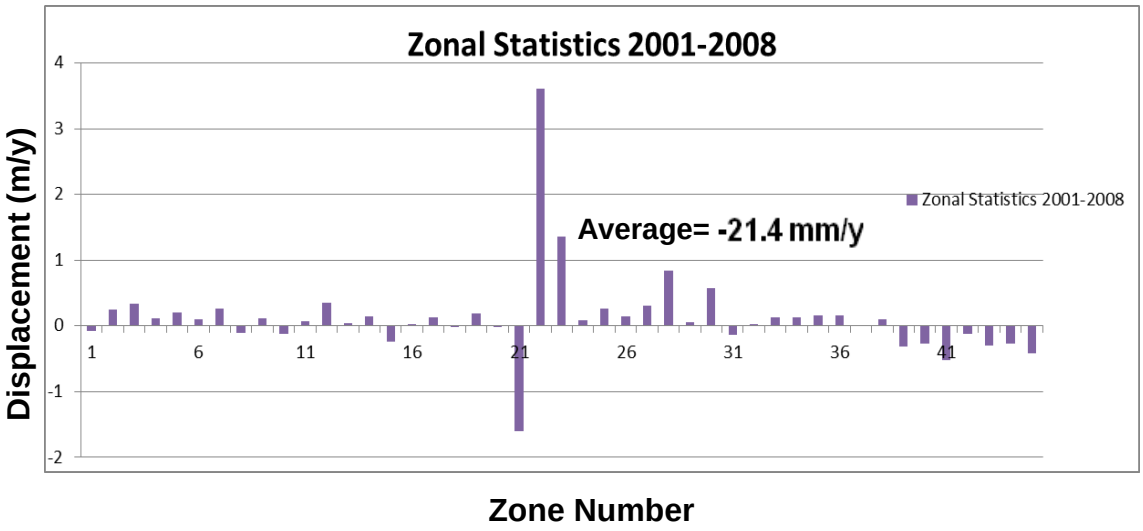

Figure 3.28: Graph of difference of the mean elevation values of northwest and southeast of the Hockley Fault

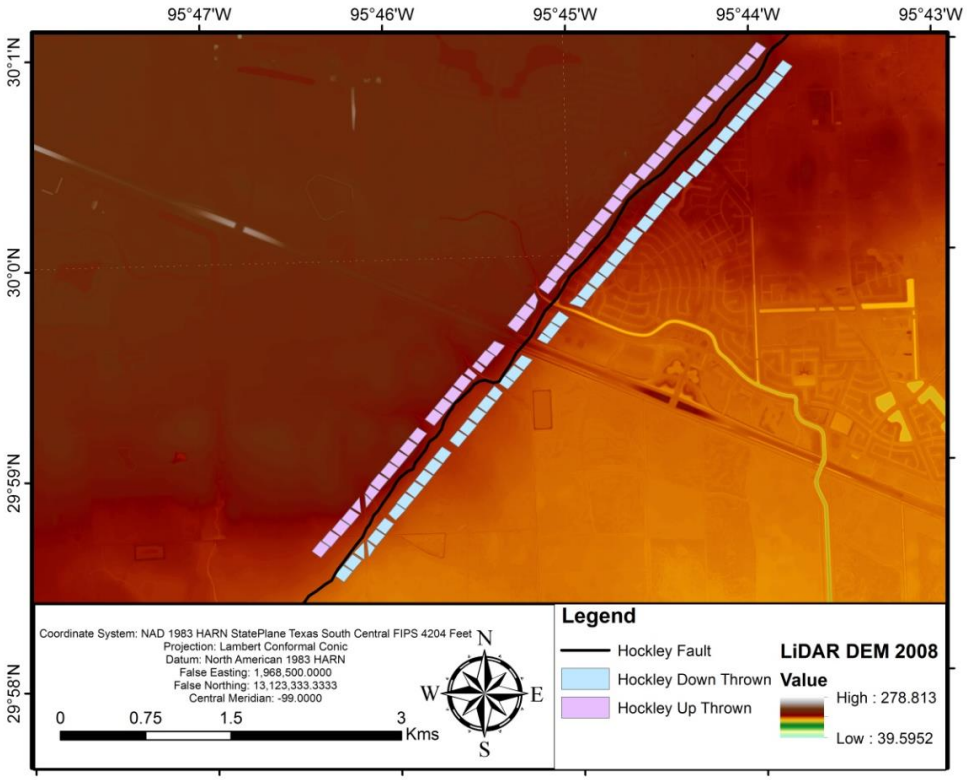

Figure 3.29: Height computation zones of Hockley Fault. Black line on the 2008 LiDAR DEM shows the location of theHockley Fault. Pink zones and blue zones represent the upthrown and downthrown of Hockley Fault, respectively.

3.3 InSAR

3.3.1 Persistent Scatterer

Eight (8) ERS1 and seventeen (17) ERS2 data from 1992 to 2002 were processed and analyzed using Persistent Scatterer (PS) Method to clarify the subsidence rate of the Northwest Harris area precisely. Figure 3.29 presents the Persistent Scatterer results of 25 ERS image. The points with hot colors (yellow to red) express that the area is moving away from the satellite, i.e., the area are subsiding. The cold colors (green to blue) show the motion of the land surface towards the satellite, in other words, uplift. The unit of the surface deformation in Figure 3.29 is in mm/y. The PS method reduces the atmospheric and topographic anomalies. Therefore, small scale (mm/y) surface deformations are not affected by noises. However, some hot colored points are recognized over the cold colored points, and vice versa. It was decided that these points may be caused by the trees that scatter radar signals persistently. Figure 3.29 demonstrates that the area is subsiding at different rates. It is seen that the subsidence pattern is changing from the northwest to central portion of the Northwest Harris area. The northwest portion of study area is subsiding with the rate -17 mm/y at most. Besides, the central portion is sinking with rates between -27 and -47 mm/y.

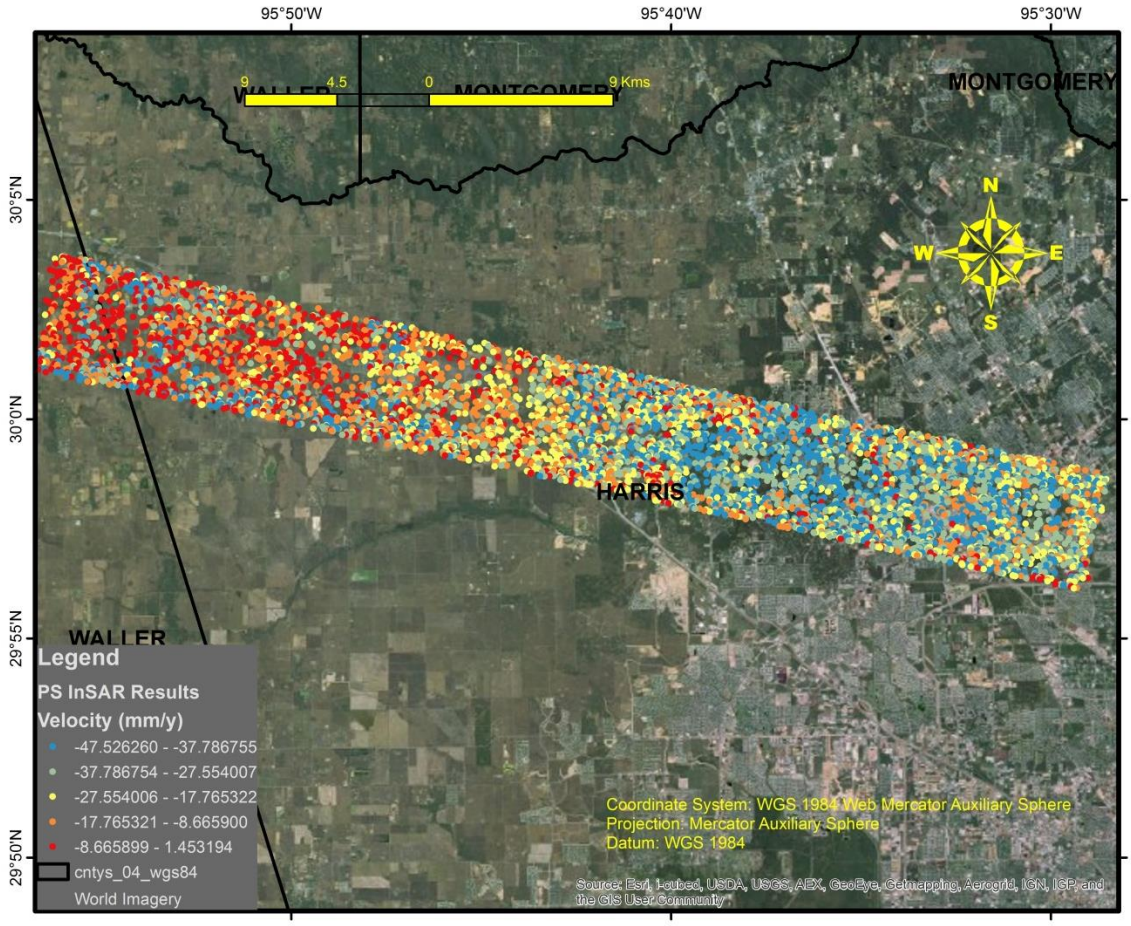

Figure 3.30: Persistent Scatterer (PS) InSAR results map. The colored points from blue to red presents the PS InSAR values over the Northwest Harris County. The cold colors (blue to yellow) represent high rate subsidence, and the hot colored (yellow to red) points show low rate subsidence in the study area.

3.4 Groundwater

The groundwater observation data acquired from USGS were processed and evaluated to reveal the rate of change in the Chicot and Evangeline aquifer systems. The groundwater level change was analyzed for two different time span (1990-2011and 2008-2011). These periods were selected in order to compare the remote sensing results with rate of change in groundwater level.

The combination of the result of both the Chicot Aquifer and the Evangeline Aquifer was modeled and given in Figure 3.37. The cold colors (blue to yellow) represent the decline in groundwater level. The hot colors on the map show increasing groundwater level. The highest decrease in groundwater level is located in the central portion of the Northwest Harris area. However, the groundwater level is increasing on the northwest and southeast portion of the study area.

To see the trend of change in groundwater level, the data of 261 groundwater observation wells were averaged per year for the period 1990-2012 and it plotted to graph shown in Figure 3.38. The blue line represents groundwater level, and orange area shows the depth to groundwater in meter scale. It is realized that the groundwater level is the lowest in 2000.

3.4.1 Chicot Aquifer

The rate of change in groundwater in the Chicot Aquifer is elucidated. Table 3.4 expresses the results of groundwater level change for ninety six (96) groundwater observation wells for the period 1990-2011 and 2008-2011.

Figure 3.30 and 3.32 demonstrate the surface model of the rate of change in groundwater for different time intervals. The colors from blue to green present decline in groundwater level and the colors from yellow to red show rise in groundwater level. The blue points in Figure 3.30 and Figure 3.32 display the locations of groundwater observation wells. It is seen that the water level is decreasing in the center of study area for long and short terms. However, the groundwater level change in recent time is declining faster than in past. The northwest portion of study area shows increasing trend of groundwater level in Figure 3.30 and Figure 3.32. Figure 3.31 demonstrates the general trend of groundwater level change in the Chicot Aquifer. It is seen that the groundwater level was declining before 2000. However, it began to rise after 2000.

Table 3.4: Groundwater level change of the Chicot Aquifer for 1990-2011, and 2008-2011. The difference between 'Chicot' and 'Chicot Evangeline' is that some of the wells are penetrating both aquifers.

Well No	Latitude	Longitude	Field Name	Rate for Long change (1990-2011) (m/y)	Rate of change (short term) (2008-2011) (m/y)
294031095554201	29.675278	-95.928333	Chicot	-0.18	-0.89
294108095324702	29.692083	-95.564139	Chicot	0.60	-5.71
294142095515301	29.695153	-95.864981	Chicot	0.48	0.48
294144095351002	29.6955	-95.586556	Chicot Evangeline	1.18	-1.08
294147095344303	29.696222	-95.578944	Chicot Evangeline	1.02	-0.46
294201095355601	29.700278	-95.598889	Chicot Evangeline	1.17	-1.28
294211095370901	29.703056	-95.619167	Chicot Evangeline	0.68	3.76
294219095583601	29.705278	-95.976667	Chicot	-0.08	-0.48
294252095362101	29.714444	-95.605833	Chicot Evangeline	0.77	-0.39
294407095403701	29.717611	-95.688389	Chicot	-0.17	0.73
294319095305901	29.721944	-95.516389	Chicot Evangeline	1.00	-4.19
294328095290402	29.724722	-95.479444	Chicot	1.66	-1.60
294329095284602	29.724722	-95.479444	Chicot Evangeline	1.37	-1.60
294333095275602	29.725833	-95.465556	Chicot Evangeline	1.69	4.94
294338095270406	29.727222	-95.451111	Chicot	1.21	-0.31
294338095270405	29.727222	-95.451111	Chicot	0.34	-0.31
294338095270404	29.727222	-95.451111	Chicot Evangeline	0.62	-0.31
294340095311103	29.727778	-95.519722	Chicot Evangeline	1.32	-4.92
294348095303702	29.727778	-95.510556	Chicot Evangeline	1.02	-5.05
294405095412301	29.734667	-95.689806	Chicot	-0.06	-0.38
294302095411801	29.7355	-95.677167	Chicot	-0.42	0.28
294503095373201	29.750944	-95.625583	Chicot	-0.01	-0.01
294529095371801	29.758056	-95.621667	Chicot Evangeline	0.45	0.75
294538095344601	29.760861	-95.57925	Chicot	0.02	0.62
294548095372801	29.763333	-95.624444	Chicot Evangeline	0.98	0.39
294519095383201	29.766111	-95.633806	Chicot Evangeline	-0.14	-6.17
294606095383901	29.7686	-95.644319	Chicot	-0.04	-0.04
294620095440501	29.772222	-95.734722	Chicot	-0.04	-0.07
294708095363201	29.785556	-95.609056	Chicot Evangeline	2.99	-0.81
294717095401001	29.788056	-95.669444	Chicot Evangeline	-0.81	-2.33
294721095361001	29.789222	-95.602722	Chicot Evangeline	1.56	4.39
294726095351102	29.790556	-95.586389	Chicot	-0.08	-2.36

Table 3.4: Continued

Well No	Latitude	Longitude	Field Name	Rate for Long change (1990-2011) (m/y)	Rate of change (short term) (2008-2011) (m/y)
294726095351102	29.790556	-95.586389	Chicot	0.00	-2.36
294726095351102	29.790556	-95.586389	Chicot	0.04	-2.36
294800095344101	29.800083	-95.699528	Chicot	-0.02	-3.06
294807095484901	29.802056	-95.757556	Chicot	-0.02	-0.23
294807095452701	29.802639	-95.819028	Chicot	-0.14	-0.23
294900095312101	29.816667	-95.5225	Chicot Evangeline	2.20	-0.67
294919095320501	29.821917	-95.534778	Chicot	-0.06	0.23
294921095312907	29.8225	-95.524722	Chicot Evangeline	1.50	-0.30
294950095313701	29.830556	-95.526944	Chicot Evangeline	3.67	1.01
294952095342601	29.831111	-95.573889	Chicot Evangeline	1.80	-5.28
294957095310801	29.832611	-95.518778	Chicot	-0.07	-0.26
294959095405501	29.833528	-95.682889	Chicot Evangeline	-0.52	1.77
295046095492901	29.846167	-95.824833	Chicot	-0.08	-0.08
295049095253101	29.847	-95.425306	Chicot	-0.11	-0.31
295133095273201	29.859056	-95.45875	Chicot	-0.04	-0.07
295150095302401	29.864028	-95.506722	Chicot	-0.16	-0.28
295207095262102	29.868611	-95.436472	Chicot	1.42	2.38
295228095262901	29.874444	-95.441389	Chicot Evangeline	2.27	-2.56
295232095294101	29.875472	-95.49475	Chicot	-0.12	-0.17
295246095351301	29.879444	-95.586944	Chicot Evangeline	1.48	-7.04
295247095344701	29.879722	-95.579722	Chicot Evangeline	1.20	-6.76
295249095370701	29.879917	-95.618056	Chicot Evangeline	1.86	-0.03
295249095411301	29.880389	-95.686917	Chicot	-0.08	-0.03
295258095354201	29.882778	-95.595	Chicot Evangeline	2.10	0.06
295358095374101	29.899361	-95.627944	Chicot	0.03	-0.07
295505095462201	29.918417	-95.773278	Chicot Evangeline	0.01	0.10
295522095291902	29.924611	-95.487389	Chicot	0.31	0.69
295557095360901	29.932583	-95.602444	Chicot	-0.19	-0.17
295558095442301	29.932778	-95.739722	Chicot Evangeline	-1.20	-2.87
295633095335201	29.942444	-95.564444	Chicot	-0.10	1.76
295633095324401	29.9425	-95.545556	Chicot Evangeline	-0.20	1.76
295646095324601	29.946111	-95.546111	Chicot Evangeline	-0.43	2.00
295650095322301	29.947222	-95.54	Chicot Evangeline	0.28	0.28
295704095320301	29.952611	-95.535111	Chicot Evangeline	1.11	0.53

Table 3.4: Continued

Well No	Latitude	Longitude	Field Name	Rate for Long change (1990-2011) (m/y)	Rate of change (short term) (2008-2011) (m/y)
295705095320201	29.953111	-95.535111	Chicot Evangeline	1.21	-2.28
295711095330201	29.953139	-95.373	Chicot	0.03	-3.85
295711095222301	29.953167	-95.551	Chicot Evangeline	0.81	-3.85
295714095361701	29.953806	-95.604667	Chicot	0.06	-0.07
295720095290001	29.955417	-95.483361	Chicot	-0.07	0.00
295723095340201	29.962722	-95.556556	Chicot Evangeline	0.92	-5.22
295754095324901	29.9705	-95.546583	Chicot Evangeline	0.78	-0.39
295840095525901	29.978694	-95.882556	Chicot Evangeline	0.02	-0.26
295842095430201	29.979028	-95.717861	Chicot	-0.23	-0.57
295924095450601	29.989778	-95.753639	Chicot Evangeline	-0.91	3.06
300007095354701	30.002	-95.595806	Chicot	-0.28	-0.09
300026095225401	30.007389	-95.398472	Chicot	-0.11	-0.20
300036095400101	30.009917	-95.666917	Chicot	-0.13	-0.57
300044095293201	30.01225	-95.522139	Chicot	-0.01	-12.35
300101095211301	30.016944	-95.353611	Chicot	0.43	0.33
300239095431101	30.044083	-95.719722	Chicot	0.02	-0.19
300333095291701	30.059278	-95.488028	Chicot	-0.21	-0.18
300351095232601	30.064194	-95.390472	Chicot	-0.19	-0.45
300447095444101	30.07985	-95.74485	Chicot	-0.33	-1.89
300457095245801	30.0825	-95.416111	Chicot	-0.06	-0.40
300503095260001	30.084083	-95.433444	Chicot	-0.26	-0.13
300521095365101	30.089167	-95.614167	Chicot	-0.41	2.17
300643095214301	30.111611	-95.363167	Chicot	-0.73	-0.73
300714095493401	30.120556	-95.826111	Chicot	11.47	11.47
300717095463601	30.121278	-95.77675	Chicot	-0.29	-0.78
300754095451101	30.131556	-95.753139	Chicot	0.37	0.48
300906095392001	30.151556	-95.6555	Chicot	-0.31	-0.51
300915095343701	30.154167	-95.576861	Chicot	0.43	-0.07
300954095421101	30.164889	-95.703139	Chicot	-0.20	-0.77
301139095393801	30.194167	-95.660556	Chicot	-0.07	-0.26

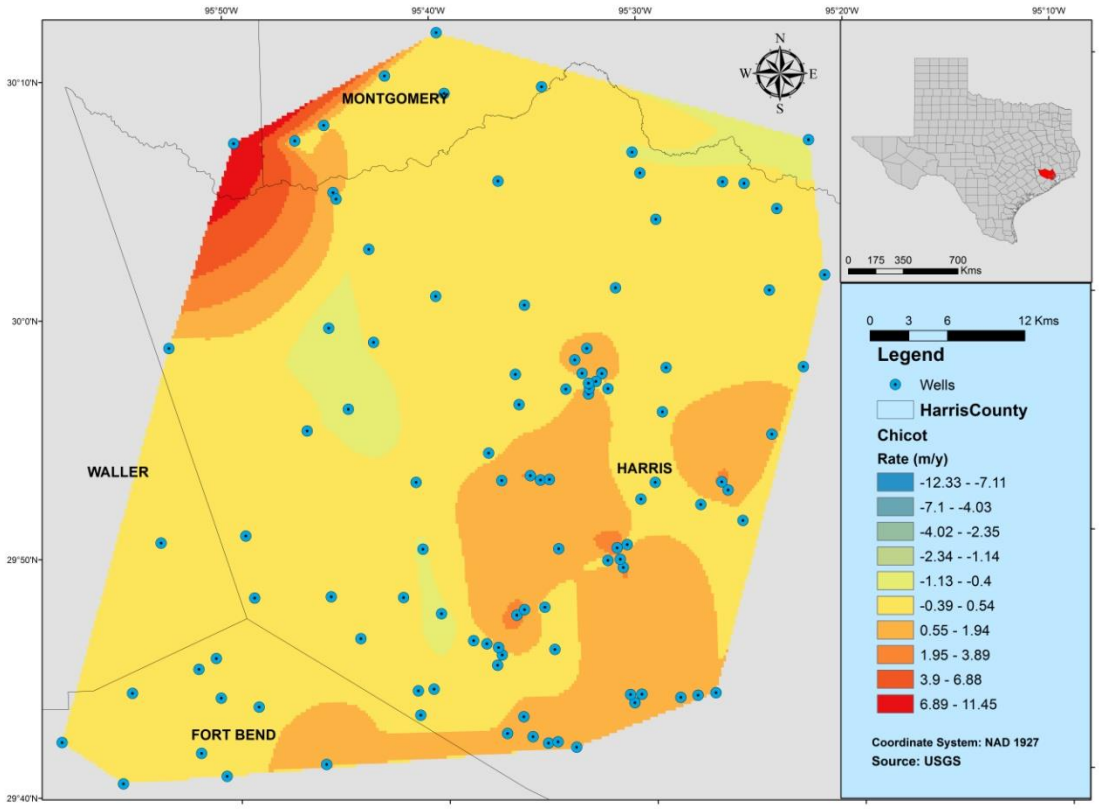

Figure 3.31: Rate of the groundwater level change map for 1990-2011. Hot colors from red to yellow represents increasing water level. Colors from yellow to blue show the area where groundwater level is declining. The map represent positive trend, or enlarging, most of the part of the Northwest Harris County. The blue points represent the well locations which are penetrating 'Chicot' and 'Chicot Evangeline' aquifers.

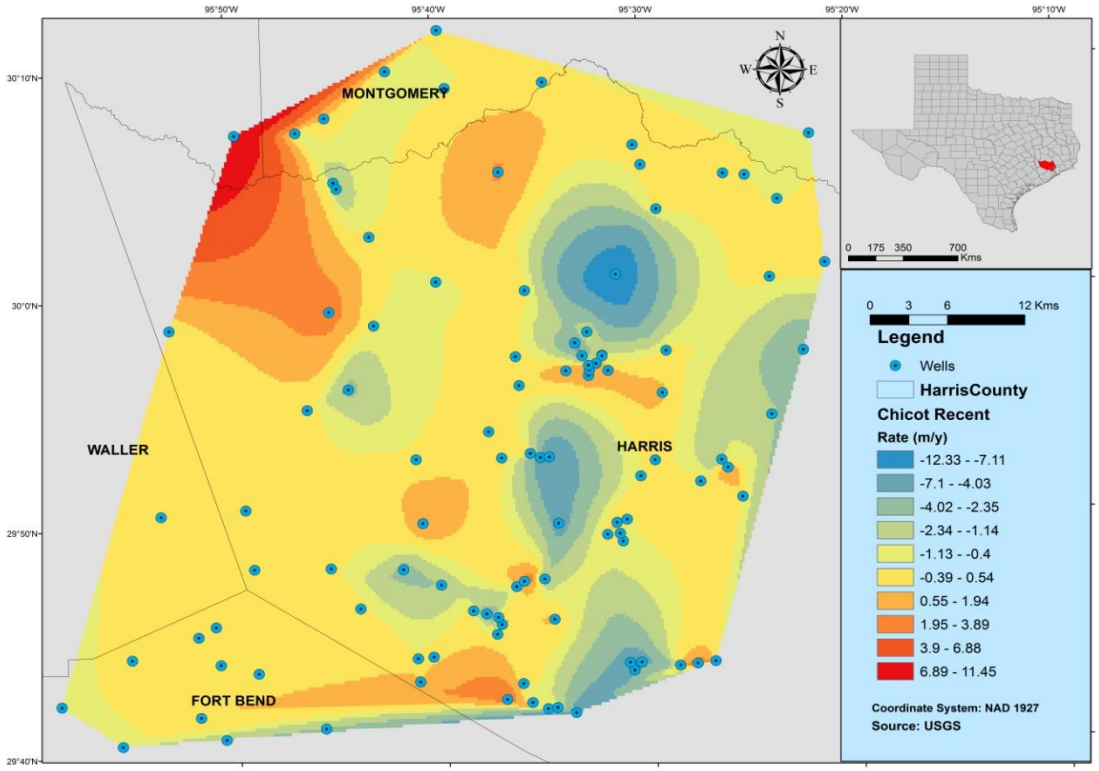

Figure 3.32: Rate of the groundwater level change map for 2008-2011. Colors represent the same trend shown in Figure 3.30. The map presents both positive (at the edges) and negative (at the centre) trends.

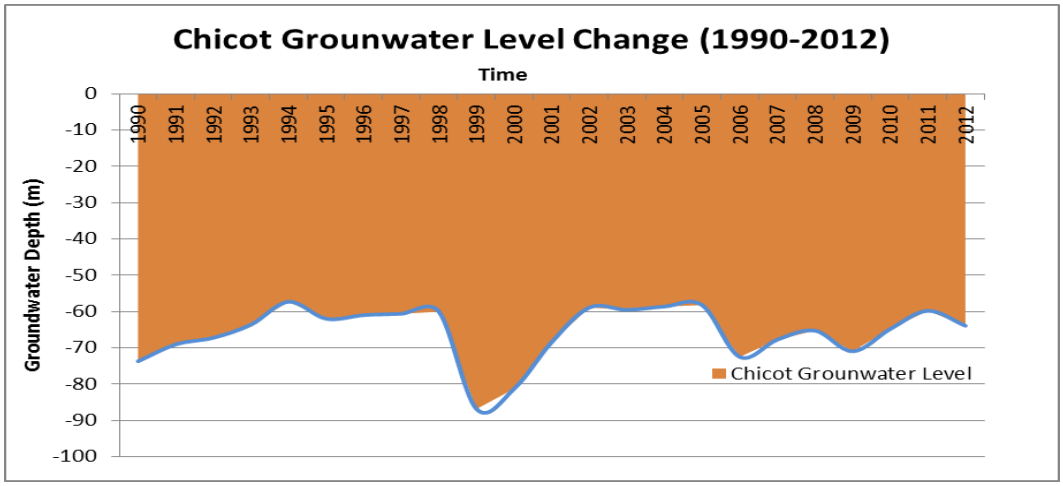

Figure 3.33: Graph of general change in groundwater in Chicot Aquifer. This graph shows annual average of water level change in Chicot Aquifer gathered by 110 wells. Blue line represents the water surface, and orange area is to show the depth to groundwater level.

3.4.2 Evangeline Aquifer

The rate of change in groundwater level in the Evangeline Aquifer for the period 1990-2011 and 2008-2011 is given in Table 3.5. Figure 3.33 and Figure 3.35 present the map of the water level alteration in these time periods. The green points on each map demonstrate the groundwater observation well locations of the Evangeline Aquifer. The cold colors (blue-green) indicate the decrease in groundwater level. The hot colors (yellow-red) on both figures signify groundwater level increase in the Evangeline Aquifer. It is recognized that the water level is dropping down on the central part of the Northwest Harris area. Yet, the map for the period 2008-2011 represents more reduction of groundwater with respect to annual groundwater level change between 1990 and 2011. Figure 3.34 demonstrates the general trend of groundwater level change in the Evangeline Aquifer. Similar to the general trend of groundwater level change in Chicot aquifer, the groundwater level of the Evangeline Aquifer is decreasing before 2000 and increasing after 2000.

Table 3.5: Groundwater level change of Evangeline Aquifer for 1990-2011, and 2008-2011

WellNo	Latitude	Longitude	Field Name	Rate for Long change (1990-2011) (m/y)	Rate of change (short term) (2008-2011) (m/y)
294112095462501	29.686861	-95.773792	Evangeline	-1.61	-4.06
294134095470301	29.692672	-95.784067	Evangeline	-2.60	-2.60
294144095351002	29.6955	-95.586556	Chicot Evangeline	1.18	-1.08
294147095344303	29.696222	-95.578944	Chicot Evangeline	1.02	-0.46
294201095355601	29.700278	-95.598889	Chicot Evangeline	1.17	-1.28
294209095494701	29.702222	-95.829722	Evangeline	-4.09	-4.09
294211095370901	29.703056	-95.619167	Chicot Evangeline	0.68	3.76
294213095322001	29.703611	-95.538889	Evangeline	1.37	-2.96
294215095301502	29.704167	-95.504167	Evangeline	1.13	-2.59
294216095301601	29.704444	-95.504444	Evangeline	1.17	-3.62
294219095470501	29.707944	-95.787	Evangeline	-1.57	-6.30
294243095371201	29.711944	-95.62	Evangeline	0.91	3.72
294252095362101	29.714444	-95.605833	Chicot Evangeline	0.77	-0.39
294301095341801	29.716944	-95.571667	Evangeline	1.01	7.78
294306095371801	29.718333	-95.621667	Evangeline	0.45	-0.42
294313095365101	29.720278	-95.614167	Evangeline	0.41	-0.07
294317095313001	29.721389	-95.523611	Evangeline	1.17	-5.46
294319095305901	29.721944	-95.516389	Chicot Evangeline	1.00	-4.19
294323095300102	29.723056	-95.500278	Evangeline	1.17	-1.38
294326095293002	29.723889	-95.491667	Evangeline	1.23	-3.13
294328095290402	29.724444	-95.484444	Evangeline	1.41	2.67
294329095284602	29.724722	-95.479444	Chicot Evangeline	1.37	-1.60
294333095275602	29.725833	-95.465556	Chicot Evangeline	1.69	4.94
294338095270406	29.727222	-95.451111	Evangeline	1.69	-0.31
294338095270405	29.727222	-95.451111	Chicot Evangeline	0.62	-0.31
294338095270404	29.727222	-95.451111	Evangeline	1.55	-0.31
294338095270401	29.727222	-95.451111	Evangeline	1.13	-0.31
294340095311103	29.727778	-95.519722	Chicot Evangeline	1.32	-4.92
294348095303702	29.727778	-95.510556	Chicot Evangeline	1.02	-5.05
294348095303702	29.727778	-95.510556	Evangeline	1.36	-5.05
294352095385501	29.731111	-95.648611	Evangeline	-0.19	9.33
294356095391501	29.732222	-95.654167	Evangeline	0.07	2.28
294403095460101	29.734167	-95.766944	Evangeline	-2.66	-2.66
294414095364202	29.737222	-95.611667	Evangeline	0.03	-6.20

Table 3.5: Continued

WellNo	Latitude	Longitude	Field Name	Rate for Long change (1990-2011) (m/y)	Rate of change (short term) (2008-2011) (m/y)
294442095450801	29.745317	-95.752458	Evangeline	-1.51	-4.76
294452095354501	29.747778	-95.595833	Evangeline	0.90	-6.43
294529095371801	29.758056	-95.621667	Chicot Evangeline	0.45	0.75
294548095372801	29.763333	-95.624444	Chicot Evangeline	0.98	0.39
294548095372801	29.763333	-95.624444	Evangeline	-0.97	0.39
294519095383201	29.766111	-95.633806	Chicot Evangeline	-0.14	-6.17
294607095492201	29.769178	-95.822308	Evangeline	-1.07	-2.30
294627095375801	29.774167	-95.632778	Evangeline	-0.45	-6.99
294656095382501	29.782222	-95.640278	Evangeline	-0.13	-7.47
294708095363201	29.785556	-95.609056	Chicot Evangeline	2.99	-0.81
294712095401301	29.786667	-95.670278	Evangeline	0.62	-1.09
294731095414201	29.787444	-95.694417	Evangeline	-0.49	-1.70
294717095401001	29.788056	-95.669444	Chicot Evangeline	-0.81	-2.33
294721095361001	29.789222	-95.602722	Chicot Evangeline	1.56	4.39
294723095382601	29.789722	-95.640556	Evangeline	1.88	-4.71
294723095382601	29.789722	-95.640556	Evangeline	1.13	-4.71
294724095351401	29.790167	-95.587361	Evangeline	0.71	3.49
294726095351102	29.790694	-95.586139	Evangeline	0.91	-2.36
294735095344001	29.793056	-95.577778	Evangeline	3.86	-9.31
294747095444701	29.796917	-95.747278	Evangeline	-1.66	-2.98
294753095454001	29.797306	-95.761833	Evangeline	-1.54	-0.49
294800095344101	29.8	-95.578056	Evangeline	1.75	-3.06
294820095342002	29.805556	-95.572222	Evangeline	1.56	-2.18
294844095342401	29.812222	-95.573333	Evangeline	3.53	-4.53
294900095312101	29.816667	-95.5225	Chicot Evangeline	2.20	-0.67
294916095314601	29.821389	-95.529722	Evangeline	2.81	-0.41
294921095312907	29.8225	-95.524722	Chicot Evangeline	1.50	-0.30
294925095341201	29.824667	-95.570306	Evangeline	1.81	-8.59
294931095240801	29.825278	-95.402222	Evangeline	2.21	-0.23
294950095313701	29.830556	-95.526944	Chicot Evangeline	3.67	1.01
294950095313701	29.830556	-95.526944	Evangeline	5.71	1.01
294952095342601	29.831111	-95.573889	Chicot Evangeline	1.80	-5.28
294959095405501	29.833528	-95.682889	Chicot Evangeline	-0.52	1.77
295001095240302	29.833611	-95.400833	Evangeline	2.86	-0.19

Table 3.5: Continued

WellNo	Latitude	Longitude	Field Name	Rate for Long change (1990-2011) (m/y)	Rate of change (short term) (2008-2011) (m/y)
295019095240801	29.838611	-95.402222	Evangeline	2.70	-1.49
295027095312301	29.841194	-95.523417	Evangeline	5.68	-2.70
295044095565201	29.845556	-95.947778	Evangeline	-0.03	-13.80
295048095240801	29.846667	-95.402222	Evangeline	2.86	-1.26
295155095282401	29.865278	-95.473333	Evangeline	2.57	1.19
295203095261401	29.867389	-95.437778	Evangeline	2.94	-4.71
295204095261301	29.867528	-95.437611	Evangeline	2.35	-0.97
295218095572701	29.871667	-95.9575	Evangeline	-0.19	-3.13
295228095262901	29.874444	-95.441389	Chicot Evangeline	2.27	-2.56
295228095262901	29.874444	-95.441389	Evangeline	2.30	-2.56
295235095414301	29.876472	-95.691639	Evangeline	-1.71	3.32
295240095375601	29.876833	-95.632583	Evangeline	0.72	-4.90
295243095383101	29.878861	-95.640444	Evangeline	0.30	-3.13
295246095351301	29.879444	-95.586944	Chicot Evangeline	1.48	-7.04
295247095344701	29.879722	-95.579722	Chicot Evangeline	1.20	-6.76
295249095411301	29.880389	-95.686917	Chicot Evangeline	1.86	-0.03
295249095411301	29.880389	-95.686917	Evangeline	2.02	-0.03
295251095264502	29.881	-95.445778	Evangeline	1.91	2.68
295252095300401	29.881111	-95.501111	Evangeline	2.43	-2.81
295254095361901	29.882389	-95.605639	Evangeline	1.85	2.68
295258095354201	29.882778	-95.595	Chicot Evangeline	2.10	0.06
295301095393901	29.884361	-95.660972	Evangeline	-0.10	1.41
295306095270502	29.884917	-95.451306	Evangeline	1.50	-2.19
295316095562801	29.887778	-95.941111	Evangeline	0.17	-0.41
295339095383201	29.894194	-95.641917	Evangeline	0.13	2.71
295505095462201	29.918417	-95.773278	Chicot Evangeline	0.01	0.10
295544095462401	29.928917	-95.774083	Evangeline	-0.02	-0.28
295558095442301	29.932778	-95.739722	Chicot Evangeline	-1.20	-2.87
295633095324401	29.9425	-95.545556	Chicot Evangeline	-0.20	1.76
295644095261001	29.9458	-95.436633	Evangeline	2.08	-3.87
295646095324601	29.946111	-95.546111	Chicot Evangeline	-0.43	2.00
295650095322301	29.947222	-95.54	Chicot Evangeline	0.28	0.28
295709096013101	29.9525	-96.025278	Evangeline	-0.01	-1.16
295704095320301	29.952611	-95.535111	Chicot Evangeline	1.11	0.53

Table 3.5: Continued

WellNo	Latitude	Longitude	Field Name	Rate for Long change (1990-2011) (m/y)	Rate of change (short term) (2008-2011) (m/y)
295705095320201	29.953111	-95.535111	Chicot Evangeline	1.21	-2.28
295711095330201	29.953167	-95.551	Chicot Evangeline	0.81	-3.85
295722095372001	29.956806	-95.622361	Evangeline	0.38	-0.19
295723095340201	29.962722	-95.556556	Chicot Evangeline	0.92	-5.22
295754095324901	29.9705	-95.546583	Chicot Evangeline	0.78	-0.39
295831095530801	29.9755	-95.885694	Evangeline	0.32	-0.86
295840095525901	29.978694	-95.882556	Chicot Evangeline	0.02	-0.26
295842095430201	29.979028	-95.717861	Evangeline	-1.29	-0.57
295850095201301	29.980317	-95.33745	Evangeline	0.28	-3.14
295855095204301	29.982033	-95.345667	Evangeline	0.08	-2.71
295924095450601	29.989778	-95.753639	Chicot Evangeline	-0.91	3.06
300018095225701	30.005	-95.3825	Evangeline	-0.02	-0.23
300050095275301	30.0142	-95.464569	Evangeline	-0.01	5.66
300056095335601	30.015556	-95.565556	Evangeline	0.51	0.41
300104095365101	30.017917	-95.614417	Evangeline	-4.17	-3.13
300123095264501	30.023056	-95.445833	Evangeline	0.46	0.86
300146095510402	30.029444	-95.851111	Evangeline	-0.11	-0.86
300157095292501	30.0325	-95.490278	Evangeline	-1.23	-9.92
300239095431101	30.044083	-95.719722	Evangeline	-0.67	-0.19
300251095265401	30.04865	-95.447525	Evangeline	-1.54	1.54
300301095361301	30.050944	-95.604139	Evangeline	-1.00	0.65
300318095553401	30.055	-95.926111	Evangeline	-0.14	-1.00
300332095553601	30.05875	-95.926778	Evangeline	-0.24	-1.19
300342095282201	30.061611	-95.47275	Evangeline	-1.51	-7.16
300408095485701	30.068889	-95.813056	Evangeline	0.12	-1.86
300414095585601	30.070722	-95.982278	Evangeline	-1.10	-1.62
300507095280201	30.085278	-95.467222	Evangeline	-1.23	1.29
300542096045402	30.095	-96.081667	Evangeline	-0.75	-0.68
300542096045402	30.095	-96.081667	Evangeline	-0.86	-0.68
300544095231501	30.095556	-95.3875	Evangeline	-3.01	-2.49
300551095330401	30.0975	-95.551111	Evangeline	-0.37	-1.23
300556095304102	30.098889	-95.511389	Evangeline	-0.76	-4.53
300621095225201	30.105833	-95.381111	Evangeline	-5.92	-5.92
300637095240801	30.112139	-95.402056	Evangeline	0.68	-0.86

Table 3.5: Continued

WellNo	Latitude	Longitude	Field Name	Rate for Long change (1990-2011) (m/y)	Rate of change (short term) (2008-2011) (m/y)
300728095292901	30.124389	-95.491369	Evangeline	-4.08	-6.53
300732095292101	30.124811	-95.491331	Evangeline	-2.31	-4.26
300730095465001	30.124944	-95.780444	Evangeline	-0.45	-0.72
300731095270701	30.125278	-95.451944	Evangeline	-1.80	-0.46
300740095262701	30.127778	-95.440833	Evangeline	-0.58	0.00
300741095262601	30.128056	-95.440556	Evangeline	0.12	-0.34
300742095244301	30.131278	-95.412167	Evangeline	-0.29	-1.23
300819095315501	30.137528	-95.53325	Evangeline	-0.67	-2.89
300811095291702	30.138219	-95.492439	Evangeline	-2.67	-3.37
300816095274701	30.139914	-95.462897	Evangeline	-0.12	-1.87
300824095274701	30.139972	-95.463139	Evangeline	-0.27	-0.33
300826095270801	30.140556	-95.452222	Evangeline	0.91	-0.13
300822095284201	30.14065	-95.479461	Evangeline	-2.15	-1.31
301020095442801	30.171944	-95.741111	Evangeline	-2.31	-2.31
301318095364501	30.221306	-95.613806	Evangeline	-2.51	-2.51

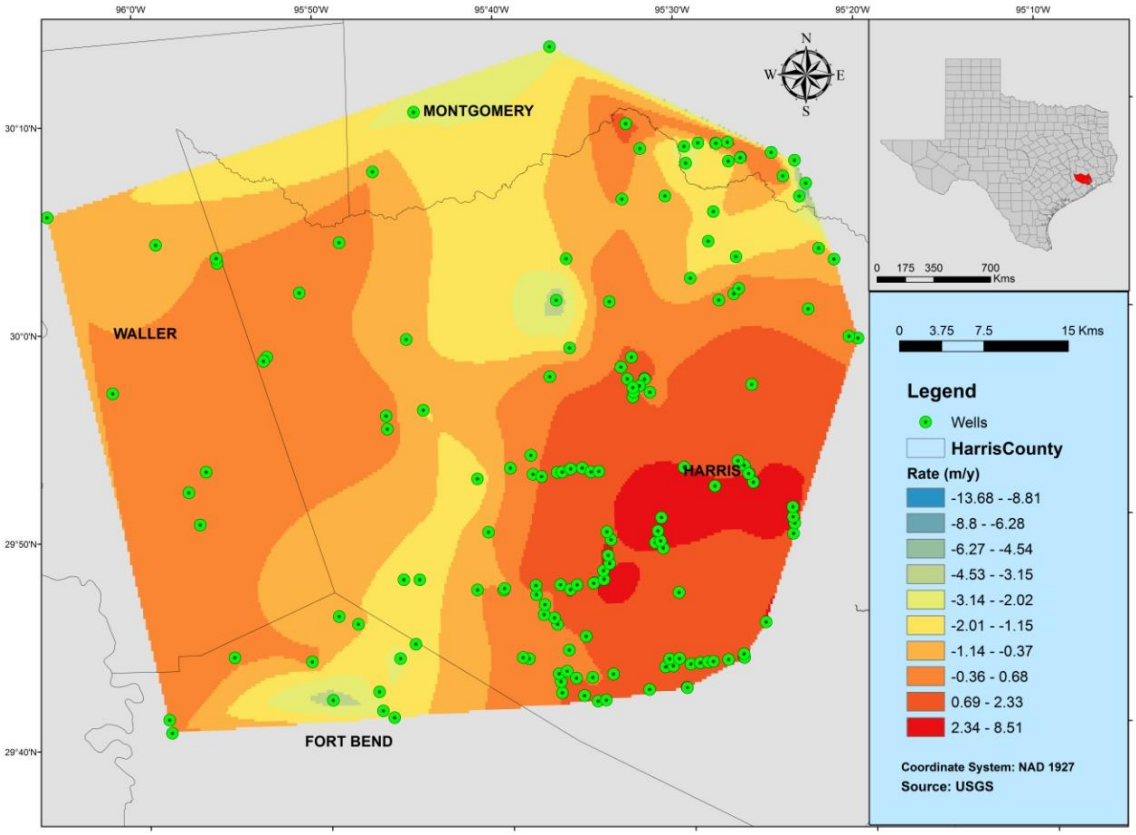

Figure 3.34: Rate of the groundwater level change map for 1990-2011 in the Evangeline Aquifer. Hot colors from red to yellow represents increasing water level. Colors from yellow to blue show the area where groundwater level is declining. The map represent increasing in groundwater most of the part of the Northwest Harris County. The green points show the location of each observation wells which penetrates 'Evangeline' and 'Chicot Evangeline' aquifers.

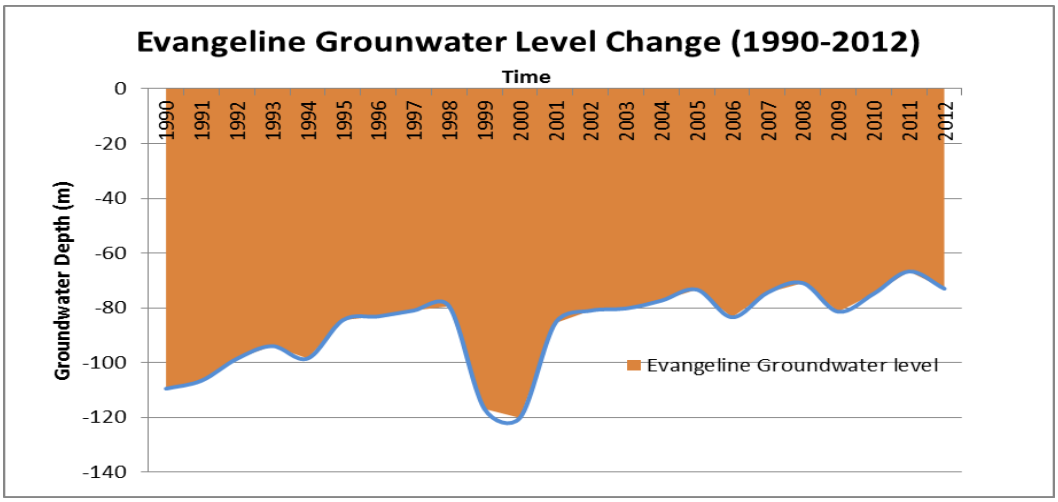

Figure 3.35: Graph of general change in the groundwater level of Evangeline Aquifer. This graph shows annual average of groundwater level change in the Evangeline Aquifer gathered by 151 wells. Blue line represents the water surface, and orange area is to show the depth to groundwater level.

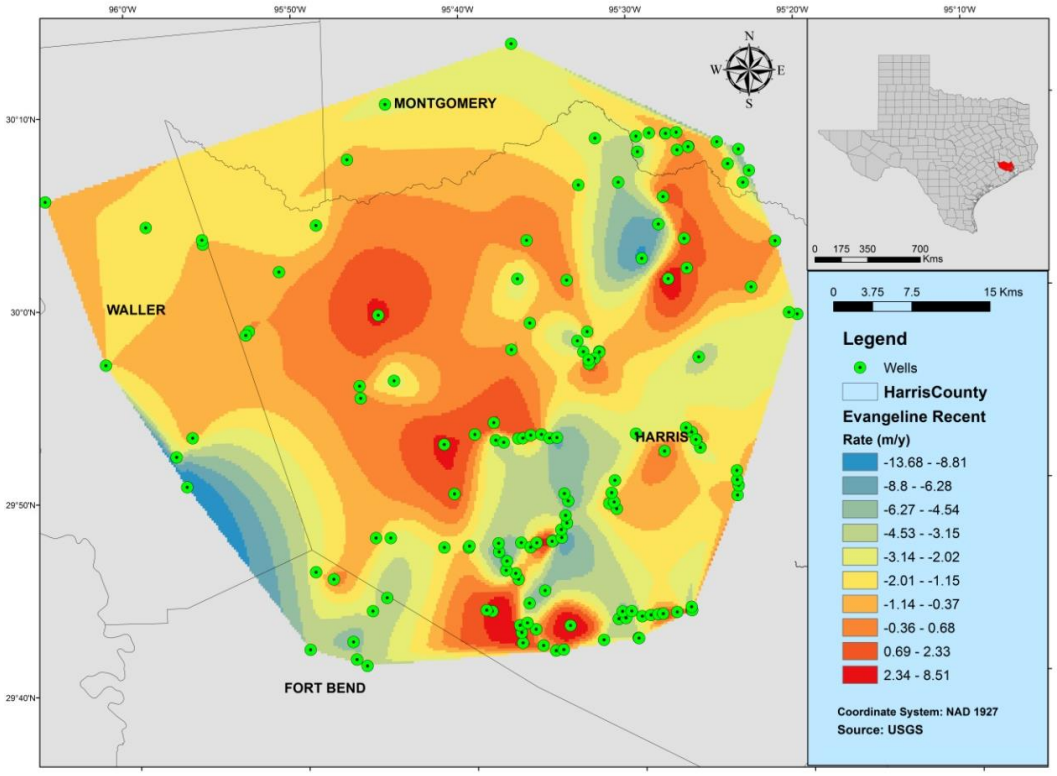

Figure 3.36: The groundwater level change map in the Evangeline aquifer for 2008-2011. Representative colors on the map are same as the colors shown in Figure 3.34. Water level decline is more than Figure 3.34.

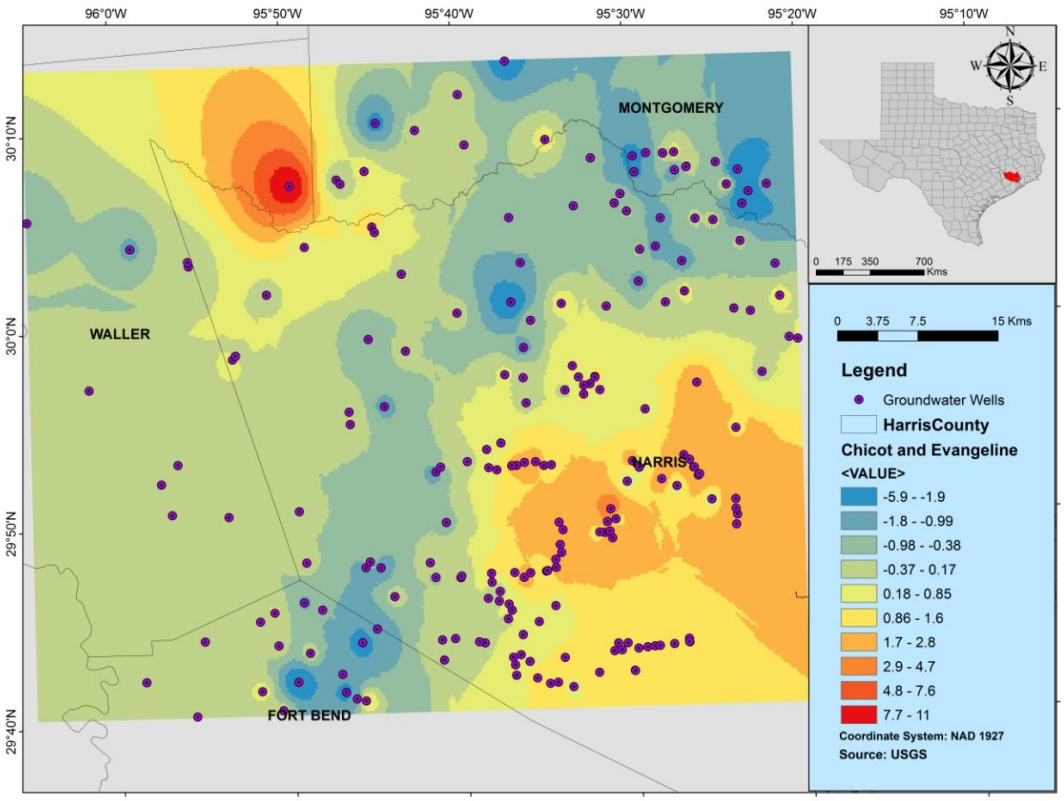

Figure 3.37. The groundwater level change map in both Evangeline and Chicot Aquifers for 2008-2011. Colors from blue to yellow represent decreasing groundwater level, and the colors from yellow to red shows increase in the groundwater level. The map shows that water drop down is the highest in the center of study area.

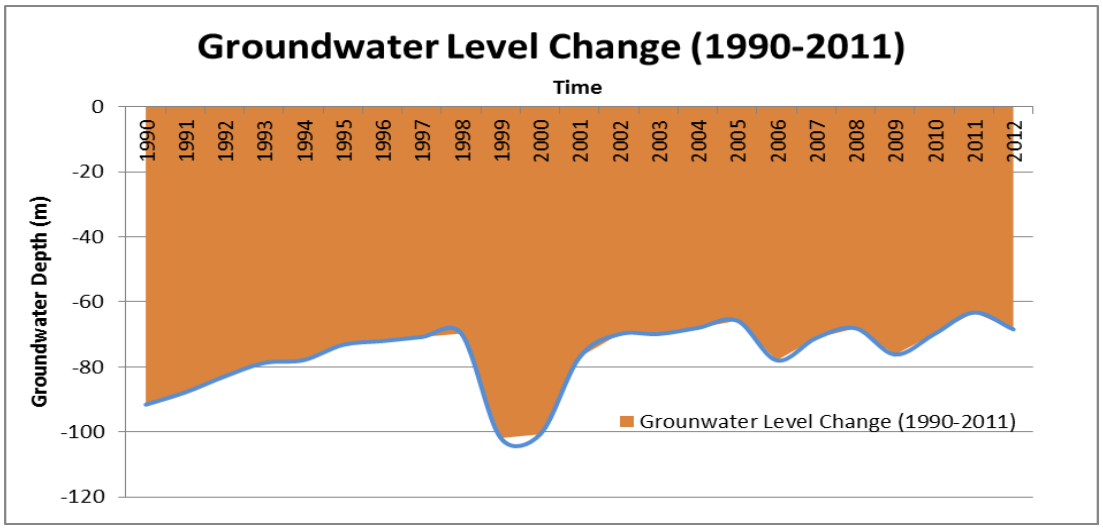

Figure 3.38: Graph of change in groundwater in both Chicot and Evangeline Aquifer. This graph shows annual average of groundwater level change in both aquifers gathered by 261 wells Blue line shows the water surface, and orange area is to show the depth to groundwater level.

3.5 Hydrocarbon

The hydrocarbon production of eight (8) oil fields were processed and analyzed to find out the annual rate of extracted volume of oil and gas in the Northwest Harris area. The rate of change in volume were plotted to create a surface model shown in Figure 3.38.

Hot colors (dark red- yellow) show the area where the oil and gas has been extracted with low rates. Cold colors (blue – yellow) represent high hydrocarbon extraction on the oil fields of study area. The colored points over the study area demonstrate the hydrocarbon production wells of different oil fields. It was noticed that the production rate is the highest on the west portion of study area, Cypress oil field. Also, the annual total hydrocarbon production were calculated and plotted into a graph shown in Figure 3.40. The highest hydrocarbon production is ~ 4.5 billion in 2000. It is seen that the annual oil and gas production is drastically decline (< 2 billion) after the year 2000.

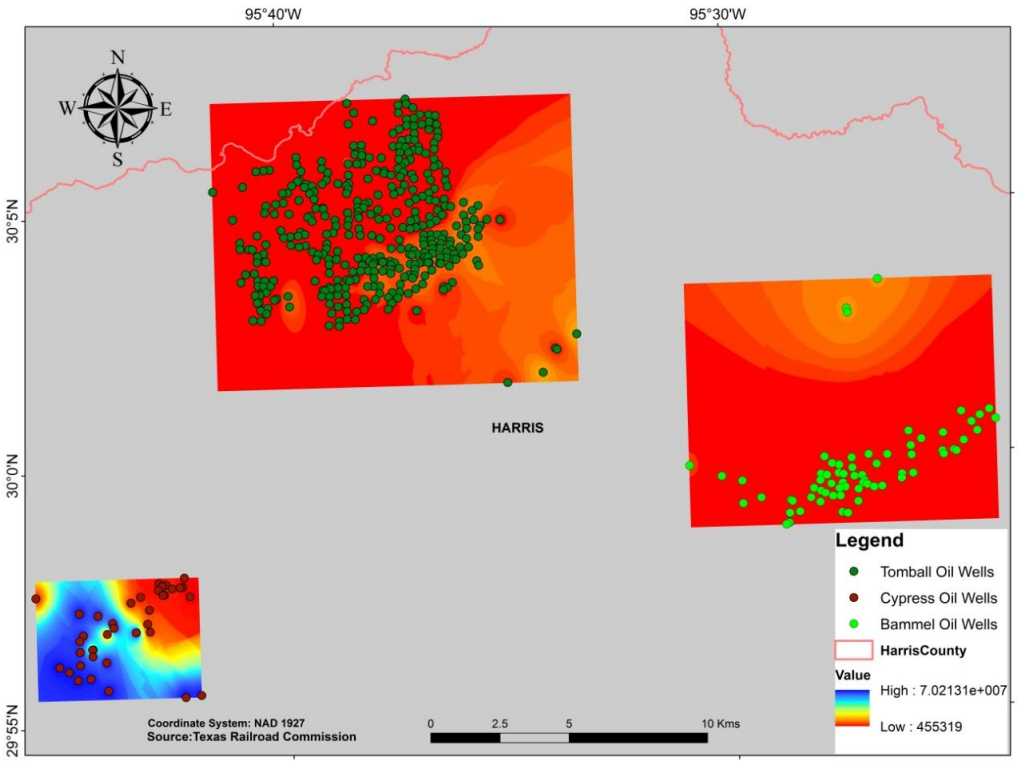

Figure 3.39: Map of hydrocarbon production rate in the Northwest Harris County. The colored points show the well locations for different oil fields. From hot colors to cold colors (red to blue) production rate is increasing. The highest rate of hydrocarbon production is on the Cypress Oil Field area.

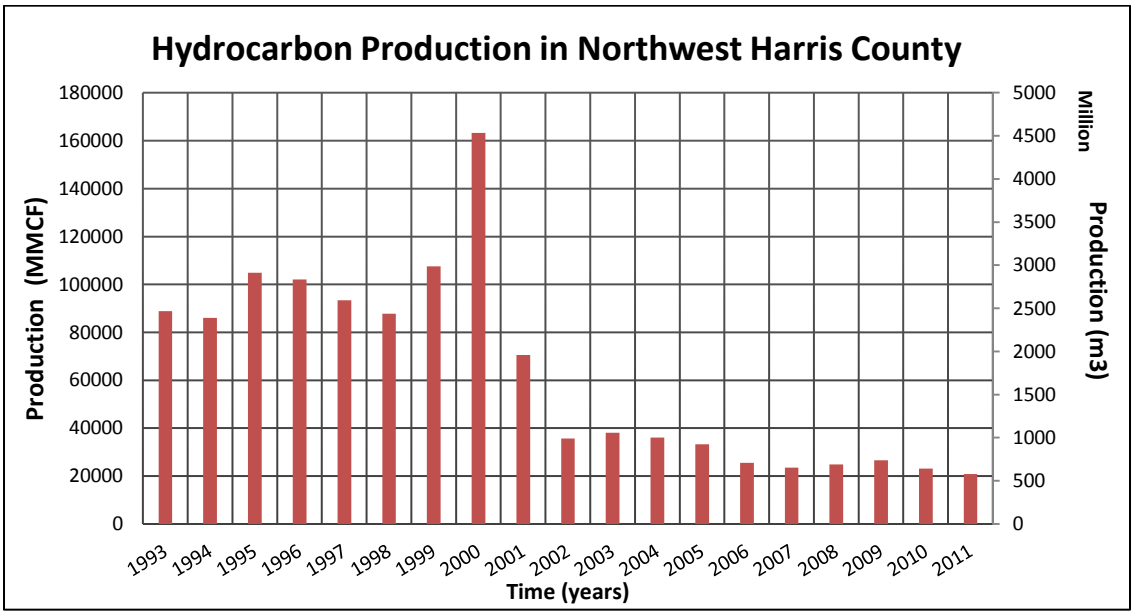

Figure 3.40: Graph of total annual hydrocarbon production between 1993 and 2012.

CHAPTER 4: DISCUSSION

4.1 Subsidence Activity in Northwest Harris

4.1.1 Remote Sensing Analysis

GPS results for the Northwest Harris area demonstrates that the subsidence is concentrated in the center of study area, Jersey Village, as Engelkemeir (2010) and HGCSD (2011) expressed in their research. The rate of subsidence between the year 2002 and 2011 in the central portion of study region is about 3.9 cm/y at most. Engelkemeir & Khan (2008) stated that the subsidence rate for same area is 5.6 cm/y between 1995 and 2005. It is considered that the velocity of subsidence in the Jersey Village area is getting slower after 2000s. Also, data from the Addicks extensometer, which is near the depression area, supports the idea of deceleration of subsidence after the year 2000 (Figure 4.2). Besides, GPS result from 2008 to 2011 manifests that land lowering in northwest region migrates towards northeast of the study area (Figure 4.1).

The zonal statistics method gives almost the same trend of subsidence with GPS results. The polygons on the central portion of the study area and surrounding vicinity represent the height difference between 2001 and 2008 DEMs as 4.5 cm/y. The statistical calculations for northwest (2.1cm/y) and southeast (3.5 cm/y) sections demonstrate the subsidence over the area is declining from center to sides of the study area. The polygonal height calculation method is not a precise, but valuable technique to analyze mean vertical variation of the land surface (Engelkemier & Khan, 2008).

In this study, the purpose of applying the Persistent Scatterer (PS) InSAR method instead of 2-pass and 3-pass interferometry is the highest precision of PS InSAR technique due to

reducing atmospheric and topographic anomalies. The result of the PS InSAR method presents the highest subsidence rate (4.6 cm/y) in the Northwest Harris area in the period 1992-2002. A recent study about subsidence in Houston is found the subsidence in Jersey Village area as 18 cm for the period 1996-2000 using InSAR techniques (Bawden et al., 2012). Therefore, the results of PS InSAR method support both previous studies and the results acquired from GPS and LiDAR techniques shown in Figure 4.3 and Figure 4.4.

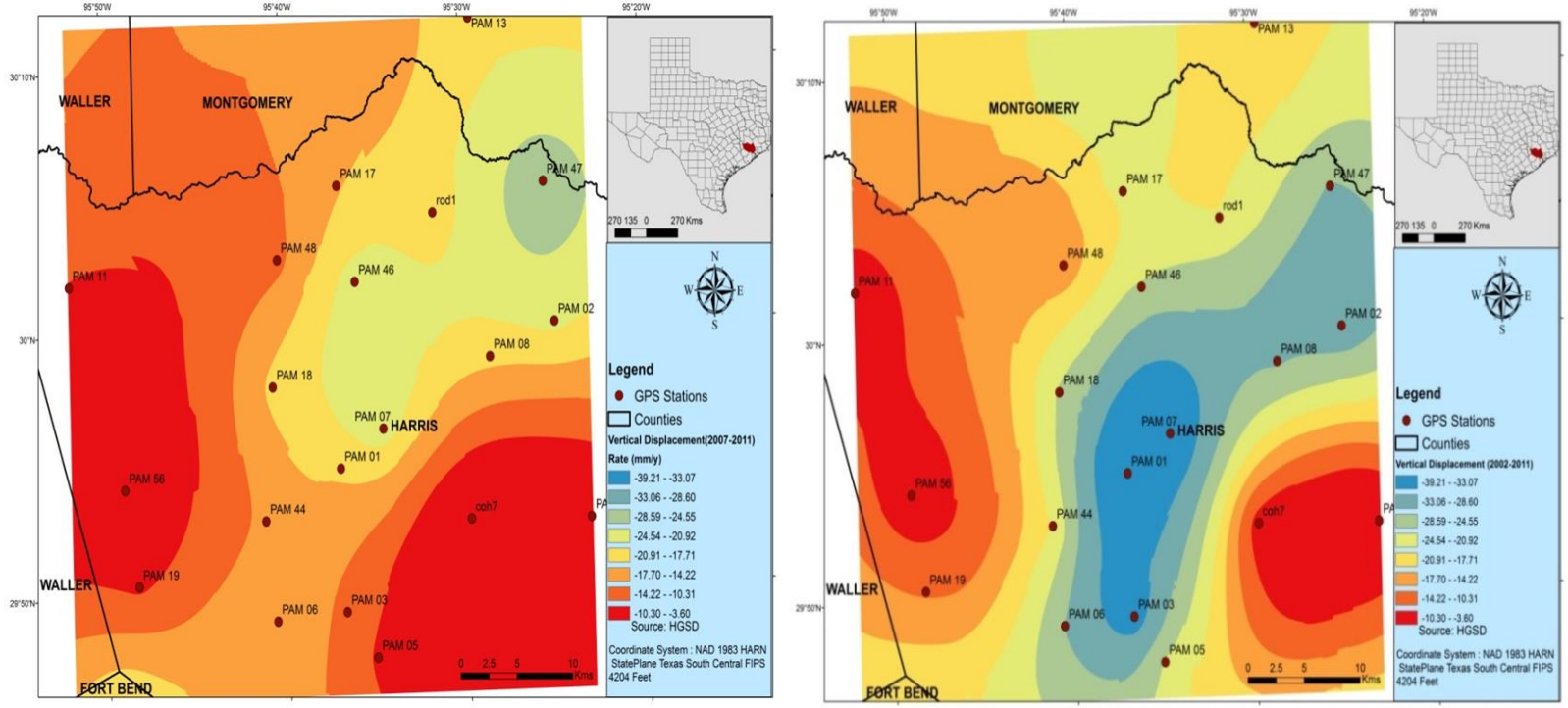

Figure 4.1: The subsidence rate maps for 2002-2011 (on the left) and 2008-2011 (on the right). These two maps represent the change in subsidence between different time spans. When these two maps compared, the migration of the subsidence towards northeast can easily be detected.

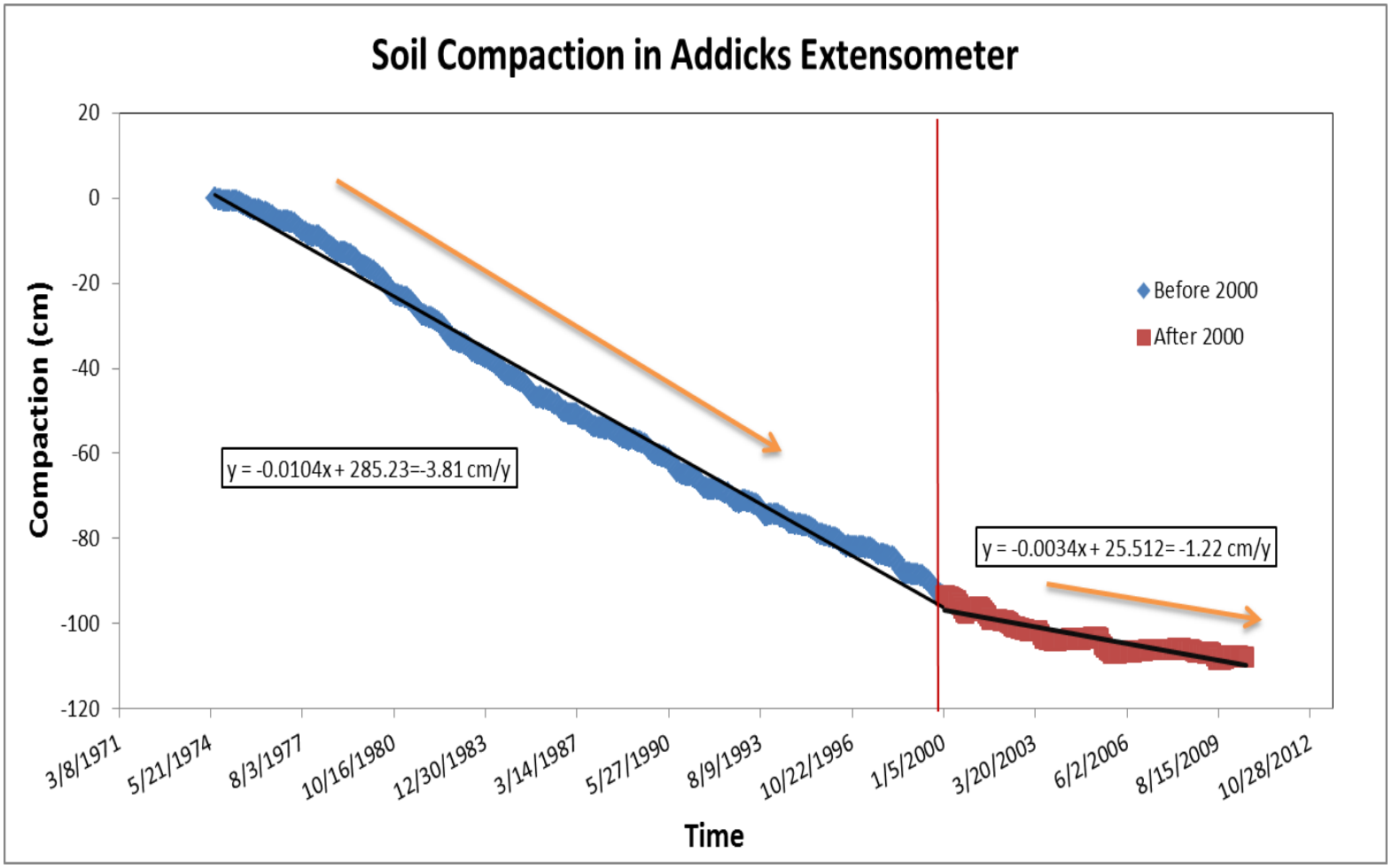

Figure 4.2: Graph of Addicks extensometer. Bold black line represents the year 2000. The orange arrows show the subsidence trend before 2000(3.81 cm/y compaction) and after 2000 (1.22 cm/y compaction). The subsidence began getting slower after 2000. (Source: HGCSD)

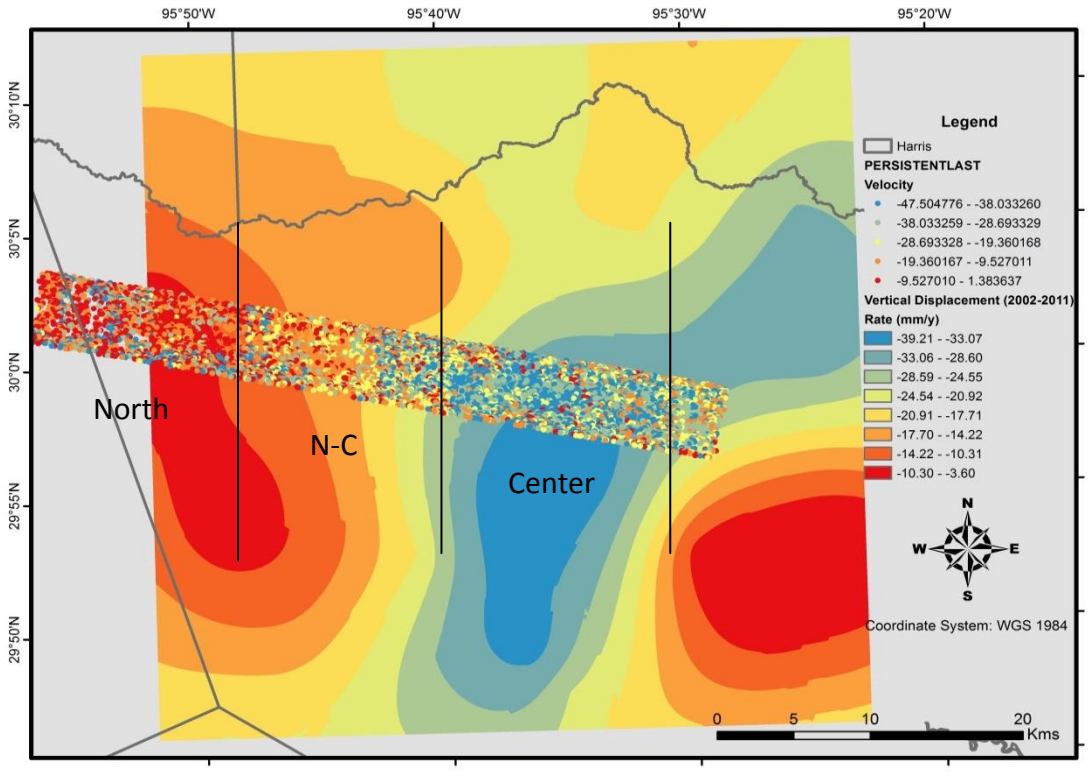

Figure 4.3: Comparison of PS InSAR and GPS results. The points over the continuous colored surface are PS InSAR values. Similar to GPS results, colors of PS InSAR demonstrate different rates of surface deformation. The color trend of PS InSAR and GPS results are almost matched. Both has high subsidence rate near or on the center of the Northwest Harris.

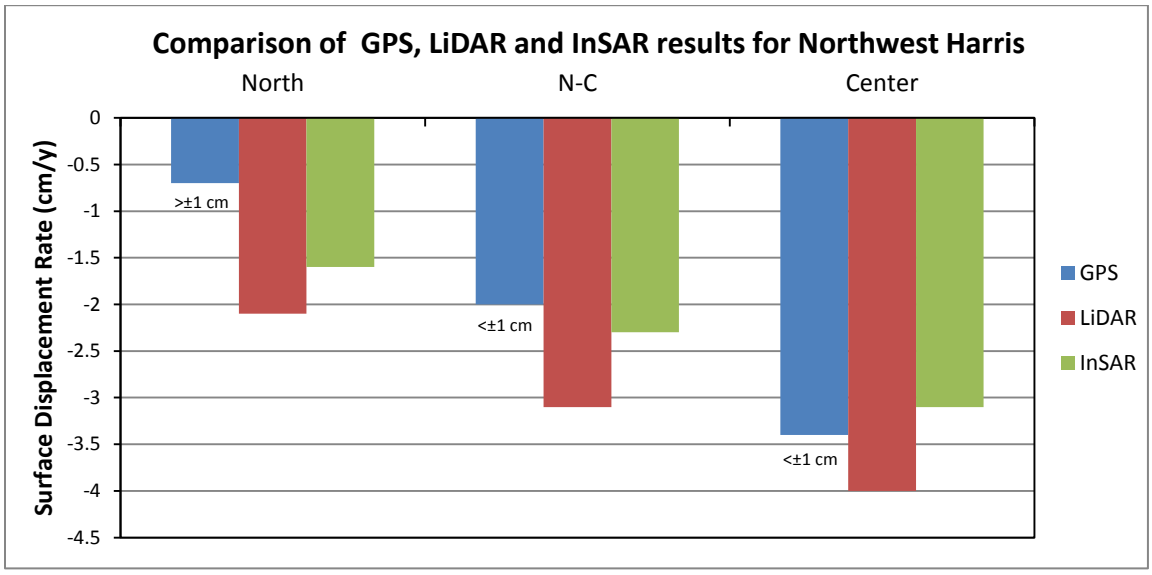

Figure 4.4: The graph of comparison of remote sensing techniques. Each color bar represents each remote sensing technique.

4.2 Fluid Withdrawal in Northwest Harris

4.2.1 Groundwater Level Change and Subsidence

The high rate of groundwater withdrawal is a well-known cause of the subsidence in Houston area documented by many studies. It was first noticed in 1943, and began to be monitored by HGCSD since 1975 (Galloway et al., 1991; Zilkoski et al., 2003). Therefore, the primary purpose of this study is to analyze the groundwater level to clarify its effect on subsidence. The results of the water observations (1990-2011) in the Chicot and Evangeline Aquifers demonstrate that the water level is dropping down with a rate of 2 m/y for both aquifers near the central part of the study area. However, the water level is increasing in the northwest and southeast parts of the study area for both aquifers at most 6 m/y rate. Besides, the surface models for the recent time (2008-2011) present more water-level reduction rather that long-term data for both aquifers. The result of combination of the Evangeline Aquifer and the Chicot Aquifer observational data demonstrates the same trend seen in different aquifers. When these surface modeling results are compared with the general trend of groundwater level change, it was recognized that the groundwater level began to increase after 2000. Annual report of the HGSCD prepared in 2012 stated that the water withdrawal rate for Northwest area started to decrease after 2000 (Figure 4.5). Therefore, the general trend of groundwater level found for this study is supported by HGSCD report. Water withdrawal is not the only factor for change in groundwater level. Also, precipitation reported for the same region demonstrates increasing trend after 2002 (Figure 4.5). When the trend of surface

deformation results compared with the groundwater elevation change, it can be seen that both subsidence and water level drop is higher in central part of the Northwest Harris County. Furthermore, the subsidence map created using GPS results between 2007 and 2011 demonstrate decrease in sinking in the central part of study area. This result also supports the general trend of groundwater level change which has increasing trend after 2000. Therefore, these results indicate groundwater withdrawal is one of the major cause of the subsidence in Northwest Harris.

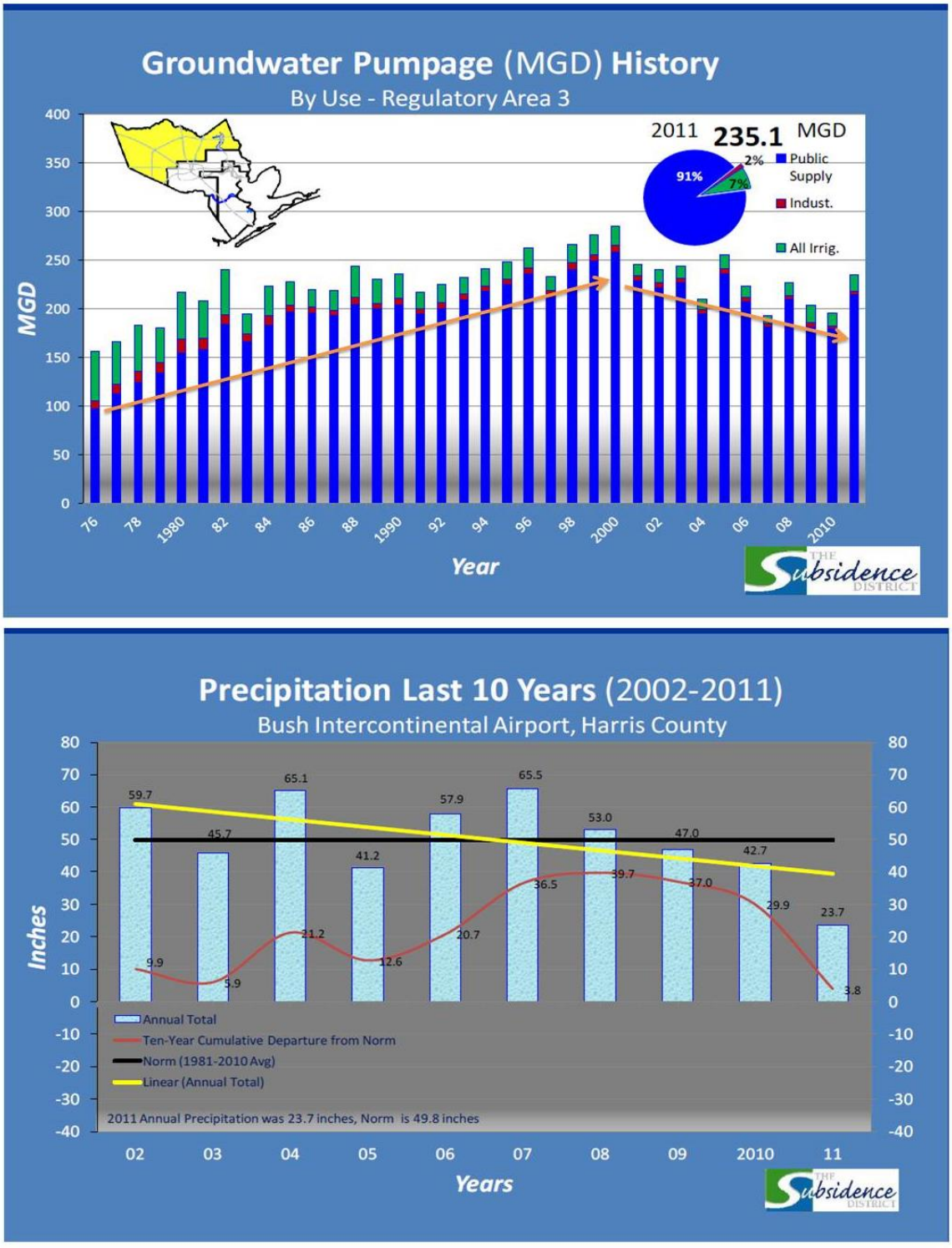

Figure 4.5: Figures for groundwater withdrawal (above) and precipitation (below). The regulatory area is one of the groundwater control area defined by HGCSD (HGCSD, 2012)

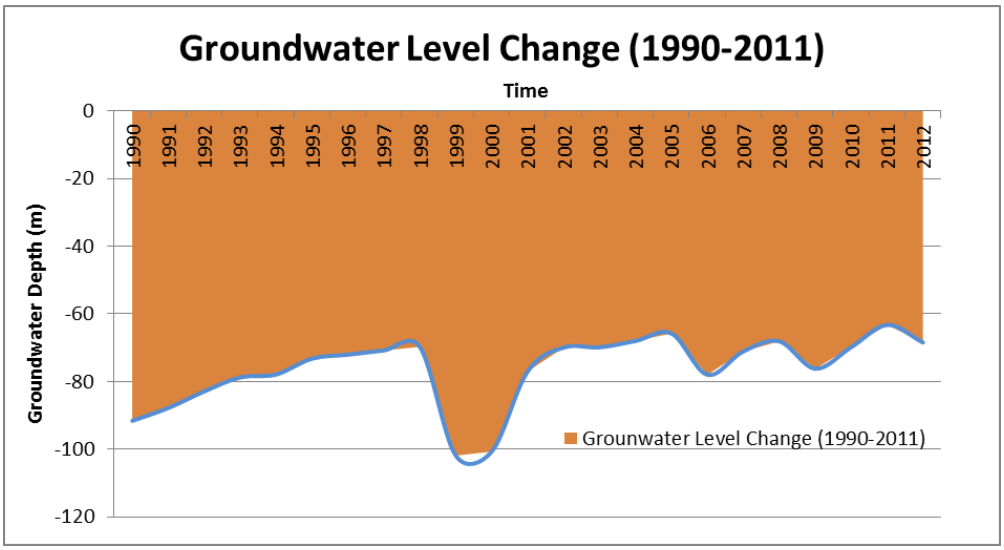

Figure 4.6: Graph of change in groundwater in both Chicot and Evangeline Aquifer. This graph shows annual average of water level change in Chicot and Evangeline Aquifer gathered by 261 wells. Blue line shows the water surface, and orange area is to show the depth surface to groundwater.

4.2.2 Hydrocarbon Extraction

Beside water withdrawal, oil extraction is one of the well-known effects on local subsidence in Houston area. First reported oil withdrawal-based subsidence was on the Goose Creek Oil Field. It was noticed that the subsidence rate exceeded 11 cm after one year production in this area (Pratt & Johnson, 1926). As it was stated in the Chapter 1 and 2, the Northwest area has eight oil fields some of which has productivity since 1930's. The hydrocarbon production data from Railroad Commission of Texas were processed to recognize the volume change in the reservoirs. The result of the oil and gas production data presents the high volumetric change on the Cypress Oil Field, in the central area of Northwest Harris. The production rate in the other oil fields is not as much as the Cypress Oil Field has. When the subsided area is compared with regional production results, it is considered that hydrocarbon production may be the reason for subsidence.

4.2.3 Comparison of Fluid Withdrawals and Remote Sensing Results

Several causes are proposed for subsidence in Houston area. For example, Engelkemeir & Khan (2008) suggested as the role of salt withdrawal, fault activities, etc., differentiated soil compaction, and salt activity (Huang, 2012; Otoum, 2011). The Tomball and Hockley salt domes are the only two domes that has been mapped over northwest of Houston. The salt diapirism of the region was mapped by Huang (2012). According to this study, salt movement in southeast part of Houston area has some role in subsidence at the Northwest Harris. However, most of other studies concentrated on groundwater withdrawal in this area.

The results of groundwater present declination of water level near the center of study area. Besides, the extremely high oil production rate, the factor of compaction in the oil reservoir, is located almost the same region (Figure 4.6). Although the groundwater level is rising in the northwest and southeast portion of the study area, the subsidence is still remaining with lower rates.

The compaction in the aquifer systems was explained by Galloway et al. (1991). However, the reservoir compaction has not been analyzed due to the limitations of understanding characteristic behavior of the productive layers. Doornhof et al. (2006) show the compressibility of the reservoir depending on the rock material and depositional history. Furthermore, Geertsma (1973) concluded the four main conditions that cause subsidence over productive reservoirs:

1. A significant decline in reservoir pressure occurs throughout the production period.

2. Production is effected from a large vertical interval.

3. Oil or gas, or both, are enclosed in loose or weakly cemented rock.

4. The reservoirs with small depth of burial.

As it was explained in Hydrocarbon part in chapter 2, the reservoirs layers are formed by sands, silt and clays which support the third item above. The oil production layers range from approximately ~900 m (3000 ft.) to ~3810 m (12500 ft.) (RRC, 2012). Although the reservoirs are not as shallow as Goose Creek Oil Field, the potential of compaction might be taking place in the productive layers.

When the GPS, LiDAR, and InSAR results is compared to the fluid withdrawal results, it is seen that the trend of both subsidence and fluid level change are located almost at the same part of the Northwest Harris County (Figure 4.6). The surface map of the GPS results for the time span 2008-2011 also supports that the velocity of subsidence in the study area was started to get slower with the groundwater rising after 2000. Therefore, combination of the results of techniques used for study indicates that the fluid withdrawal (both hydrocarbon and water) has significant effect on the subsidence in Northwest Harris County.

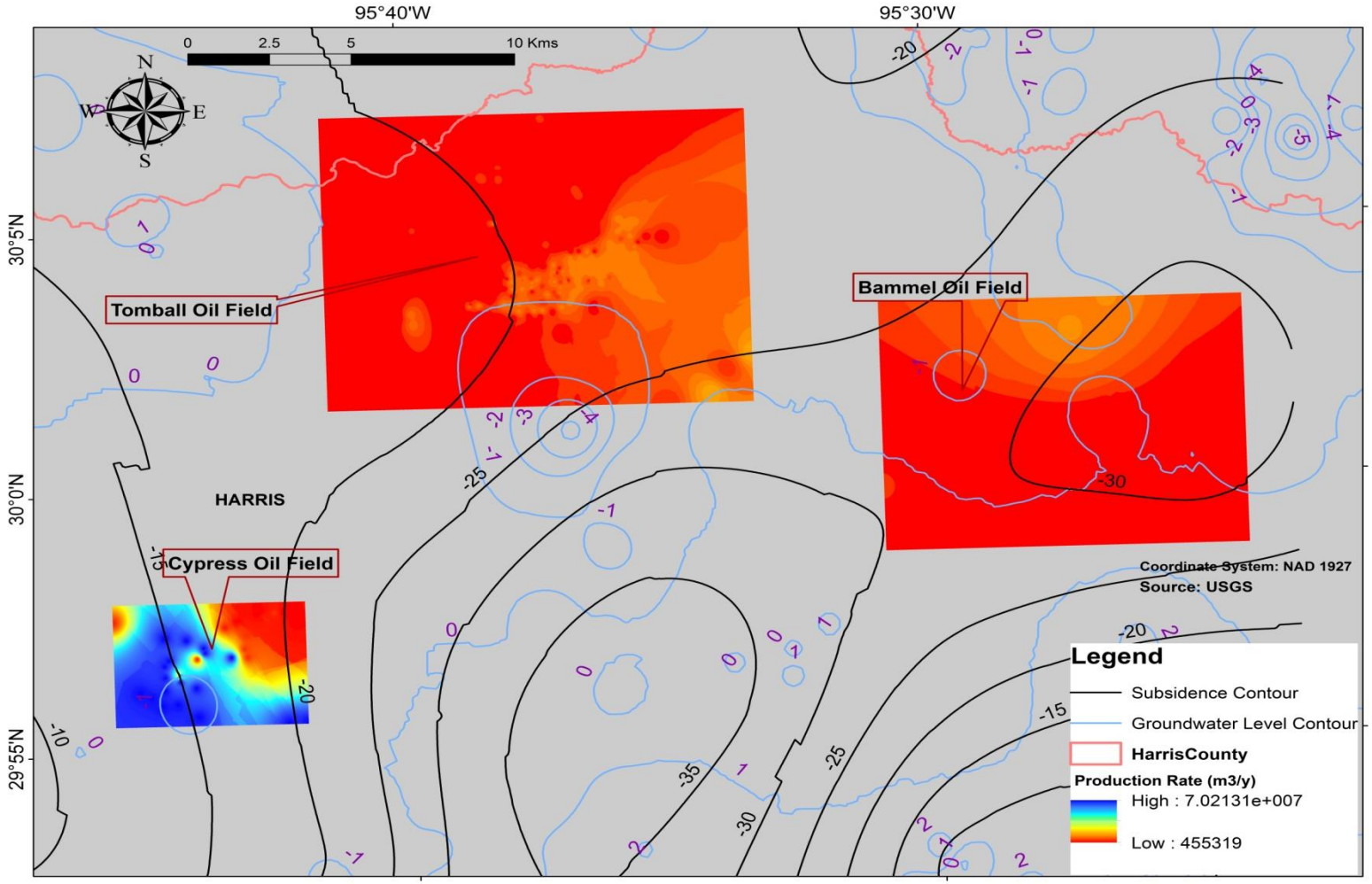

Figure 4.7: The map of comparison among hydrocarbon withdrawal, groundwater pumping and subsidence. The surfaces changing colors red to blue are annual oil production rate data. The blue polylines over the area show the change in groundwater level. Black polylines drived from Kriging interpolated surface of the GPS result demonstrate the subsidence rates over Northwest Harris County

CHAPTER 5: CONCLUSION

The Greater Houston area is the well-known for coping with subsidence problems for many years. Previous studies suggested that the most probable reason for the subsidence is groundwater withdrawal. The Northwest Harris was documented area with the highest rate of land surface lowering.

The GPS, LiDAR, and InSAR remote sensing techniques are the most useful tools to measure subsidence. Surface model generated from the results of 25 GPS locations stated highest subsidence rate near the Jersey Village area. Polygonal height computation from LiDAR DEMs and the Persistent Scatterer InSAR results supports the GPS solutions.

The groundwater level and hydrocarbon extraction data were analyzed to understand their weight on subsidence. Although the excessive water withdrawal seems as a major cause of the subsidence, reservoir compaction due to oil and gas production may be a secondary factor on the sinking of the Northwest Harris. The results of this work showed subsidence ranging from 0.3 to 4.5 cm/y in GPS, LiDAR, and InSAR in the Northwest Harris. The groundwater level is lowering close to the area where subsidence is the highest. Also, the hydrocarbon withdrawals are highest in areas that are sinking more rapidly. The strong correlation between fluid withdrawals and subsidence has been observed. Therefore, both groundwater and hydrocarbon withdrawal in Northwest Harris County are considered to be major drivers on the surface deformation.

REFERENCES

Ashford, J. B., & Hopkins, J. (1995). *Aquifers of Texas.* Austin, Texas: Texas Water Development Board.

Baker, E. T. (1979). *Stratigraphic and Hydrogeologic Framework of Part of the Coastal Plain of Texas.* Texas: Texas Department of Water Resources Report 236.

Bamler, R., & Hartl, P. (1998). Synthetic aperture radar interferometry. *Inverse Problems, 14*, R1-R54.

Bawden, G. W., Johnson, M. R., Kasmarek, M. C., & Middleton, C. S. (2012). *Investigation of Land Subsidence in the Houston-Galveston Region of Texas by Using the Global Positioning System and Interferometric Synthetic Aperture 1993–2000.* U.S.G.S.

Beckelhymer, R. L. (1946). Stratigraphy of Waller and Harris Counties, Texas. *AAPG Bulletin, 30*(1), 52-62.

Bernard, H. A., LeBlanc, R. J., & Major, C. F. (1962). Recent and Pleistocene geology of southeast Texas. in E. H. Rainwater, & R. P. Zingula (Eds.), *Geology of the Gulf Coast and Central Texas* (pp. 175-224). Houston: Houston Geological Society.

Bird, D., Burke, K., Hall, S., & Casey, J. (2005). Gulf of Mexico tectonic history: Hotspot tracks, crustal boundaries, and early salt distribution. *AAPG Bulletin, 89*, 311-328.

Blakey, R. (2006). Sedimentation, tectonics, and paleogeography of North Atlantic region. http://jan.ucc.edu/reb7/nat.html.

Brace, O. L. (1962). Bammel Field. *Typical Oil and Gas Fields of Southeast Texas*, 4-7.

Canada, W. R. (1962). Hockley Field. In *Typical Oil and Gas Fields of Southeast Texas* (pp. 76-79). Houston Geological Society.

Carter, C. (1997). *Principles of GPS, A Brief Primer on the Operation.* Westlake Village, CA: Allen Osborne Associates.

Center, N. O. (2008). *Lidar 101: An Introduction Lidar Technology, Data, and Applications.* Charleston, SC: NOAA Coastal Services Center.

Chan, Y. K., & Koo, V. C. (2008). An introduction to Synthetic Aperture. *Progress In Electromagnetics Research B, 2*, 27-60.

Chowdhury, A. H., & Mace, R. E. (2003). *A Groundwater Availability Model for the Gulf Coast Aquifer in the Lower Rio Grande Valley, Texas—Numerical Simulations through 2050.* Texas: Texas Water Development Board.

Chowdhury, A. H., & Turco, M. J. (2006). *Geology of the Gulf Coast Aquifer Texas.* Retrieved 2012, from http://www.twbd.state.tx.us/publications/reports/GroundWaterReports/GWReports/R365/ch02-Geology.pdf

Cockerhham, K. L. (1957). Developments in Upper Gulf Coast of Texas in 1956. *AAPG Bulletin, 41*(6), 1181-1189.

Cooperating, F. (2003). *LIDAR and Digital Elevation Data.* North Carolina: FEMA's Cooperating.

Coplin, L. S., & Galloway, D. L. (1999). Houston-Galveston, Texas: Managing coastal subsidence. in D. Galloway, D. R. Jones, & S. E. Ingebritsen (Eds.), *Land*

Subsidence in the United States (pp. 35-48). U.S. Geological Survey Circular1182.

Curlander, J. C., & McDonough, R. N. (1991). *Synthetic Aperture Radar: Systems and Signal Processing.* John Wiley and Sons.

Doornhof, D., Kristiansen, T. G., Nagel, N. B., Pattillo, P. D., & Sayers, C. (2006). Compaction and Subsidence. *Oilfield Review, 18*(3), 56-68. Retrieved from https://www.slb.com/~/media/Files/resources/oilfield_review/ors06/aut06/compaction_and_subsidence.pdf

Dutton, S. P., & Loucks, R. G. (2010). Diagenetic controls on evolution of porosity and permeability in lower Tertiary Wilcox sandstones from shallow to ultradeep (200–6700 m)burial, Gulf of Mexico Basin, U.S.A. *Marine and Petroleum Geology, 27*, 69–81.

Ehigiator–Irughe, R., Uzodinma, V. N., & Ehigiator, M. O. (2012). An evaluation of Precise Point Positioning (PPP) in Nigeria using ZVS3003 geodetic control as a case study. *Research Journal in Engineering and Applied Sciences, 1*(2), 134-141.

Engelkemeir , R. E., & Khan, S. D. (2008). LiDAR mapping of faults in Houston, Texas, USA. *Geosphere, 4*(1), 170-182.

Engelkemeir, R. E., Khan, S. D., & Burke, K. (2010). Surface deformation in Houston, Texas using GPS. *Tectonophysics, 490*, 47-54.

European Space Agency (ESA). (2011). *Observing the Earth*. Retrieved 2012, from http://www.esa.int/Our_Activities/Observing_the_Earth/ERS_overview

European Space Agency (ESA). (2012). *What is ERS?* Retrieved December 2012, from ESA Earth Online: https://earth.esa.int/web/guest/missions/esa-operational-eo-missions/ers

Ferretti, A., Prati, C., & Rocca, F. (2001). Permanent Scatterers in SAR Interferometry. *Transactions on Geoscience and Remote Sensing, 39*(1), 8-20.

Fowler, R. (2001). Topographic LIDAR, In Digital Elevation Model Technologies and Applications: The DEM Users Manual. (D. Maune, Ed.) *The American Society for Photogrammetry and Remote Sensing*, 207-236.

Froese, C. R., & Mei, S. (2008). Mapping and monitoring coal mine subsidence using LiDAR and InSAR. *GeoEdmonton,* 1127-1133.

Galloway, D., Jones, D. R., & Ingebritsen, S. E. (1999). *Land Subsidence in the United States* (pp. 117). U.S. Geological Survey Circular 1182.

Galloway, W. (2008). Depositional evolution of the Gulf of Mexico sedimentary basin. (K. J. Hsu, Ed.) *The Sedimentary Basins of the United States and Canada, Sedimentary Basins of the World, v.5*, 505-549.

Galloway, W. E., Ganey-Curry, P. E., Li, X., & Buffler, R. (2000). Cenozoic depositional history of the Gulf of Mexico basin. *AAPG Bulletin, 84*(11), 1743-1774.

Gao, Y., Zhang, Y., & Chen, K. (2006). Development of a real-time single-frequency precise point positioning system and test results. Forth Worth: ION GNSS 19th International Technical Meeting of the Satellite Division.2297-2303

Geertsma, J. (1973). Land subsidence above compacting oil and gas reservoirs. *Journal of Petroleum Technology,* 734-744.

Goldenstein, R. M., Engelhardt, H., Kamb, B., & Frolich, R. M. (1993). Satellite radar interferometry for monitoring ice sheet motion:Application to an Antartic ice stream. *Science, 262*(5139), 1525-1530.

Hackley, P. C. (2012). *Geologic Assessment of Undiscovered Conventional Oil and Gas Resources-Middle Eocene Claiborne Group, United States Part of the Gulf of Mexico Basin.* Virginia: US Geological Survey. Retrieved from http://pubs.usgs.gov/of/2012/1144/

Hackley, P. C., & Ewing, T. E. (2010). Assessment of undiscovered conventional oil and gas resources onshore Claiborne Group, U.S. part of the Gulf of Mexico Basin. *AAPG Bulletin, 94*(10), 1607-1636.

Hamman, H. R. (1987). Cypress Field. *Typical Oil and Gas Fields of Southeast Texas, 2*.

Harris-Galveston Coastal Subsidence District (HGCSD). (2012). *2012 Annual Groundwater Report.* Friendswood: The Subsidence District.

Harvey, C. J., & Burkhead, W. Z. (1939). Fairbanks and Satsuma Fields Harris County, Texas. *AAPG Bulletin, 23*(5), 686-698.

Holzer, T. L., & Bluntzer, R. L. (1984). Land Subsidence Near Oil and Gas Fields, Houston, Texas. *Groundwater, 22*(4), 450-459.

Hooper, A., Zebker, H., Segall, P., & Kampes, B. (2004). A new method for measuring deformation on volcanoes and other natural terrains using InSAR persistent scatterers. *Geophysical Research Letters, 31*, L23611.

Hosman, R. L. (1996). *Regional Stratigraphy and Subsurface Geology of Cenozoic Deposits, Gulf Coastal Plain, South-Central United States—Regional Aquifer System Analysis—Gulf Coastal Plain* (pp. 35). U.S. Geological Survey.

Huang, Z. (2012). *Multidisciplinary Investigation of Surface Deformation above Salt Domes in Houston, Texas* (pp. 21). Houston, Texas: Master Thesis: University of Houston.

Johnson, A. I. (1991). *Land Subsidence.* UK: IAHS Press.

Jorgensen, D. G. (1975). *Analog-model Studies of Ground-water Hydrology in the Houston District, Texas.* Houston, Texas: U. S. Geological Society.

Kasmarek, M., Johnson, M., & and Ramage, J. R. (2010). *Water-level altitudes 2010 and water-level changes in the Chicot, Evangeline, and Jasper aquifers and compaction 1973–2009 in the Chicot and Evangeline Aquifers,Houston-Galveston region* (pp. 17). U.S. Geological Survey.

Kim, E. M., & Ruppel, S. C. (2005). *Oil and Gas Production in Texas* (pp. 2). Austin, Texas: The University of Texas at Austin, Bureau of Economic Geology.

Knox, P. R., Kelley, V. A., & Deeds, A. V. (2007). *Structure of the Yegua-Jackson Aquifer of the Texas Gulf Coastal Plain.* Austin, Texas: Texas Water Development Board.

Kreitler, C. W. (1977). Fault control of subsidence, Houston, Texas. *Groundwater, 15*(3), 203-214.

Kuehn, F., Hoffmann-Rothe, A., Albiol, D., Cooksley, G., J., D., Granda, J., . . . Murdohardono, D. (2009). Detection of land subsidence in Semarang, Indonesia

using persistent scatterer interferometry. Proceedings of Asian Association on Remote Sensing. TS30-3

LaBarbera, R. (2012). *Harris-Galveston Area Council*. (Harris-Galveston Area Council) Retrieved November 24, 2012, from http://www.h-gac.com/rds/gis_data/lidar/default.aspx

Lauknes, T. R., Dehls, J., Larsen, Y., & Hgda, K. A. (2005). A comparison of SBAS and PS ERS InSAR for subsidence monitoring in Oslo, Norway. *Proc. Fringe 2005 Workshop.* Frascati, Rome: ESA ESRIN.

Lefebvre, L. (2010). *Gulf Coast Aquifer, Texas*. Retrieved October 2012, from http://academic.emporia.edu/schulmem/hydro/TERM%20PROJECTS/2010/Lefebvre/Lynn.htm

Louisiana Department of Environmental Quality(LDEQ). (2002). *Chicot Aquifer Summary Baseline Monitoring Project.* Louisiana Department of Environmental Quality.

Martin, A., Olson, D., & Mills, C. (2012). *Peakbagger*. Retrieved March 20, 2013, from http://www.peakbagger.com/list.aspx?lid=13514

Martyn, P. F., & Beery, R. F. (1961). The Milton Field, Harris County, Texas, produced before discovery. *Houston Geological Society Bulletin, 3*(10), 19-20.

Martyn, P. F., & Berry, R. F. (1962). Milton Field. In *Typical Oil and Gas Fields of Southeast Texas.* Houston Geological Society.

Massonnet, D., & Feigl, K. L. (1998). Radar interferometry and its application to changes in the Earth's surface. *Reviews of Geophysics, 36*(4), 441-500.

Meyer, W. B. (2002). Allison's aftermath. *Point of Beginning* , 4 p.

Michel, T. A. (2006). *100 years of Groundwater Use and Subsidence in the Upper Texas Gulf Coast.* Aquifers of the Gulf Coast of Texas. Texas Water Development Report 365.139-148

Morton, R. A., Buster, N. A., & Krohn, M. D. (2002). Subsurface controls on historical subsidence rates and associates wetland loss in southcentral Lousiana. *Transactions Gulf Coast Association of Geological Societies, 52,* 767-778.

Mouratidis, A., Briole, P., Astaras, A., Pavlidis, S., Tsakiri, M., Ilieva, M., . . . Katsambalos, K. (2010). Contribution of InSAR and Kinematic GPS Data to Subsidence and Geohazard Monitoring in Central Macedonia. *Aristotle University of Thessaloniki.* Thessaloniki, Greece: Scientific Annals, School of Geology.

National Geodetic Survey (NGS). (2012b). *Accuracy.* Retrieved December 2012, from http://geodesy.noaa.gov/OPUS/about.jsp#accuracy

National Oceanic and Atmospheric Administration (NOAA) Coastal (Service) Center. (2008). *Lidar101 : An Introduction LiDAR Technology, Data, and Applications.* Charleston, SC: NOAA Coastal Service Center.

National Research Council. (1991). *Mitigating Losses from Land Subsidence in the United States.* Washington: National Academy Press.

Neighbors, R. J. (2003). Subsidence in the greater Houston area: past, present and future. *Harris-Galveston coastal Subsidence District, Fort bend Subsidence District.* CIGMAT.

Norman, C. (2005). Ground subsidence and active faults in the Houston metropolitan. *Coastal Subsidence, Sea Level and the Future of the Gulf Coast HGS/ECH* (p. 31). Field Trip Guide.

Olien, R. M. (2012). *Oil and Gas Industry.* Retrieved December 25, 2012, from Handbook of Texas Online: http://www.tshaonline.org/handbook/online/articles/doogz

OnboardInformatics. (2012). *Citi-Data.com*. Retrieved September 13, 2013, from www.city-data.com/city/Northwest-Harris-Texas.html

Osmanoglu, B., Dixona, T. H., Wdowinskia, S., Cabral-Canob, E., & Jiang, Y. (2011). Mexico City subsidence observed with persistent scatterer InSAR. *International Journal of Applied Earth Observation and Geoinformation, 13*(1), 1-12.

Otoum, M. A. (2011). An Integrated Geophysical Investigation to Map the Hockley Active Fault in Northwest Harris County, Texas. *Houston, Texas: Master Thesis, University of Houston*.

Pratt, W., & Johnson, D. (1926). Local subsidence of the Goose Creek oil field. *Journal of Geology, 34*(7), 577-590.

Railroad Commission of Texas (RRC). (2012). *Production Reports*. Retrieved from RRC Online System: http://webapps.rrc.state.tx.us/PR/publicQueriesMainAction.do

Raucoules, D., Colesanti, C., & Carnec, C. (2007). Use of SAR interferometry for detecting and assessing. *C. R. Geoscience, 339*, 289-302.

Reigber, A., Erten, E., Guillaso, S., & Hellwich, O. (2007). I.D.I.O.T.: A free and easy-to-use software tool for DInSAR analysis. *Envisat Symposium 2007.* Montreux, Switzerland: ESA.

Roger, M. (2009). Oil and Gas Industry. In *The Handbook of Texas Online.* Texas State Historical Association.

Salvador, A. (1991). Origin and development of the Gulf of Mexico basin. In *The Gulf of Mexico Basin: the Geology of North America* (pp. 389-444). Boulder, Colorado: Geological Society of America.

Saribudak, M. (2010). Geophysical mapping of Hockley fault in NW Houston: a few suprising results. *Houston Geological Society Bulletin, 52*(9), 43-57.

Sellards, E. H., Adkins, W. S., & Plummer, F. B. (1932). *The Geology of Texas, Volume I, Stratigraphy*. Austin,Texas: The University of Texas at Austin, Bureau of Economic Geology.

Sithole, G., & Vosselman, G. (2004). Experimental comparison of filter algorithms for bare-Earth. *Journal of Photogrammetry & Remote Sensing, 59,* 85-101.

Sneed, M., & Brandt, J. T. (2007). Detection and Measurement of Land Subsidence Using Global Positioning System Surveying and Interferometric Synthetic Aperture Radar, Coachella Valley, California. *U.S. Geological Survey*, 12 p.

Stern, R. J., & Dickinson, W. R. (2010). The Gulf of Mexico is a Jurassic backarc basin. *Geosphere, 6*(6), 739-754.

Tarikhi, P. (2010). InSAR: a new generation. *Position Magazine*(50), 42.

Turcan, A. N., B., W. J., & C., K. (1966). *Interstate Correlation of Aquifers, Southwestern Louisiana and Southeastern Texas* (pp. 231-236). U.S. Geological Survey.

U.S.Census. (2010). *Place of USA*. Retrieved September 12, 2013, from http://www.placesofusa.com/texas/harris-county/northwest-harris-ccd

Verbeek, E. R., & Clanton, U. S. (1981). Historically active faults in the Houston metropolitan area, Texas. *Houston Area Environmental Geology-Surface Faulting, Ground Subsidence, Hazard Liability*. *Houston Geological Society Special Publications,* 28-68.

Wang, G., & Soler, T. (2012). OPUS for horizontal subcentimeter-accuracy landslide monitoring: A case study in the Puerto Rico and Virgin Islands region. *Journal of Surveying Engineering, 138*(3), 143-153.

Ward, B. (2006). *Geologic History as it Relates to Modern Vegetation Patterns of South Central Texas.* Texas: Native Plant Society of Texas Symposium.

Worldmark Encyclopedia of the States. (2004). *Texas: State of Texas.* Detroit: Gale.

Zilkoski, D., Hall, L. W., Mitchell, G. J., Kammula, V., Singh, A., Chrismer, W. M., & Neighbors, R. J. (2003). The Harris-Galveston Coastal Subsidence District/National Geodetic Survey Automated GPS Subsidence Monitoring Project. *the U.S. Geological Survey Subsidence Interest Group Conference*, (pp. OFR 03-308).